

Bose–Einstein Correlations  
in  
Deep Inelastic Scattering at HERA

Inaugural Dissertation

zur Erlangung der Philosophischen Doktorwürde  
vorgelegt der  
Philosophischen Fakultät II  
der  
Universität Zürich

von  
Christian Dollfus  
von Basel und Zürich

begutachtet von Prof. Dr. P. Truöl

Zürich 1996

Bose–Einstein Correlations  
in  
Deep Inelastic Scattering at HERA

Inaugural Dissertation

zur Erlangung der Philosophischen Doktorwürde  
vorgelegt der  
Philosophischen Fakultät II  
der  
Universität Zürich

von  
Christian Dolfus  
von Basel und Zürich

begutachtet von Prof. Dr. P. Truöl

Zürich 1996

Die vorliegende Arbeit wurde von der Philosophischen Fakultät II der Universität Zürich im Sommersemester 1996 auf Antrag von Prof. Dr. Peter Truöl und Prof. Dr. Roland Engfer als Inaugural-Dissertation angenommen.

Meinen Eltern gewidmet



# Contents

Abstract . . . . .	iii
Zusammenfassung . . . . .	iii
<b>1 Introduction</b>	<b>1</b>
<b>2 Theory of Bose Einstein correlations</b>	<b>4</b>
2.1 Idea . . . . .	4
2.2 History . . . . .	5
2.3 Derivation of the correlation function . . . . .	6
2.3.1 Coherence and chaos . . . . .	8
2.3.2 The Goldhaber parametrization . . . . .	9
2.4 String model approach to Bose-Einstein correlations . . . . .	10
2.4.1 The Lund string model . . . . .	10
2.4.2 String model of the Bose-Einstein correlations . . . . .	12
<b>3 Deep inelastic electron scattering</b>	<b>15</b>
3.1 Deep inelastic scattering . . . . .	15
3.2 Diffractive scattering . . . . .	17
<b>4 The H1 detector</b>	<b>19</b>
4.1 The electron proton storage ring HERA . . . . .	19
4.1.1 The H1 Detector . . . . .	21
4.1.2 The H1 Tracking System . . . . .	23
<b>5 The inner z-drift chamber</b>	<b>27</b>
5.1 The hardware . . . . .	27
5.1.1 Current monitoring . . . . .	30
5.1.2 Gas mixtures . . . . .	31
5.1.3 Experience with another sense wire type . . . . .	32
5.1.4 High voltage problems . . . . .	33
5.2 The software . . . . .	33
5.2.1 Qt analysis and noise studies . . . . .	33
5.2.2 Isochrone map . . . . .	34
5.2.3 Reconstruction of tracks . . . . .	34

---

5.3	Calibration . . . . .	36
5.3.1	$\phi$ calibration . . . . .	36
5.3.2	Calibration of drift velocity and time offset . . . . .	37
5.4	Resolution, efficiency and performance . . . . .	44
<b>6</b>	<b>Bose Einstein correlation analysis</b> . . . . .	<b>54</b>
6.1	Event selection . . . . .	54
6.1.1	Deep inelastic scattering events . . . . .	54
6.2	Track selection . . . . .	55
6.3	Technical aspects of the analysis . . . . .	57
6.4	Correlations in invariant mass . . . . .	65
6.5	Comparison with Monte Carlo . . . . .	69
6.5.1	Track finding efficiency and correction factors . . . . .	69
6.5.2	Comparison of different Monte Carlo generators . . . . .	75
6.5.3	Monte Carlo with BEC included . . . . .	76
6.6	Final state interactions and corrections . . . . .	77
6.6.1	Coulomb correction . . . . .	77
6.7	Purity and its correction . . . . .	82
6.7.1	Resonances and decay channels . . . . .	82
6.7.2	Purity correction . . . . .	82
6.8	Dependence of BEC on kinematic variables . . . . .	86
6.9	Systematic errors . . . . .	89
6.10	Results and discussion . . . . .	90
6.10.1	Low $Q^2$ data . . . . .	91
6.10.2	High $Q^2$ and diffractive data . . . . .	93
6.10.3	$x_{Bjorken}$ , $W$ and multiplicity dependence . . . . .	102
6.11	Comparison with other Experiments . . . . .	102
	Appendix A . . . . .	103
	Acknowledgments . . . . .	110
	Curriculum Vitae . . . . .	111

## Abstract

Two-particle correlations in invariant mass are studied separately for like-sign and unlike-sign charged particles. The like-sign correlations exhibit the familiar enhancement at low invariant masses possibly related to the dimensions of the hadronic source. The data are compared to and corrected with different QCD models where the hadronization is performed with the string-fragmentation model. The observed correlations can be described with parametrizations quite similar to those obtained in previous analyses of  $\mu p$ -inelastic scattering and  $e^+e^-$ -annihilation. The data were taken with the H1 detector at HERA  $ep$ -collider in 1994, in which 26.7 GeV positrons collided head-on with 820 GeV protons at  $\sqrt{s} = 296$  GeV. The detector components used for this analysis are presented. Monitoring the the performance, the calibration and measuring the efficiency of the innermost driftchamber constitutes a major part of this work. Those chamber measures the tracks along the coordinate parallel to the beam line.

## Zusammenfassung

Zwei-Teilchen Korrelationen in der invarianten Massenverteilung werden sowohl für gleichgeladene als auch für ungleich geladene Teilchen analysiert. Gegenüber ungleichen Paaren zeigen die gleichgeladenen Teilchen die bekannte Häufung von Ereignissen gegen kleine invariante Massen hin. Die Form dieser Erhöhung kann mit der raum-zeitlichen Ausdehnung der Quelle in Verbindung gebracht werden, aus der die Teilchen stammen.

Die Daten werden mit verschiedenen QCD Modellen verglichen und korrigiert, welche für die Hadronisation das String-Modell benutzen. Die beobachteten Korrelationen können mit denselben parametrisierten Funktionen verglichen werden wie sie auch von anderen Experimenten verwendet wurden wie z. B. in tief inelastischen  $\mu p$ -Kollisionen oder in der  $e^+e^-$ -Annihilation.

Die Daten wurden mit dem H1 Detektor am HERA Speicherring im Jahre 1994 aufgenommen, in dem Positronen von 26.7 GeV Energie mit Protonen von 820 GeV frontal zusammenstossen, was einer Schwerpunktsenergie ( $\sqrt{s}$ ) von 296 GeV entspricht.

Im experimentellen Teil werden Detektorkomponenten, die für diese Analyse verwendet wurden, speziell besprochen. Die Bestimmung der Effizienz, die Kalibrierung und die Auflösung der innersten Driftkammer, welche die  $z$ -Koordinate (parallel zur Strahlachse) vermisst, bilden einen wesentlichen Teil der hier vorgelegten Arbeit.

# Chapter 1

## Introduction

The primary goal of high energy physics today is a theory to describe the basic components of nature and the forces acting on them. Dramatic progress has been made in particle physics during the past three decades. A series of important experimental discoveries has firmly established the so called *standard model* in particle physics together with the principle of *gauge theories* which represent a comprehensive theory of particles and their interactions. It gives a complete and correct description of all non-gravitational physics and unifies very different forces as the electromagnetic and the strong one with the same principle. The proton and the neutron, which form nuclei, are no longer regarded as elementary particles because in 1968 electron scattering experiments gave the first clear hints that point-like particles are existing inside the proton. These were named “partons”. Earlier, in 1964, Gell-Mann and Zweig had proposed that the proton and most other of the discovered particles at that time were in fact built from more basic entities named “quarks”. With this quark model sense could be made out of the multitude of meson and baryon resonances then being found. When interpreted as excited states of multi-quark and quark-antiquark systems, these resonances and their properties were understood. At the same time one realized that the dynamics of quarks and leptons can be described by an extension of the sort of quantum field theory that proved successful in describing the electromagnetic interactions of charged particles. The fundamental interactions are widely believed to be described by quantum field theories possessing local gauge symmetry. In the standard model of elementary particle physics the fundamental particles of the universe are divided into two groups: particles of spin half (fermions) which make up the whole matter (quark and leptons) and particles of integer spin which mediate the forces between the matter particles. The standard model classifies the forces carried by particles of integer spin into four categories:

The gravitational force is the weakest of the four forces. A particle of spin 2 called *graviton* is thought to be the carrier of this interaction.

The electromagnetic force affects only electrically charged particles and is caused by the exchange of the massless *photon*. The corresponding gauge symmetry group of this force is the Lie group  $U(1)$ .

The weak force acts on all particles of spin  $\frac{1}{2}$ . The carriers are known as massive vector bosons

$W^+$ ,  $W^-$  and  $Z^0$ . Their gauge group is  $SU(2)$ .

Finally the strong force, constitutes the fourth category. The *gluon* interacts with quarks and other gluons as the intermediate particle. Quarks and gluons are carriers of *color*, a new quantum state in the same way that electrons are carriers of electric charge. This is the origin of the name Quantum Chromodynamics (QCD). The strong force has the surprising property, called *confinement*, that always binds particles together into combinations that are colorless (white). This particular feature is responsible for the formation of hadrons in the final state in high energy reactions.

The basic method of studying the structure of particles and their interactions is to carry out scattering experiments. In deep inelastic scattering (DIS) the electron scatters the proton. To be able to resolve any structure within the diameter of the proton of  $10^{-15}$  m the probing particle (electron) needs a momentum greater than 1 GeV according to the De Broglie wave length  $p = \hbar \cdot k$ . The greater the momentum of the probe used the shorter is the wavelength and hence the smaller are the distances which can be resolved.

At the end of 1991 the first electron proton collider HERA at the DESY Laboratory in Hamburg came into operation, providing collisions of 26.7 GeV electrons and 820 GeV protons resulting in a center of mass energy near 300 GeV. This is more than a factor of ten above the energies reached so far in lepton-nucleon scattering experiments. HERA as a colliding experiment allows the investigation of deep inelastic scattering down to values of  $x_{Bjorken} = 10^{-4}$ , two orders of magnitude lower in  $x$  than present fixed target experiments. Studies on leptoquark production, proton structure functions, hadronic final states and a lot more are possible in a new kinematical region. Two general purpose detectors H1 and ZEUS are installed in the HERA beam lines in the interaction regions.

The perturbative calculation of physical reactions is limited to phenomena at the parton level where single gluons and quarks are produced. However, the phenomena occurring afterwards, i. e. the transformation of the outgoing colored partons into a set of color singlet hadrons, is up to now not calculable. In order to keep track of the process occurring during the hadronization, probabilistic models are used. They fill the gap left by the limited theoretical approaches between partons and the hadronic final states which are detected and measured in a detector. These phenomenological models of fragmentation make possible a proper comparison between experiment and results obtained by perturbative QCD. The models used in this thesis, unfortunately, do not explicitly include interference terms. Important quantum mechanical effects are therefore ignored.

This thesis deals with a quantum mechanical interference of hadrons in the fragmentation stage. The interference is a manifestation of the quantum statistics of hadrons which produces a correlation among identical particles. For identical bosons the effect is known as Bose-Einstein correlation as bosons obey the Bose-Einstein statistic. The principle is used in radio astronomy as well as in optics to determine the spatial extent of photon radiating sources. The interference occurs in particle physics at the beginning of the hadronization and therefore Bose-Einstein correlations reflect, to a great extent, some aspects of the particle production mechanism. Here the Bose-Einstein effect is used to obtain information concerning the space-time characteristics of the interaction region and to highlight the role of quantum interferences in the multiparticle

production process.

Chapter 2 gives a theoretical overview of Bose-Einstein correlations and their interpretation.

Chapter 3 explains the kinematics of deep inelastic scattering processes at HERA.

Chapter 4 shortly describes the HERA accelerator and the H1 detector, in particular the driftchambers of the tracker part of the H1 detector which are mainly used to analyze the data.

Chapter 5 describes the inner  $z$ -drift chamber of the H1 experiment. The performance, the calibration and the efficiency in the 1993 – 1995 running periods are discussed in detail.

Chapter 6 discusses the analysis of Bose-Einstein correlations with data collected during 1994.

## Chapter 2

# Theory of Bose Einstein correlations

### 2.1 Idea

In classical physics it is possible to keep track of individual particles even when they may look alike. In quantum mechanics, however, identical particles are truly indistinguishable because we cannot specify more than a complete set of commuting observables for each of the particles, in particular we cannot follow the trajectory of a particle because that would entail a position measurement at each instant of time, which necessarily disturbs the system due to the Heisenberg uncertainty principle. In particular the two situations (1) and (2) shown in fig. 2.1 cannot be distinguished—not even in principle.

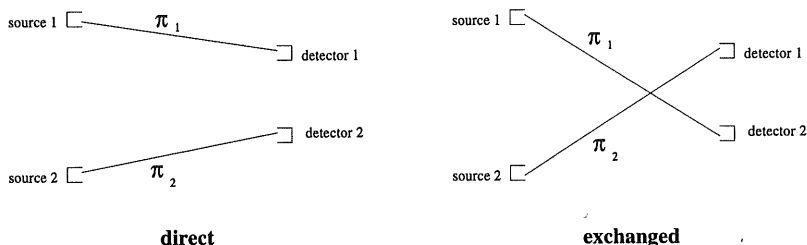


Figure 2.1: Two different paths of a two-pion system, for example, in which we cannot assert even in principle through which of the paths the pions pass.

One of the most fundamental aspect of quantum theory is that particles are mathematically well described in terms of wave functions and that production or particle propagation is determined by the absolute square of the sum of the amplitude of the wave functions for that process.

Let  $\Psi_n(\dots q_i, \dots q_j, \dots)$  be a wave function of a  $N$ -body system of identical particles where the  $q_i$  denotes the collection of all the coordinates of the  $i$ -th particle, including the position coordinates

and all other internal coordinates like spin for example. Let  $\mathcal{P}_{ij}$  be a permutation operator which interchanges the positions of  $q_i$  and  $q_j$  when applied to the wave function  $\Psi_n$ . Since  $\mathcal{P}_{ij}^2 \Psi_n = \Psi_n$  the eigenvalues of  $\Psi_n$  are +1 and -1. So  $\Psi_n$  is either symmetric or antisymmetric under the interchange of two coordinates:  $\mathcal{P}_{ij} \Psi_n = \pm \Psi_n$

It turns out that such systems of  $N$  identical particles are either totally symmetrical under the interchange of any pair, in which case the particles are said to satisfy **Bose–Einstein** (BE) statistics, hence known as **bosons**, or totally antisymmetrical, in which case the particles are said to satisfy **Fermi–Dirac** (FD) statistics, hence known as **fermions**. Thus

$$\mathcal{P}_{ij} \Psi_n(N \text{ identical bosons}) = + \Psi_n(N \text{ identical bosons}) \quad (2.1)$$

$$\mathcal{P}_{ij} \Psi_n(N \text{ identical fermions}) = - \Psi_n(N \text{ identical fermions}) \quad (2.2)$$

where  $i$  and  $j$  are arbitrary.

It is an empirical fact that a mixed symmetry does not occur. In relativistic quantum theory it can be proved (spin–statistic theorem from W. Pauli 1940) that half–integer spin particles cannot be bosons and integer spin particles cannot be fermions.

Let  $\langle 1|\pi_1 \rangle$  be the amplitude for  $\pi_1$  to be detected in detector 1 and  $\langle 2|\pi_2 \rangle$  the same for  $\pi_2$  and detector 2. Since we have undistinguishable bosons the total amplitude to obtain a particle in each of the two counters is the sum

$$\langle 1|\pi_1 \rangle \cdot \langle 2|\pi_2 \rangle + \langle 1|\pi_2 \rangle \cdot \langle 2|\pi_1 \rangle \quad (2.3)$$

and the probability is the square of that amplitude containing an interference term.

To see the fundamental difference between bosons and fermions we replace the two detectors by one (say detector 1) and calculate the probability for two particles to be detected in one single detector. If two particles  $a$  and  $b$  are not identical, the probability is  $2 \cdot |\langle 1|a \rangle|^2 \cdot |\langle 1|b \rangle|^2$ . This probability changes to  $4 \cdot |\langle 1|a \rangle|^2 \cdot |\langle 1|b \rangle|^2$  if we deal with undistinguishable bosons. For fermions the probability vanishes according to the Pauli exclusion principle.

The result is an enhanced probability for identical bosons to be emitted with small relative four–momenta as compared with non–identical bosons under otherwise similar conditions.

The experimental observation of this phenomenon is normally carried out by means of a correlation function. This function is defined as the probability to observe two identical bosons divided by the probability to observe distinguishable ones and is a function of the spatial distance of two detectors. From the characteristics of this arisen interference pattern it is possible, at least principally, to determine the space–time dimensions of the boson source.

## 2.2 History

In 1954 R. Hanbury–Brown and R. Q. Twiss developed a new type of interferometer for measuring the diameter of discrete radio sources and developed the mathematical theory [17]. The principle of the method is based upon the correlation between the rectified outputs of two independent receivers at each end of a baseline. The relative phases of the two radio signals are lost and only the correlation in their intensity fluctuations is measured. This new system was



developed for use with very long baselines and hence the resolution of the "Michelson interferometer" could be improved crucially. These advantages lead the authors to suggest that the principle might be applied to the measurement of the angular diameter of visual stars. Thus they replaced the two aerials by two mirrors and the radio frequency detectors by photomultipliers and measure, as a function of the separation of the mirrors, the correlation between the fluctuations in the currents from the photoelectric cells when illuminated by a star [18]. In 1956 a laboratory experiment was carried out to test experimentally the principle of these intensity interferometer [18]. To get more precise data the experiment was rebuilt and described in detail in [20]. At the end of 1956 the first measurement of the diameter of Sirius was made, since this was the only star bright enough to give a workable signal-to-noise ratio with their preliminary equipment at Jodrell Bank (England) [19]. These intensity correlations are also called "second order coherence" or "Bose-Einstein correlations" (BEC) or "Hanbury-Brown and Twiss effect" (HBT effect).

Intensity interferometry with photons is still an important tool for astronomers and is used also in biology to measure the spatial extent of biological objects.

In 1959 G. Goldhaber, S. Goldhaber, W. Lee and A. Pais were working on a proton anti-proton collision experiment in Berkeley. They were searching for the  $\rho$  meson which had been theoretically predicted to be a pion-pion resonance state. They searched for a  $\rho$  signal by comparing the invariant mass of like charged pion pairs with that of unlike charged pairs. Due to the poor statistics of their experiment, the observation of a  $\rho$  signal was not possible. They compared therefore the cosine of the opening angle between pions and observed a difference in the angular distribution for like and unlike charged pion pairs [21]. Some time later they could explain this difference as a result of a quantum interference of identical bosons i. e. Bose-Einstein correlations [22] (in the future also named as GGLP-effect according to the authors of article [22]).

Applying this technique to particle physics the size and shape of the volume in space-time from which particles are produced could be measured. In the 35 years since then in nearly all types of high energy scattering experiments possible in physics such as  $pp$ ,  $\bar{p}p$ ,  $\pi p$ ,  $Kp$ ,  $\mu p$ ,  $\nu$ -*deuterium*,  $e^+e^-$  annihilations,  $\gamma\gamma$  reactions, and heavy-ion collisions BE correlations were studied.

Comprehensive reviews of results of BEC analyses can be found in [27]-[31].

A possibly different interpretation is offered by the color-string model. As emphasized by Andersson and Hofmann [35] and Bowler [36] the string hadronization model contains most of the ingredients for the Bose-Einstein correlations (BEC). Recently, BEC have been found to be the likely origin of the so-called "intermittency" effect [24], with its characteristic power-law behavior. In [25] B. J. Bjorken pointed to the importance of BEC in the understanding of the geometry of multi-hadron production.

### 2.3 Derivation of the correlation function

The analogy between the Bose-Einstein effect in particle physics and the "second order interference" of photons in optics was realized and the correlation function concept was introduced as a tool in describing the Bose-Einstein effect. A correlation function for BEC in particle physics can be expressed as the ratio of the two particle inclusive cross section to the product of the

single-particle cross sections

$$R_{BE} = \frac{P(1,2)}{P(1)P(2)} \quad (2.4)$$

The intensity of light is classically determined by the absolute square of the sum of electromagnetic fields. In quantum mechanics the probability for particle production is determined by the absolute square of the amplitudes for the process. This means that cross terms in the square of the sum of different contributions to a process give rise to interference in the same way as interference in light occurs.

This heuristic procedure neglects important effects of multiparticle dynamics but helps to understand the origin of Bose-Einstein correlations. We start from the situation shown in Figure 2.2 where two pions created in the same event in the space-time points  $S_1$  and  $S_2$  within the pion source described by  $\rho(r)$  and propagate with the four momenta  $p_1$  and  $p_1$  towards the two detectors  $D_A$  and  $D_B$ .

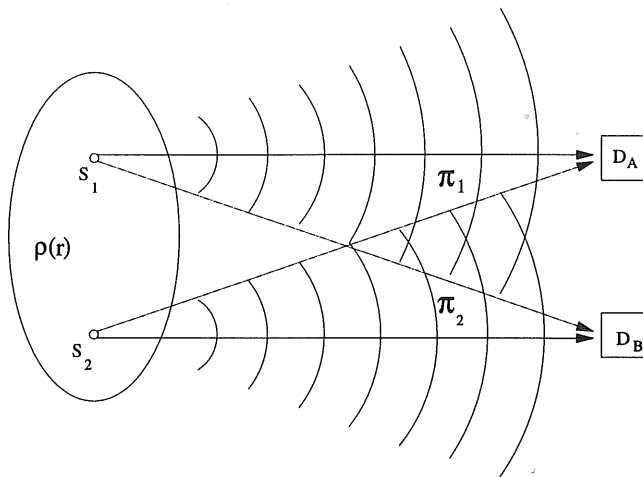


Figure 2.2: Schematic illustration of a two-pion correlation experiment. The space-time points  $S_1$  and  $S_2$  within the pion source described by  $\rho(r)$  emit the particles which are detected in  $D_A$  and  $D_B$ .

Because of the identity of the pions the wave function has to be properly symmetrized as follows (here the Bose-Einstein statistic comes in):

$$\Psi(1,2) = \frac{\Psi_{1A}\Psi_{2B} + \Psi_{1B}\Psi_{2A}}{\sqrt{2}} \quad (2.5)$$

where  $\Psi_{1A} \propto e^{ip_1(D_A - S_1)}$  which correspond to the wave function for a boson produced at  $S_1$  and traveling to detector  $D_A$  under the assumption that the boson wave functions are described by plane waves. The alternative paths for the observed event (Figure 2.2) must be added coherently according to equation 2.5. The probability for that special process is then

$$dP_{12} \propto dS_1 dS_2 \frac{1}{\sqrt{2}} \left| e^{i((p_1(D_A - S_1) + p_2(D_B - S_2)))} + e^{i((p_1(D_A - S_2) + p_2(D_B - S_1)))} \right|^2 \quad (2.6)$$

$$\propto [1 + \cos((p_1 - p_2)(S_1 - S_2))] dr_1 dr_2$$

If the pions are emitted from the whole source statistically independent (chaotic source) and if the density of the source is described by a distribution function  $\rho(r)$ , one obtains the net probability by integrating over  $S_1$  and  $S_2$  with the result:

$$P_{12} \propto \int dP_{12} \rho(S_1) \rho(S_2) = 1 + |\tilde{\rho}(T)|^2 \quad (2.7)$$

where  $T = p_1 - p_2$  and  $\tilde{\rho}(T)$  is the Fourier transform of  $\rho(r)$  with respect to  $q$  and tends to unity as  $q \rightarrow 0$ . This result represents the correlation function of BEC and hence the basis of the traditional pion interferometry. Insertion of a model density of the source reveals that the variation of the probability  $P_{12}$  with  $q$  determines suitable parameters describing the linear dimensions of the source i.e. the probability of detecting two identical pions depends on the shape of the interaction volume  $\rho(r)$  and this dependence is given by its Fourier transform.

### 2.3.1 Coherence and chaos

Following [10] one can consider the possibility of a time dependent amplitude  $f(t)$  which is similar to a certain "phase" associated with each local source. Assume the case of two pion radiating point-like oscillators. Then the total amplitude for emitting a pion with momentum  $p_1$  (single particle production) is given by:

$$\Psi(1) \propto f_A e^{ip_1(r - r_A)} + f_B e^{ip_1(r - r_B)} \quad (2.8)$$

where  $f_A = f_A(t)$  and  $f_B = f_B(t)$  are the phase factors and  $r$  the position of the detector. The joint amplitude of observing two particles with momenta  $p_1$  and  $p_2$  is

$$\Psi(1, 2) = \Psi(1)\Psi(2) \propto [f_A e^{ip_1(r - r_A)} + f_B e^{ip_1(r - r_B)}][f_A e^{ip_2(r - r_A)} + f_B e^{ip_2(r - r_B)}] \quad (2.9)$$

which is already symmetric.

The joint probability is given by:

$$|\Psi(1, 2)|^2 = (|f_A|^2 + |f_B|^2 + f_A \bar{f}_B e^{ip_1(r_B - r_A)} + f_B \bar{f}_A e^{ip_1(r_A - r_B)}) \times \quad (2.10)$$

$$(|f_A|^2 + |f_B|^2 + f_A \bar{f}_B e^{ip_2(r_B - r_A)} + f_B \bar{f}_A e^{ip_2(r_A - r_B)})$$

If the two sources are coherent, their relative phase does not change and the average of the product of the two "phases" is non-zero:  $\langle f_A \bar{f}_B \rangle = f_A \bar{f}_B$  and  $|\Psi(1, 2)|^2 = |\Psi(1)|^2 |\Psi(2)|^2$

The chaotic limit corresponds to assuming that the amplitudes  $f_i$  for radiation from each point in space fluctuate wildly so that the average of  $(f_A \bar{f}_B)$  is zero. Hence

$$|\Psi(1, 2)|^2 = (|f_A|^2 + |f_B|^2)^2 + 2|f_A|^2|f_B|^2 \cos[(p_2 - p_1)(r_A - r_B)] \quad (2.11)$$

All other terms in the product in equation 2.10 like  $|f_A|^2 f_A \bar{f}_B e^{ip_2(r_B - r_A)}$  or  $(f_A \bar{f}_B)^2 e^{i(p_1 - p_2)(r_A - r_B)}$  a.s.o. are zero in the average. As the correlation function has the form  $R_{BE} = \frac{P(1,2)}{P(1)P(2)}$  where

$P(1, 2) = \langle |\Psi(1, 2)|^2 \rangle$ ,  $P(1) = \langle |\Psi(1)|^2 \rangle$  and  $P(2) = \langle |\Psi(2)|^2 \rangle$  there is no enhancement of the correlation function in the case of coherence but the correlation function is enhanced with an interference term for chaotic emission as  $P(1)P(2) = (|f_A|^2 + |f_B|^2)^2$  in that case.

Coherent emission will reduce the interference effect which is also known in laser optics for the degree of second order coherence.

This derivation was made for two emitters of pions placed at the points  $r_A$  and  $r_B$ . For a real source and an infinite number of emitters the most general expression for the correlation function is [10]

$$R(T) = 1 + \lambda |\tilde{\rho}(T)|^2 \quad (2.12)$$

This gives a physical meaning to  $\lambda$  as a "coherence factor" or "chaoticity parameter" taking values  $0 \leq \lambda \leq 1$ .  $\lambda = 1$  corresponds to a complete chaotic source while complete coherence is expressed by  $\lambda = 0$ . In the literature this factor  $\lambda$  is sometimes introduced as an empirical scale factor in order to improve the fit of the correlation function to the data. It is important to note, that in high energy physics other effects than a simple degree of coherence of the production mechanism can reduce the strength of the enhancement of the correlation towards smaller  $T$  (for instance resonance production).

### 2.3.2 The Goldhaber parametrization

The space-time distribution  $\rho(r)$  proposed by Goldhaber *et al.* [22] corresponds to particle emission from a Gaussian distributed source in four dimensions. It is nowadays the most extensively used parametrization:

$$\rho(x) = \rho(0) \exp\left(-\frac{x^2}{2r^2}\right). \quad (2.13)$$

which leads to the following correlation function:

$$R(T) = 1 + \lambda \exp(-r^2 T^2). \quad (2.14)$$

The width  $r$  is interpreted as the size  $R$  of the production area according to  $R = \hbar c r = 0.197r$  fm and  $T^2$  is related to the invariant mass  $M$  of the pion pair by

$$T^2 = -(p_1 - p_2)^2 = M^2 - 4m_\pi^2. \quad (2.15)$$

The extension of the enhancement in  $T$  is proportional to  $R^{-1}$  in agreement with the Heisenberg uncertainty principle.

In order to take long-range charge correlations (e.g. of kinematical origin) into account a slightly modified function can be used :

$$R(T) = N(1 + \delta T)(1 + \lambda \exp(-r^2 T^2)). \quad (2.16)$$

where  $N$  is a global normalization factor. As most other experiments we will use this parametrization too in the comparison to our data.

## 2.4 String model approach to Bose–Einstein correlations

Models of fragmentation are phenomenological approaches to multiparticle dynamics and production processes in high energy physics.

The first model of Feynman and Field based on an iterative algorithm for the mechanism of particle production was developed in 1978 ([13]). Further models improved the description of experimental data and the “string model of fragmentation” developed by the theoretists from the University at Lund (Sweden) in 1980 is one of these models (see [33] for a comprehensive overview). Its underlying idea goes back to 1974 when Artru and Menessier applied the idea of colored strings to multiple production of hadrons [34]. The string model has recently been applied to the Bose–Einstein correlations. In [10] M. G. Bowler used the Artru–Menessier string model to explain BEC between like pion pairs. This was further improved by B. Andersson and W. Hofmann in [35] via the area dependence of Wilson loop integrals where the correlation length in momentum space can be related to the string tension. X. Artru and M.G. Bowler finally quantized the classical Artru–Menessier string model with a Feynman sum over histories method yielding a propagation amplitude which can account for the observed BEC. The model reproduces naturally the quantum mechanical second order interference.

### 2.4.1 The Lund string model

The basic idea is that the color field of the strong interaction between an outgoing quark pair  $q\bar{q}$  is compressed in a flux tube which contains a constant amount of energy  $\kappa$  per unit length ( $\kappa \sim 1 \text{ GeV/fm} = 0.2 \text{ GeV}^2$ ). Hence the potential between a  $q\bar{q}$  pair rises linearly. In a process where a  $q\bar{q}$ -pair is produced quark  $q$  and anti-quark  $\bar{q}$  go out in opposite directions with a color flux between them as indicated in Figure 2.3. In order to model the dynamics of fragmentation, a probability is introduced for the string to break up into pieces corresponding to the creation of a new  $q\bar{q}$ -pair. This can be treated as a tunneling phenomenon with a production probability proportional to  $\propto e^{-\frac{\pi m_t^2}{\kappa}}$  where  $m_t^2 = m^2 + p_t^2$ .

Quarks are supposed to have a transverse momentum  $\vec{p}_t$  which is randomly distributed according to a Gaussian distribution. The distribution of longitudinal momentum is simulated by a fragmentation function  $f(z)$  where  $z$  is the fraction of energy taken by the hadron. The primary quark  $q$ , going out along the  $+x$  axis (fig. 2.3) initially carries the “lightcone momentum”  $W_0 = E_0 + p_{x0}$ . From this  $W_0$  the first hadron  $q\bar{q}_1$  (composed of the original and a new quark) takes the fraction  $z_1 = \frac{(E+p_x)q\bar{q}_1}{W_0}$  leaving  $W_1 = (1-z_1)W_0$  to the remaining quark  $q_1$ , from which the second hadron  $q_1\bar{q}_2$  takes a fraction  $Z_2$  etc. The distribution function  $f(z)$  is related to the probability for the string to break up and can have several forms.

The general final form of the fragmentation function given in [33] is:

$$f(z) = N_{\alpha\beta} \left(\frac{1}{z}\right) z^{a_\alpha} \left(\frac{1-z}{z}\right)^{b_\beta} e^{-\left(\frac{bm_t^2}{z}\right)} \quad (2.17)$$

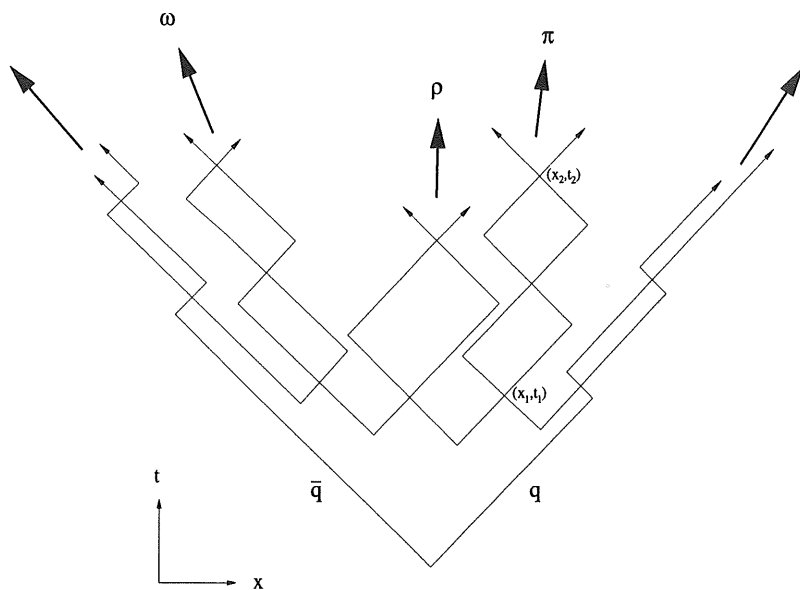


Figure 2.3: Space-time development of hadronization in the Lund-string model of fragmentation

where  $\alpha$  and  $\beta$  are the flavor of the quark and anti-quark respectively and  $a_{\alpha}, b_{\beta}$  and  $b$  are free parameters.  $N_{\alpha\beta}$  is a normalization factor. The flavor dependence is given as an exponential of the mass of the hadrons and has an important implication on the probability to produce a final state with  $n$  particles. The equation of motion of two massless quarks interacting via a linearly rising potential  $V = \kappa |x|$  (see [34]) is

$$\frac{dp}{dt} = \pm\kappa \quad \text{and} \quad \frac{dE}{dx} = \pm\kappa \quad (2.18)$$

The evolution of a meson in space-time is thus "yo-yo like" and the return points  $(x_1, t_1), (x_2, t_2)$  of the  $q\bar{q}$ -pair are related to the total energy  $E$  and momentum of the meson via

$$E = \kappa(x_1 - x_2), \quad p = \kappa(t_1 - t_2) \quad (2.19)$$

The mass of a meson can therefore be written as

$$m^2 = \kappa^2(x_1 - x_2)^2 - \kappa^2(t_1 - t_2)^2 \quad (2.20)$$

The action of a classical string is given by

$$S = -\kappa \int d\Sigma \quad (2.21)$$

where  $\int d\Sigma$  is the invariant space-time area spanned by the string and  $\kappa$  is the string tension. Bearing in mind the formalism of path integrals one can write the amplitude for string propagation as

$$A_{12} \propto e^S = e^{-\kappa \int d\Sigma} \quad (2.22)$$

The amplitude associated with each configuration has a phase equal to the area enclosed multiplied by the string tension. The probability for the production of a  $n$  particle configuration is suppressed by an exponential of the space-time area enclosed by the string field. This property of the fragmentation model, as will be seen, allows the incorporation of quantum interference in the string model.

#### 2.4.2 String model of the Bose-Einstein correlations

In order to incorporate the real quantum behavior of the microscopic nature in string models of fragmentation, a semi-classical description of phase space been proposed [35]. The probability for a particular final state with  $n$  particles is given by

$$Prob. = (\text{phasespace}) \cdot e^{-bA} \quad (2.23)$$

where  $A$  is the area spanned by the string in space-time. The exponential of the area was interpreted by Andersson and Hofmann [35] as the square of a matrix element  $M$ . Considering the possibility that the string state decays one writes  $S$  as

$$S = \left(\kappa + \frac{ib}{2}\right)A \quad (2.24)$$

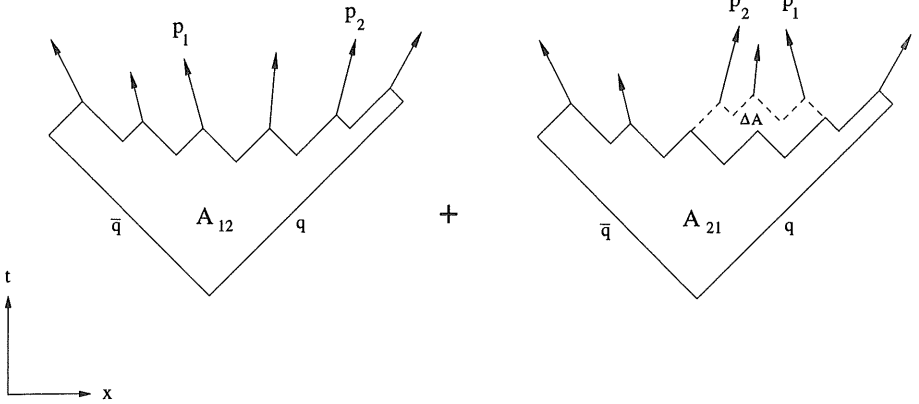


Figure 2.4: Two string configurations which lead to the same final state. The areas of the first closed quark loops are different and the amplitudes have different phases. The phase difference is proportional to the area  $\Delta A = A_{21} - A_{12}$  which arise under the interchange of mesons 1 and 2.

where the imaginary term  $\frac{i\hbar}{2}$  has been introduced. The production of two identical bosons 1,2, for example pions, can occur in several ways. As shown in fig. 2.4, the final state obtained after the interchange of two of the identical bosons remains the same (see fig 2.4). The amplitude should therefore consider the terms describing the ways to obtain the same array of particles (addition of the amplitudes), thus

$$M \propto e^{i(\kappa + \frac{i\hbar}{2})A_1} + e^{i(\kappa + \frac{i\hbar}{2})A_2} \tag{2.25}$$

where  $A_1$  ( $A_2$ ) represents the area of a  $n$ -particle configuration when particles 1 and 2 are un-permuted (permuted). This amplitude gives

$$Prob. \propto |M|^2 \propto [e^{-bA_1} + e^{-bA_2}][1 + \frac{\cos(\kappa\Delta A)}{\cosh(\frac{b\Delta A}{2})}] \tag{2.26}$$

where an area difference  $\Delta A = A_1 - A_2$  appears as is shown in figure 2.4. Using the relationship given in equation 2.19 one can express this area  $\Delta A$  in terms of the momenta of the particles 1 and 2 and of the intermediate state  $I$ :

$$\Delta A = |A_1 - A_2| = \frac{|\vec{p}_1 E_2 - \vec{p}_2 E_1 + (\vec{p}_1 - \vec{p}_2) E_I - (E_1 - E_2) \vec{p}_I|}{\kappa^2} \tag{2.27}$$

where  $(E_i, p_i)$  is the two-momentum of bosons  $i$  and  $(E_I, p_I)$  is the two-momentum of the intermediate state. The enhancement of the probability which arises from this  $\Delta A$  can be



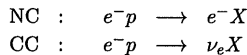
computed as a function of the relative momentum variable  $T$ . This computation was done in [35]. The relative phase of the two amplitudes shown in figure 2.4 is very sensitive to the string configuration, unless the momenta of the two exchanged pions are small. It turns out [11] that permutations which generate a large area are exponentially suppressed. In this case the difference in the four momenta of the two interchanged pions is not small. This behavior explains the characteristic rise of the correlation function towards smaller relative momenta  $T$  of two identical pions. The appearance of partial coherence was discussed by Bowler in [52]. There it is shown that partial coherence arises when one of the like charged pions is a daughter of a resonance.

## Chapter 3

# Deep inelastic electron scattering

### 3.1 Deep inelastic scattering

In a deep inelastic scattering experiment the incoming electron scatters with the proton by exchanging a gauge boson and converts to a charged or uncharged lepton on the charge of the gauge boson. In deep inelastic scattering the proton is not conserved. Its partons form a hadronic final state  $X$  which can include jets. If the gauge boson is an uncharged  $\gamma$  or  $Z^0$  the event is called a neutral current (NC) event. The lepton in the final state is an electron which can be measured in the detector. In the case of an exchange of a gauge boson  $W^\pm$  the event is called a charged current (CC) event and the scattered lepton is a neutrino which cannot be directly measured in the detector.



The Feynman diagram of fig. 3.1 summarizes these most basic reactions in deep inelastic scattering.

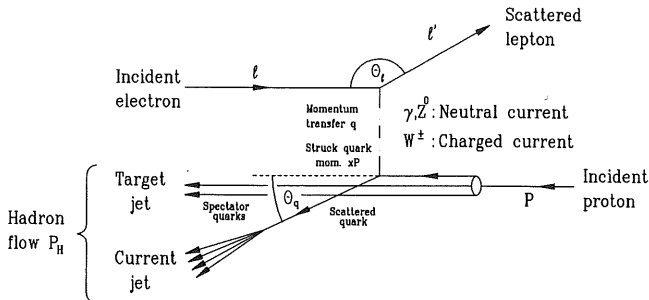


Figure 3.1: Feynman diagram for basic processes in deep inelastic scattering.

The kinematics of the  $ep$  scattering is fully determined by two kinematical variables at a fixed known center of mass energy  $\sqrt{s}$  of the  $ep$  system. Two of the following Lorentz invariant quantities are most frequently used:

- The center of mass energy  $\sqrt{s}$  of the  $ep$  system

$$s \equiv (p_e + p_p)^2 \approx 4E_e E_p \quad (3.1)$$

where  $p_e$  and  $p_p$  are the momenta and  $E_e$  and  $E_p$  the energies of the electron and the proton.

- The four momentum transfer  $Q$  of the gauge boson, which describes its virtuality,

$$Q^2 \equiv -q^2 = -(p_e - p_{e'})^2 \approx 2p_e p_{e'} \quad (3.2)$$

- The invariant mass  $W$  of the hadronic final state  $X$

$$W^2 \equiv (q + p_p)^2 = m_p^2 + q^2 + 2p_p q \quad (3.3)$$

- The energy transfer  $\nu$  in the proton rest frame

$$\nu \equiv \frac{q \cdot p_p}{m_p} \quad (3.4)$$

Another frequently used way to describe the  $ep$  system is to use the dimensionless scaling variables  $x$  and  $y$ . They are defined as follow

$$x \equiv \frac{Q^2}{2(q \cdot p_p)} = \frac{Q^2}{2m_p \nu} \quad (3.5)$$

$$y \equiv \frac{q \cdot p_p}{p_e \cdot p_p} = \frac{\nu}{\nu_{\max}} \quad (3.6)$$

The variable  $x$  is the Bjorken scale variable. It describes the fraction of the proton momentum the elastic scattered parton carries in the infinite momentum frame, where the proton recoils with high momentum against the electron. The inelasticity of the scattering is described by  $y$ , which is equal to the ratio of the actual to the maximum energy transfer in the proton rest frame ( $\nu_{\max} = \frac{s}{2m_p}$ ). Both quantities range from 0 to 1. Neglecting the masses of electron and proton, the variables  $x$  and  $y$  are connected as follows

$$Q^2 = x \cdot y \cdot s \quad (3.7)$$

The squared invariant mass of the hadronic final state  $W^2$  is given by

$$W^2 = Q^2 \cdot \frac{1-x}{x} + m_p^2 \quad (3.8)$$

There are different procedures to experimentally determine these variables. In NC events the kinematics can be calculated by measuring the polar angle  $\vartheta_e$  of the scattered electron with respect to the outgoing proton direction and the energy of the scattered electron  $E_e'$

$$y_e = 1 - \frac{E_e'}{E_e} \cdot \sin^2 \left( \frac{\vartheta_e}{2} \right) \quad (3.9)$$

$$Q_e^2 = 4E_e E_e' \cdot \cos^2\left(\frac{\vartheta_e}{2}\right) . \quad (3.10)$$

Another procedure, independent of the measurement of the electron, is the method of Jacquet-Blondel [62]. It is based on the measurement of the hadronic final state. It is used for CC events and for events where the electron escapes detection or is measured only with a poor resolution

$$y_{JB} = \frac{1}{2E_e} \cdot \sum_{\text{hadrons } i} (E_i - p_{z_i}) \quad (3.11)$$

$$Q_{JB}^2 = \frac{1}{1 - y_{JB}} \left( \sum_{\text{hadrons } i} p_{\vec{t}_i} \right)^2 . \quad (3.12)$$

The summation includes all hadrons measured in the detector. The variables  $E_i$ ,  $p_{z_i}$  and  $p_{\vec{t}_i}$  are the energy, the longitudinal and transverse momenta of the hadron  $i$ .

For the majority of DIS events the final state hadronic energy flow is spread between the directions of the struck quark and the proton remnant. Due to the high incident proton momentum at HERA, the directions of these two systems are generally very different in the laboratory. Hence detailed studies of the energy flow associated with them and their interrelation become possible.

### 3.2 Diffractive scattering

Recent measurements at HERA [63],[64] in the low  $x_{Bjorken}$  kinematic range  $5 < Q^2 < 120$  GeV<sup>2</sup> and  $10^{-4} < x_{Bjorken} < 10^{-2}$  have demonstrated the existence of a distinct class of events in which there is no hadronic energy flow in an interval of (laboratory frame) pseudo-rapidity  $\eta$  adjacent to the proton beam direction. A natural interpretation of these so called "rapidity gap" events is based on the hypothesis that the deep-inelastic scattering process involves the interaction of the virtual boson probe with a colorless component of the proton. Hence there is no chromodynamic radiation in the final state immediately adjacent to the direction of the scattered proton or any proton remnant. Observed distributions of such events are found to be consistent with simulations based on models in which the virtual boson-proton interaction is diffractive [63], that is in which the colorless component of the proton is hypothesized to be a pomeron ( $\mathbb{P}$ ) and the virtual boson-proton interaction may be understood as  $\mathbb{P}$  exchange. The observation of these rapidity gap events in DIS means that a measurement of any short distance sub-structure of this colorless component of the proton is possible, and thus, if the process is diffractive, of the  $\mathbb{P}$ . Figure 3.2 represents such a diffractive process in deep inelastic electron-proton scattering where the produced hadronic system X is well separated in phase space from the quasi-elastically scattered proton. The process proceeds by the emission of a pomeron from the proton with a small squared momentum transfer and with a fraction  $x_P = 1 - x_p \leq 0.1$  of the proton momentum. This pomeron then interacts with the electron in a large momentum transfer process, described by the usual kinematic variables ( $Q^2$  and  $x_{Bjorken}$ ) described above, and produces the hadronic final state X. A separate measurement of Bose Einstein correlations with such a diffractive DIS data-sample has been done [65].

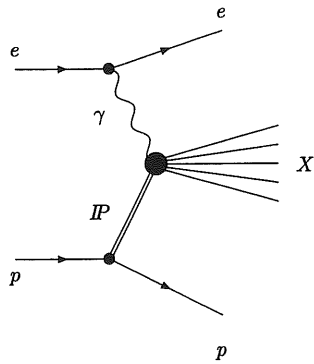


Figure 3.2: General diagram of a diffractive deep inelastic electron-proton scattering with produced hadronic system  $X$  well separated in phase space from the quasi-elastically scattered proton..

## Chapter 4

# The H1 detector

### 4.1 The electron proton storage ring HERA

The storage ring HERA is the first electron proton collider and came into operation in 1991. An overview of the accelerator facility is given in fig. 4.1.

The electrons and the protons are accelerated and stored in two separated pipes in a ring 15 to 20 m underground. The earlier accelerators LINAC, DESY and PETRA were in some of their parts modified and used as preaccelerators.

The electrons are produced thermo electrically and accelerated to an energy of 450 MeV with the linear accelerator LINAC II. They are then injected into the electron synchrotron DESY II where their energy is increased to 7.5 GeV. In PETRA II they achieve an injection energy of 14 GeV for HERA. The electron ring in HERA is designed for energies up to 30 GeV and can store the electrons over several hours. The required magnetic field of 0.165 T is achieved with normally conducting magnets in contrast to the proton ring in HERA. The electrons lose 127 MeV energy at each turn through synchrotron radiation. The total power loss of the accelerator system is about 6.5 MW.

The protons are derived from negatively charged hydrogen atoms. They are produced in an ion source with an energy of 18 keV, focused with a high frequency quadrupole magnet and accelerated to an energy of 500 keV. At the exit of the linear accelerator LINAC III at an energy of 50 MeV the protons are stripped of their electrons by a thin foil when they enter the proton synchrotron DESY III. The protons then reach PETRA II with a momentum of 7.5 GeV/c and are accelerated to the injection energy of 40 GeV for the proton ring at HERA in the same pipe as the electrons but in a counter-clockwise rotating direction. In HERA they are accelerated in separate pipes to the design energy of 820 GeV. The superconducting bending magnets achieve a magnetic field of 4.65 T. The superconductors are cooled with liquid helium at a temperature of 4.2 K from a special cooling system of DESY. The required power is less than 20 kW.

There are four locations in HERA where the electrons and the protons can collide. The center of mass energy of the  $ep$  system is  $\sqrt{s} = 314$  GeV at nominal beam energies. In comparison to previous  $ep$  scattering experiments with a fixed target the square of maximum four momentum transfer at HERA is  $Q_{\max}^2 \approx s/c^2 = 98400 \text{ GeV}^2/c^2$  i. e. about two orders of magnitude higher.

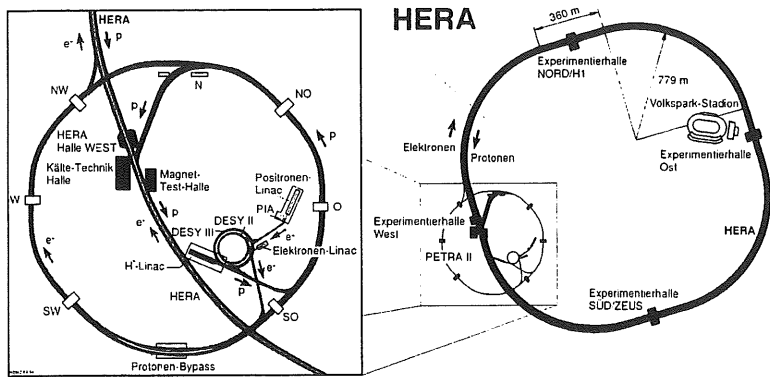


Figure 4.1: The storage ring HERA on the right with its preaccelerators LINAC, DESY and PETRA on the left.

To get the same center of mass energy with a fixed target experiment it would be necessary to accelerate the electrons to an energy of 52 TeV which is not possible at present. With HERA we have therefore access to an entirely new kinematical regime.

In 1994 the electron beam had an energy of 27.5 GeV corresponding to a center of mass energy  $\sqrt{s} = 300.33$  GeV and a square of maximum four momentum transfer  $Q_{\max}^2 \approx s/c^2 = 87576$  GeV<sup>2</sup>/c<sup>2</sup>. The accelerator is able to run with 220 bunches of each kind. To achieve the design luminosity of  $1.5 \cdot 10^{31}$  cm<sup>-2</sup>s<sup>-1</sup> HERA has to run with 210 bunches each containing  $0.8 \cdot 10^{13}$  electrons and  $2.1 \cdot 10^{13}$  protons. In this situation the currents are 58 mA and 163 mA respectively. The electron and proton beams intersect at each crossing point every 96 ns. From the total cross section one expects only  $10^5$  ep interactions a second, whereas there is about 10 times more interactions between protons and gas molecules in the beam pipe at the interaction zone of the detectors.

The radial extensions are  $\sigma_{xe} = 280$   $\mu$ m and  $\sigma_{ye} = 37$   $\mu$ m for the electron beam and  $\sigma_{xp} = 265$   $\mu$ m and  $\sigma_{yp} = 84$   $\mu$ m for the proton beam. The profile of the beams are of similar dimensions. That is not the case for the length of the bunches. The proton bunches are more than 10 times longer than the electron bunches and therefore the interaction zone extends over 50 cm (1993 beam conditions). These parameters are summarized in Table 4.1.

At two of the four interaction zones, experiments were installed in spring 1992. The experiment H1 is installed in the north hall, the experiment ZEUS [4] in the south hall. Two new experiments, HERA-B [2] and HERMES [3], are located in the remaining two interaction zones.

In order to improve the life of the beam the HERA preaccelerators were switched to positrons in July 1994. Thus the data used in the analysis presented here are dealing with positron proton collisions.

parameter	<i>p</i> beam	<i>e</i> beam	<i>p</i> beam	<i>e</i> beam	unit
	design		1994		
Length	6336		6336		m
Beam energy	820	30	820	27.55	GeV
Injection energy	40	14	40	12	GeV
Number of bunches	210	210	94	90	
Particles per bunch	$10 \cdot 10^{10}$	$3.8 \cdot 10^{10}$	$3 \cdot 10^{10}$	$3.6 \cdot 10^{10}$	
Current per bunch	760	290	210	265	$\mu\text{A}$
<i>B</i> field	4.68	0.165	4.68	0.149	T
$\sigma_x$ at interaction point	0.29	0.26	0.27	0.28	mm
$\sigma_y$ at interaction point	0.07	0.02	0.08	0.04	mm
$\sigma_z$ at interaction point	110	8	200	10	mm
Center of mass energy	314		300.33		GeV
Luminosity	$1.5 \cdot 10^{31}$		$0.15 \cdot 10^{31}$		$\text{cm}^{-2}\text{s}^{-1}$
HF frequency	52.05	499.7	52.05	499.7	MHz
	208.2		208.2		

Table 4.1: Summary of HERA parameters [1].

#### 4.1.1 The H1 Detector

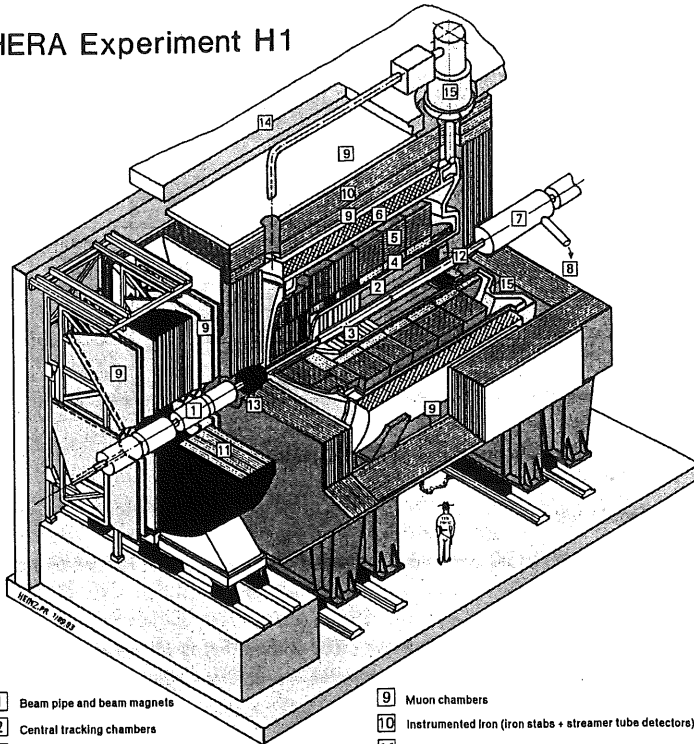
This chapter briefly describes the H1 detector. A detailed discussion of the H1 detector can be found in [1].

Figure 4.2 gives a schematic view of the detector. The *z* direction is identical with the proton flight direction. Starting from the interaction point the detector consists of the following components:

- **Central Tracker [2]** : It consists of six cylindrical chambers which cover a range in theta of  $20^\circ \leq \vartheta \leq 170^\circ$ . They are used for reconstruction of charged particles, particle identification and triggering.
- **Forward Tracker [3]** : It consists of three identical supermodules with drift and proportional chambers. It completes the tracking system in the forward direction and measures particles at a polar angle  $7^\circ \leq \vartheta \leq 20^\circ$ .
- **Liquid Argon Calorimeter (LAC) [4] [5]** : It surrounds the tracking system in the forward and barrel region. It comprises an electromagnetic part with lead absorbers which measures the electron energy with a resolution of the order of  $12\%/\sqrt{E} [\text{GeV}]$  and a hadronic part with stainless steel absorber. Its resolution is about  $55\%/\sqrt{E} [\text{GeV}]$ . The absolute energy scale for the electromagnetic part is presently known within 3 % for the backward region and 5 % for the forward region. For the hadronic part, the absolute energy



## HERA Experiment H1



- |   |   |    |  |
|---|---|----|--|
| 1 | Beam pipe and beam magnets                | 9  | Muon chambers  |
| 2 | Central tracking chambers                 | 10 | Instrumented Iron (iron stabs + streamer tube detectors) |
| 3 | Forward tracking and Transition radiators | 11 | Muon toroid magnet                                       |
| 4 | Electromagnetic Calorimeter (lead)        | 12 | Warm electromagnetic calorimeter                         |
| 5 | Hadronic Calorimeter (stainless steel)    | 13 | Plug calorimeter (Cu, Si)                                |
| 6 | Superconducting coil (1.2T)               | 14 | Concrete shielding                                       |
| 7 | Compensating magnet                       | 15 | Liquid Argon cryostat                                    |
| 8 | Helium cryogenics                         |    |  |
- } Liquid Argon

Figure 4.2: The H1 detector with its main components.

scale is measured within 7 %. In the very forward region the calorimeter is completed by a silicon-copper plug. It measures the energy deposition at  $0.6^\circ \leq \vartheta \leq 3^\circ$  between the LAC and the beam pipe.

- **Backward Electromagnetic Calorimeter (BEMC) [12]** : It completes the energy deposition measurement in the backward direction ( $151^\circ \leq \vartheta \leq 177^\circ$ ). This lead scintillator calorimeter provides a good electromagnetic but a poor hadronic energy measurement. Just in front of the calorimeter is the backward multiwire proportional chamber giving an accurate space point for tracks. The energy scale for electrons is known to an accuracy of 2 %. Its resolution is about  $10 \%/ \sqrt{E} [\text{GeV}] + 42 \%/ E [\text{GeV}]$ .
- **Time of Flight System (ToF)**: 2 m upstream of the interaction zone just behind the BEMC two scintillator walls are installed. The accurate time resolution of 2 ns allows the identification of particles crossing the detector from outside (upstream).
- **Magnet [6] [7]** : The superconducting solenoid with a diameter of 6 m, surrounds the H1 calorimeter, providing a homogeneous field of 1.2 T parallel to the beam axis in the tracking region of the H1 detector. At the proton entrance side of the solenoid, the compensating coil is located. Its purpose is to provide a longitudinal field integral  $\int B_z dz$  opposite to that of the main magnet. This is to compensate the solenoid's influence on the beam.
- **Muon System [9] [10]** : Muons escaping the H1 detector are recorded in the instrumented iron, on an octagonal yoke surrounding the solenoid. It also allows measurement of the hadronic energy leakage. The system is completed by a forward muon system with its own toroidal magnet to measure high energy muons in the energy range  $5 \text{ GeV} \leq E_\mu \leq 200 \text{ GeV}$  and muon chambers outside of the iron yoke.
- **Luminosity System**: It consists of two crystal calorimeters for the measurement of collinear photons and electrons scattered at very small angles. The photon detector is installed at  $z = -103 \text{ m}$ , the electron detector (*e*-tagger) at  $z = -33 \text{ m}$ . The system provides an accurate measurement of the luminosity using the Bethe-Heitler process  $ep \rightarrow e\gamma$  which is proportional to the luminosity and has a well known cross section. Furthermore it measures electrons scattered at very small angles ( $\vartheta \leq 5 \text{ mrad}$ ) and photons from initial state bremsstrahlung.

#### 4.1.2 The H1 Tracking System

A schematical view of the tracking system of H1 is given in Figures 4.3 and 4.4. The innermost chamber is a double layer multiwire proportional chamber (CIP) [6] giving a fast but rough  $\varphi$  and  $z$  position of a track. It is followed by a  $z$ -drift chamber (CIZ) with a spatial  $z$  resolution of  $300 \mu\text{m}$ . Two jet chambers (CJC) [5] measure the  $r$ - $\varphi$  projection of a track within an accuracy of  $210 \mu\text{m}$ . The inner chamber (CJC1) is divided into 30  $\varphi$ -sectors each with 24 sense wires, the outer chamber (CJC2) into 60  $\varphi$ -sectors with 32 layers. The sense wires are stretched parallel to the beam axis. The cells are tilted by  $30^\circ$  in order to give optimal track reconstruction. The

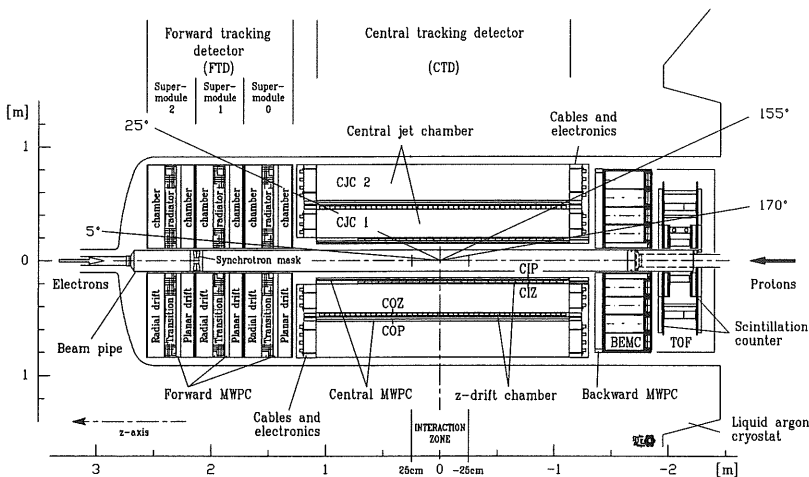


Figure 4.3: Side view of the H1 tracking system.

tilt compensates the Lorentz angle of the drifting electrons in the magnetic field. Thus the drift direction is almost perpendicular to the track which leads to a better spatial resolution. Further, all tracks with a transverse momentum  $p_t$  above 400 MeV/c cross at least once the sense wire plane. For this sense wire, the drift distance for the drift electrons is as short that the drift time is shorter than 50 ns. This property allows the assignment of a bunch crossing time to each track. They not only cross the sense wire plane, they also cross the cell boundaries which leads to the possibility of distinguishing between hits and their mirror hits. For short track segments the ambiguity is resolved with staggered sense wires. An overview of the parameters of CJC1 and CJC2 is given in Table 4.2. Between the two jet chambers another z-drift chamber (COZ) and two layers of a multiwire proportional chamber (COP) are placed. The signals of CIP and COP are only used for triggering. Taking into account the asymmetry in electron and proton beam energies there is a forward tracking system to detect tracks at small angle  $\vartheta$ . It consists of three identical modules each with a multiwire proportional chamber (FPC), a radial drift chamber and a planar drift chamber. The FPC gives fast signals for triggering purpose while the radial drift chamber gives an accurate measurement in  $r$ - $\varphi$  plane ( $\sigma_{r\varphi} = 200 \mu\text{m}$ , design value) and the planar drift chamber measures the  $x$ - $y$  projection within  $170 \mu\text{m}$  (design value). In the backward direction in front of the BEMC are installed four layers of a multiwire proportional chamber (BPC). Normally hits in three out of four planes are required which lead to an efficiency of 89 % [7] in 1993.

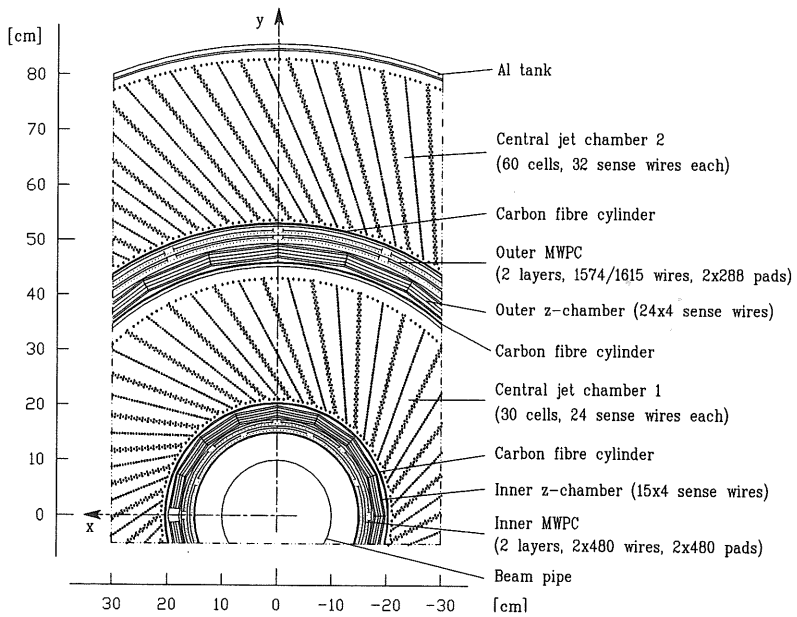


Figure 4.4: Radial view of the H1 tracking system.

parameter	CJC1	CJC2	unit
Active length	2200		mm
Inner radius $R_i$	203	530	mm
Outer radius $R_o$	451	844	mm
Number of cells	30	60	
Number of sense wires per cell	24	32	
Number of potential wires per cell	50	66	
Number of filed wires per cell	10	10	
Number of cathode wires per cell	49	65	
Sense wire distance	10.16		mm
Maximum drift distance at $R_i$	22.9	28.5	mm
Maximum drift distance at $R_o$	44.5	43.1	mm
Gas mixture Ar/C <sub>2</sub> H <sub>6</sub>	50 : 50		%
Sense voltage	1170		V
Field gradient	120		V/mm
Drift velocity	$\approx 54.2$		$\mu\text{m}/\text{ns}$
Lorentz angle	$\approx 42$		°
$\sigma_{r\phi}$	145		$\mu\text{m}$
$\sigma_z$	25		mm
$\sigma_{dE/dx}$	10		%
Double hit resolution	2.5		mm

Table 4.2: Central jet chamber parameters [5].

## Chapter 5

# The inner $z$ -drift chamber

### 5.1 The hardware

Two thin drift chambers, the central inner and outer  $z$ -chambers (CIZ, COZ) (see Chapter 4 for an overview) surround the inner half of the jet chamber and complement the measurement of charged track momenta. These two chambers deliver track elements with typically  $300 \mu\text{m}$  resolution in  $z$  and 1 to 2 % of  $2\pi$  in  $\phi$ .

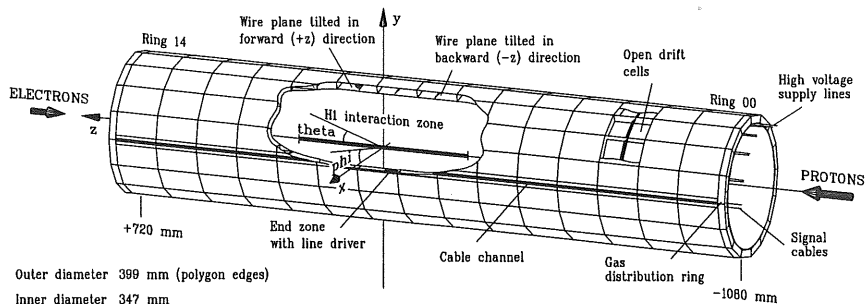


Figure 5.1: The inner  $z$ -drift chamber

This requires a drift direction parallel to the beam axis and sense wires running perpendicular to the beam axis on the surface of two cylinders with 180 and 460 mm average radii. Linking these track element to those obtained from the jet chamber with accurate  $r\phi$  and moderate  $z$ -information gives the final accuracy on both the longitudinal as well as the transverse momentum components. A double track resolution of a few mm, high efficiency and low chamber mass were further design criteria for CIZ. The CIZ uses the inner carbon fiber wall of the CJC for closing its gas volume. The polar angle covered by the CIZ is  $16^\circ < \vartheta < 169^\circ$ . The length of the full detector is 2200 mm reaching from -1030 mm to +1080 mm in the H1 coordinate system. Fifteen rings, each 12 cm long containing sixteen drift cells, are arranged on a regular polygon.

	unit	value
active length $\Delta z$	mm	1800
active zone starts at $z$	mm	-1080
mechanical length $\Delta z$	mm	2254
total length $\Delta z$	mm	2467
thickness $\Delta r$	mm	20
chamber starts at $z$	mm	-1373
inner diameter	mm	347
outer diameter	mm	400
number of drift-cells (rings) in $z$		15
number of $\phi$ -sectors		16
number of sense wires per ring		4
number of potential wires per ring		3
mean wire length	mm	1120
drift cell length $\Delta z$	mm	120
maximum drift distance $\Delta z$	mm	61.25
sense wire material		Elgiloy
sense wire resistance	k $\Omega$ /m	3.0
sense wire diameter	$\mu$ m	20
potential wire material		Au
potential wire diameter	$\mu$ m	120
wire tension	N	0.2
dead zone in $\phi$ (readout channel)	deg (%)	7.5 (2.1)
dead zone in $\phi$ (wire support)	deg (%)	14.4 (4.0)
dead zone in $z$ (cell walls in active zone)	%	1.6
radiation length in active zones	% $X_0$	0.6
radiation length averaged	% $X_0$	1.2
gas mixture	%	Ar(70)
	%	C <sub>2</sub> H <sub>6</sub> (30)
cathode voltage	V	4300
potential wire voltage	V	2150
field gradient	V/mm	52.7
drift velocity	mm/ $\mu$ s	50

Table 5.1: CIZ parameters

The independent rings are separated by printed circuit boards on each side serving as the cathode plane. These walls, the axial dividers extending from the corners of the polygon and the Kapton foil with the field forming strips are glued to the chamber body. The cells are closed electrically with another foil identical to the one on the bottom which is glued to a removable cover. There are four anode wires and three potential wires running around the circumference in each ring.

The sense wire planes are tilted by  $45^\circ$  from the normal to the chamber axis, with the first nine cells in backward direction tilted backward and the last six in forward direction tilted forward, i.e. following the direction of the tracks crossing the respective cells. As shown in picture 5.3 this tilt produces a distortion of the equipotential wire lines resulting in a non-uniform distribution of the charge collected on the four wires and an equivalent tilt of the isochrones. In the orientation shown in Figure 5.3 wire # 4 collects charge only when a track crosses to the left of the sense wire plane and wire # 1 collects charge only if a track crosses to the right. Both collect roughly 60 % of the total charge, while wires # 2 and # 3 collect about 20 % for both sides. This unusual wire arrangement hence solves the left-right ambiguity automatically without a need for wire staggering and furthermore dampens the dependence of the resolution on the crossing angle in particular for low crossing angles. Picture 5.2 (upper picture) summarizes the different possibilities of wire signals given with different tracks. Two, three or four hits can be the signal of a track depending where the track passed the chamber.

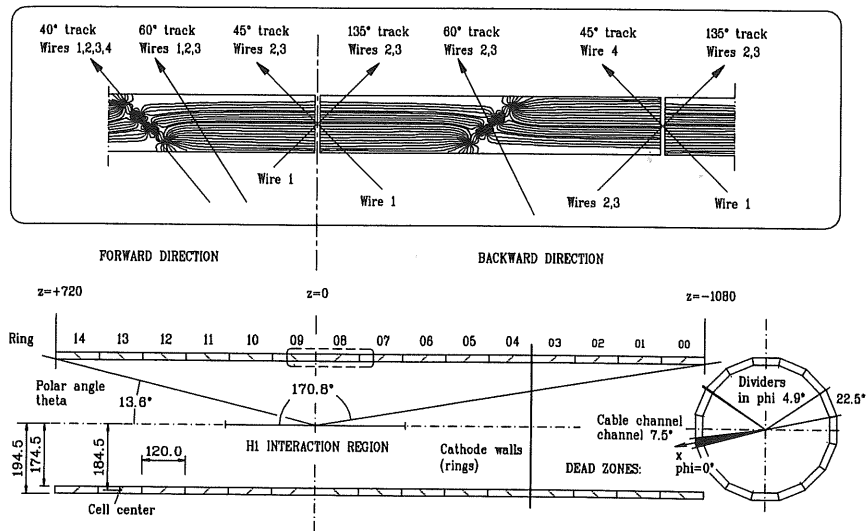


Figure 5.2: Schematic view of drift-cells in the middle of CIZ at  $z = 0$  (upper picture), and side and radial view of the whole chamber (lower picture)

The wires are soldered to both side walls of a 23 mm wide cable channel at  $\phi = 0^\circ$ . Here the signal wires are connected to line drivers and the potential wires to high voltage cables. A dedicated current monitoring system (see ref. [56] for details) was included into each potential wire supply line. It allows to measure the precise currents in the nA range. These wires control the gas amplification in the chamber. In this way the activity introduced by interaction products or stray beam can be monitored quite sensitively. More details on the results are given in a



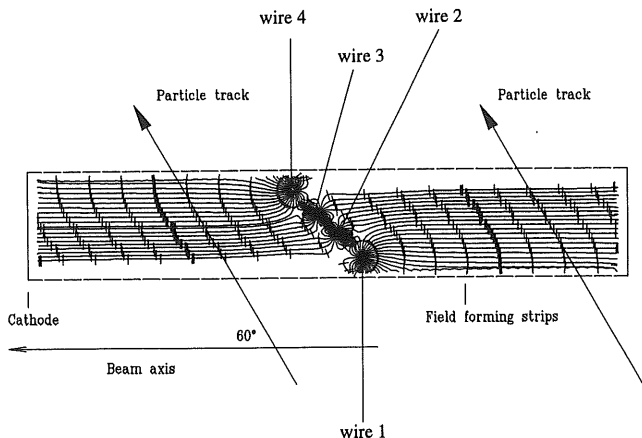


Figure 5.3: One single driftcell of CIZ. Shown are the drift-lines for the four wires with positions of equal drift times marked at fixed intervals (150 ns).

following chapter.

Damages on the sense wires seen during the repair in winter 93/94 forced a change of the gas mixture. Presently we run the chamber with an  $\text{ArC}_2\text{H}_6$  gas mixture, to which a small amount of water (0.4 %) for radiation damage protection is added. Further details and results are again given in the following chapters.

Some properties and technical data of the inner  $z$ -chamber are summarized in Table 5.1 which presents the status of CIZ at during the 1995 run period. A comprehensive description of the CIZ hardware can be found in [1] and in [55].

### 5.1.1 Current monitoring

Since the CIZ is the chamber closest to the interaction point, it senses most directly changes in beam tune and quality of the luminosity optics. When beams of high energies are lost, mainly during the filling of the HERA ring, a large amount of reaction products pass through the trackers and normally cause high voltage trips, i.e. the over-current monitor switches the voltages off. Our sensitive current monitor [56] provides a better safeguard against sudden increases in chamber current. After the successful tests with a single channel prototype a complete unit was assembled for all CIZ cells. It was found that the background level in CIZ depends only on the electron current in the machine and the current measured indicates also the quality of the beam tune, which varied often considerably. Actually the currents measured in the CIZ were often used to assess the beam conditions and to decide whether the chambers of the central tracker after a new fill of the HERA ring should be switched on or off.

### 5.1.2 Gas mixtures

The gas mixture has been changed several times in different running periods. During 1992 and 1993 an Argon/Methane (80/20%) mixture were used to run the chamber. Inspection of the chamber wires during the shutdown revealed serious ageing effects.(see [55] Chapter 10.5 and Figure 10.9–10.12). Such effects for this particular choice of gas had been seen in other experiments, and also on the inner wires of the central jet chamber and the forward tracker. During the winter shutdown 93/94 all sense and potential wires were replaced and the chamber was thoroughly cleaned. Starting in 1994 with an Ar/C<sub>2</sub>H<sub>6</sub> (50/50%) mixture we lost most of the efficiency due to a lower gas gain. The mean charge seen with the different mixtures (ArCH<sub>4</sub> 80% 20% and ArC<sub>2</sub>H<sub>6</sub> 50% 50%) can be seen in Figure 5.4. The data were taken during a cosmic run at the beginning of 1994.

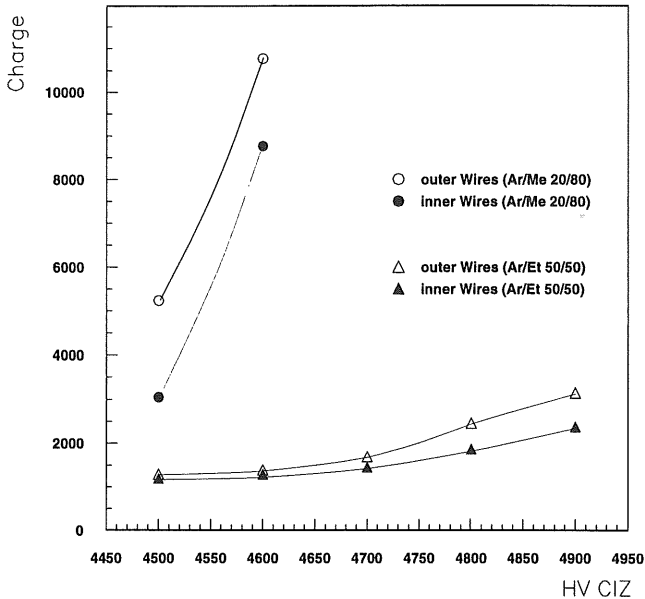


Figure 5.4: Mean charge of CIZ with different gas mixtures as a function of high voltage. (Me = Methane (CH<sub>4</sub>); Et = Ethane (C<sub>2</sub>H<sub>6</sub>))

In principle we could have enhanced the high voltage up to 5100 Volt to get a satisfactory efficiency with the gas mixture of Ar/C<sub>2</sub>H<sub>6</sub> (50/50%) but the chamber was never tested in such a high region of the cathode voltage. The danger of a serious hardware damage lead us to change the ratio of the components of the gas mixture.

In Figure 5.5 the mean collected charge is shown for Argon and Ethane in different mixtures. An increase of the gas gain is evident if the ratio of Ethane to Argon becomes smaller. This higher gas gain with a lower Ethane contribution has been observed also in a proportional chamber at the Crystal Barrel experiment at CERN [58].

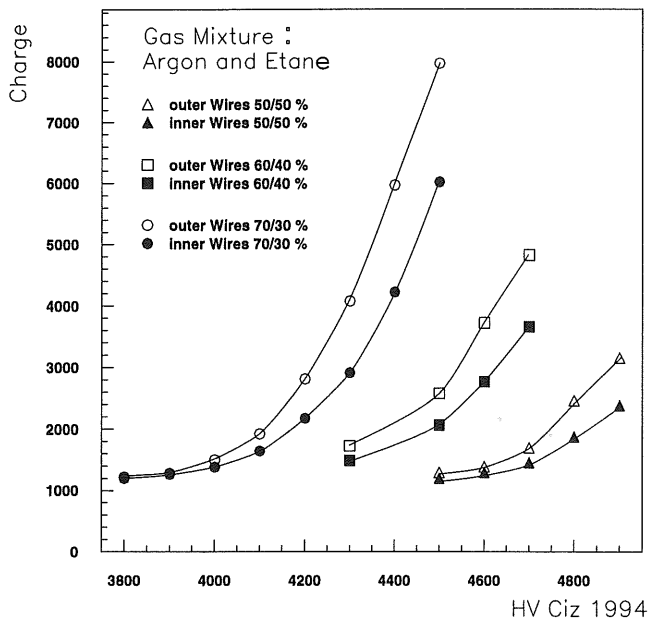


Figure 5.5: Mean charge of CIZ with the gas mixture Argon/Ethane in different ratios as a function of high voltage

During the winter shutdown 1994/1995 the chamber was removed from the tracker part of the detector and opened. There were much less deposits on the sense wires using the Ethane/Argon gas mixture instead of the Methane/Argon one.

### 5.1.3 Experience with another sense wire type

During 1994 the most forward rings in  $z$ -direction (13 and 14) were rewired with gold-plated  $WRe$   $20 \mu m$  sense wires instead of Elgiloy. Due to a smaller resistance of these wires the resistors on both ends of the wires were also lowered in order to get the same charge division performance. During operation the amplitude of the signals were smaller than for the other rings and the efficiency dropped drastically in these two rings. Unfortunately the thresholds of the scanner (see [1] and [55]) could not be lowered independently for the different rings. The

high voltage of these two rings were raised by 200 volts above the nominal value of 4500 in order to get the same efficiency. The ageing effects of *WRe* wires were comparable to Elgiloy but a faster rise time is seen for *WRe*.

### 5.1.4 High voltage problems

During the 1994 run in three out of 15 rings the desired high voltage could no longer be reached already after a short running period, which excluded radiation damage as a possible cause. The problem arose only in conjunction with high electron currents mainly at the beginning of a new filling period of the HERA ring. The hardware protection system switched the high voltage off. No problems were observed during comics data taking. When the chamber was opened during the 1994/95 shutdown again large deposits were observed in these cells on the potential wires, while the neighboring cells were clean. The deposits arose from oil residues on the gold wires left from the production process, which could not properly be removed with the wires soldered into the chamber, and were produced during the initial burning-in phase of the chamber. A special tool was fabricated, which allowed to clean gold wires during transfer from one spool to another in an ultrasound bath before putting them into the chamber. This was evidently the reason for the problems with the high voltage as CIZ was full operational and efficient during 1995. These high voltage problems occurred also during the run in 1993 where two rings could not be operated on the nominal value.

## 5.2 The software

### 5.2.1 *Qt* analysis and noise studies

The relevant parameters of a drift chamber wire signal are the arrival time ( $t$ ) and the pulse integral ( $Q$ ) i. e. the collected charge. They allow the calculation of the distance of a crossing particle from the sense wire (using the drift time) and the position along the sense wire (using the pulse integral from both ends of the wire, referred to as "charge division"). The energy loss  $dE/dx$  is measured by summing the charge of all pulses on the wires. The determination of these signal parameters is done in a program which runs on the front-end processor. The input data are digitized signals with suppressed digitisations of the baseline (zero suppression, as provided by the scanner hardware [1] and [55].)

A considerable amount of work has been concerned with noise studies. Since nearly all readout devices in H1 are clocked by the HERA bunch repetition frequency of 10 MHz, this particular frequency appears at different levels also in all analog chains and appears also superimposed on some of the pulses registered by the analog chain of the CIZ. This can be seen in [61] as a pattern of peaks in the drift time distribution which reflects a clear 10 MHz structure. If they are sitting on top of a real hit "fake" hits which are generated by the noise can emerge a real hit produced by a charged particle. In such a situation the two hits are "clipped" by the *Qt* program and seen as two individual signals. Most of the hits are coming from real particles crossing the chamber but the superposition of a 10 MHz signal shifts all hits systematically and hence modifies the original drift time distribution. An analysis of the output data of the *Qt*

program indicated that the noise is less prominent in the backward part of the chamber in  $z$ . If there are two hits on the same wire the first hit is less affected by noise than the second one, often identified as an additional hit produced by noise. Investigation on the parameters of the  $Qt$  program removed partly the most prominent spikes in the drift time distribution.

### 5.2.2 Isochrone map

The influence of the magnetic field of 1.2 Tesla with direction parallel to the beam axis on the drift field direction has been studied in detail in [55] (Chapter 4.3.3). The most important effect is a modified isochrone map installed during 1994 which takes into account these effects. Calibrating the  $t_0^{offset}$  (see section 5.3.2) separately for the inner and the outer wires lead to a difference in values. Adjusting  $t_0^{offset}$  to its correct value the triple hit resolution (as the deviation of one hit from the line which connects two other hits) became worse. This effect was revealed as an artifact of the isochrone map used and a third map was created which improved the situation but still did not make it perfect (see Figure 5.13). For very small and very large theta of tracks the actual parametrization of the isochrones as circles is not well suited for the reconstruction of the hits. Looking for the deviation of the hits measured by the CIZ from a track in the CJC as a function of theta (Figure 5.6) a spreading of the hits for flat tracks is visible. Taking a parametrization with polynoms instead of circles would improve the situation, but has not been implemented yet.

### 5.2.3 Reconstruction of tracks

Since the beginning of data-taking in 1992 different solutions were tried to relate the hits in the tracker chambers to particle tracks ("pattern recognition"). The linking procedure between the  $z$ -chambers and the central jet chambers is inherently difficult for the following reasons: The CJC has a resolution for one hit of about  $200 \mu m$  in the  $r\phi$ - plane and a resolution of about 3 cm in the  $z$  direction which is measured using "charge division". The  $z$ -chambers have an excellent resolution in  $z$  of a few  $100 \mu m$ , but a low resolution in  $r\phi$ . A track as such can only be defined by the jet chamber. Experience of the analysis of the data have shown, that usually as many as 10 hits within the CJC and also a minimal length of a track are required for so called "good" tracks which are accepted for physics analysis.

Due to the large range of allowed crossing angles in the detector ( $16^\circ - 169^\circ$ ) there is no simple relationship between drift time and the position in the chamber. The position  $(z, r)$  is a function of drift time ( $t_D$ ), wire number ( $n_w$ ) and crossing angle ( $\vartheta$ ), which is unknown initially.

The procedure depends crucially on the knowledge of the isochrones in the chamber which were parametrized as circular arcs in the form

$$(z - a)^2 + (x - b)^2 = \rho^2 \quad (5.1)$$

$z$  and  $x$  are the coordinates in the chamber and  $a$ ,  $b$  and  $r$  are functions of the drift time and wire number. For a given drift time the isochrone parameters are then computed via interpolation in the table, where the values of  $z$  and  $r$  are constrained to be maximal and minimal values. Using

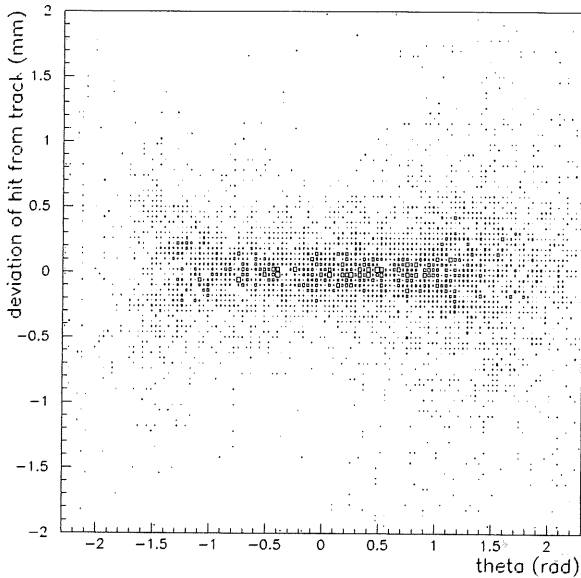


Figure 5.6: Deviation of CIZ hits from a CJC track as a function of  $\vartheta$  of the track. This Figure is produced with the third isochrone table used during 1995.

the center of the isochrone section an initial guess for the position  $(z, r)$  is simply given by

$$z_{guess} = a(t) + \rho(t) \quad (5.2)$$

$$r_{guess} = r_0 + x_{guess} = r_0 + b(t) \quad (5.3)$$

where  $r_0$  is the nominal radius of the chamber. Two procedures are then applied to correlate hits with one another to reconstruct segment in a single drift cell or to link the hits to track segments from other detector parts.

In the beginning single track segments in both  $z$ -chambers, CIZ and COZ were reconstructed and linked to corresponding tracks in the jet chambers. Details on the reconstruction of those segments within CIZ can be found in [55] and [59].

In a further step the program was modified such that only single hits are collected within the  $z$ -chambers rather than full segments. If a vertex has been found by the jet chamber reconstruction program, and if it is assumed that all tracks originate from this vertex the appropriate coordinates for hits in the CIZ can be calculated, and the corresponding hits found can be collected in a linking module [59] [60].

Given the vertex coordinate  $(z_v, r_v = 0)$ , and the isochrone parameters for the hit  $(a_i, b_i, r_i, z_i^0, x_i^0)$ ,

the slope  $\alpha$  can be estimated as

$$\alpha = \frac{z_i^0 - z_v}{x_i^0 + r_0} \quad (5.4)$$

Using  $\alpha$ , a better point can be obtained as

$$z_i^1 = a_i + \frac{\rho_i}{\sqrt{1 + \alpha^2}} \quad (5.5)$$

$$r_i^1 = b_i + \frac{\rho_i \alpha}{\sqrt{1 + \alpha^2}} \quad (5.6)$$

Both the left and the right solution for every valid hit in the CIZ are computed. The reconstruction program then uses the CJC track information to project into the CIZ and identify hits which could be associated with the track. If an association is made, with the track information from the CJC an improved  $z$  and  $r$  for the hits can be provided. The more precise  $\phi$  value from the CJC also allow to better determine radial coordinate, which varies because wires are strung along a polygon and not along a circle.

In a third step the priority changed which was given to the vertex fit. To do this first the hits from the  $z$ -chambers are combined and associated with the tracks. The initial vertex fit using only the information from CJC improves the quality of the central tracks and makes it easier to link the tracks to the other detectors. The linking routine uses an algorithm similar to the "simulated annealing" procedure (developed in neuronal networks programs) link the  $z$ -chamber hits to tracks from the jet chamber. The new program allows a link to the CIZ even if only one single hit was found to match a CJC track. ( See further chapters for detailed numbers on linking efficiencies).

## 5.3 Calibration

The final determination of the space point in  $r$ ,  $z$ , and  $\phi$  also depends on a number of calibration constants and parameters. These include geometrical constants like the accurate wire position. Electrostatic and gravitational forces will move the wires away from their original position. A mechanical deformation of the detector will change the wire position also. Secondly, there are parameters which depend on the running condition of the drift chamber, as the drift velocity which is a function of the applied electric field and the gas mixture as well as the magnetic field. Finally the readout and signal electronics influence the measurement of the time and the charge. All these influences could be corrected in a calibration procedure which has to adjust the calibration constants needed in the reconstruction program.

### 5.3.1 $\phi$ calibration

The determination of the  $\phi$  coordinate along a wire of CIZ is done using the method of charge division. This method is an application of the Ohm's law and relates the fraction of the charges on both ends of the wire  $Q_{\pm}$  to the ratio of the resistors to both ends  $R_{\pm}$  :

$$\frac{Q_+}{Q_-} = \frac{R_-}{R_+} = \frac{\frac{L}{2} + (\phi - \phi_0)}{\frac{L}{2} - (\phi - \phi_0)} \quad (5.7)$$

This can be written as :

$$\phi = \phi_0 + \frac{L}{2} \cdot \frac{Q_- - Q_+}{Q_- + Q_+} \quad (5.8)$$

The contribution of the input resistance of the amplifiers and the capacities of course does not depend on the actual position of a particle in  $\phi$ . The ratio  $\frac{Q_-}{Q_+}$  is reduced due to this effect, which make the wire seemingly longer. This effect can be corrected for by a factor  $L_{eff}$  in formula 5.8. The integrals of collected charge after the digisation step can be written as a product of effective charge and gain factor of the amplifier:

$$Q_{right} = g_+ \cdot Q_+ \quad (5.9)$$

$$Q_{left} = g_- \cdot Q_- \quad (5.10)$$

The final  $\phi$  coordinate of the hit is then given as:

$$\phi_{Hit} = \phi_0 - L_{eff} \cdot \frac{Q_{left} - g_{rel} \cdot Q_{right}}{Q_{left} - g_{rel} \cdot Q_{right}} \quad (5.11)$$

where  $\phi_0$  is the center of the wire and  $g_{rel} = \frac{g_-}{g_+}$  the relative gain factor which corrects for differences in the amplifier gain. There are 3 calibration constants which need to be tuned:  $\phi_0$ ,  $L_{eff}$  and  $g_{rel}$ .

In principle the three parameters can be tuned using cosmic tracks with requirement that the difference of the two peaks in the pulse spectrum correspond to  $180^\circ$  for vertical tracks. A more precise and accurate determination of the calibration constants can be done with respect to an external detector like the CJC. Vice versa the CJC uses the accurate  $z$  information from the  $z$ -chambers to tune their  $z$  resolution.

A special program was developed which minimizes a  $\chi^2$  function according to:

$$\chi^2 = \sum \frac{(\phi_{CJC} - \phi_{CIZ})^2}{\sigma^2} \quad (5.12)$$

where  $\phi_{CJC}$  is the reference value of  $\phi$  measured in the jet chamber and  $\phi_{CIZ}$  is the same as  $\phi_{Hit}$  in formula 5.11.  $\phi_{CIZ} = \phi_{CIZ}(\phi_0, L_{eff}, g_{rel}, Q_{left}, Q_{right})$  is a function of the three calibration constants and minimizing  $\chi^2$  is equivalent with tuning the correct parameters. The program is able either to calibrate all wires together or to tune all parameters for all wires separately.

At the beginning of 1994 the line drivers were replaced for the inner wires (number # 2 and # 3 (see Figure 5.3)) in order to equalize the pulse-heights of the outer and the inner wires. A separate calibration for both wire types was needed. (See [55] Figure 9.5 for the resolution).

### 5.3.2 Calibration of drift velocity and time offset

The drift time to calculate the position of a hit in the chamber is given by:

$$t_D = T_M - t_0^{offset} - t_0^w \quad (5.13)$$

where  $t_M$  is the measured time as provided by the  $Qt$  routine,  $t_0^w$  is the wire by wire offset introduced by differences in cable length and propagation times and  $t_0^{offset}$  is the global time



offset determined by the global cable length and delays in the readout system. The drift velocity is contained in the isochrone map, nevertheless a linear correction factor  $c_{scale}$  is used for a precise adjustment. The isochrone map is scaled linearly to correspond to the actual drift velocity. In principle the time offset and the drift velocity can be evaluated simply from the drift time spectrum using the the rising edge of the distribution to calculate the time  $t_0^{offset}$  and the falling edge for the maximum drift time, which corresponds to the maximum drift length. The drift velocity is then calculated by  $v_D = l_{Dmax}/t_{Dmax}$ . There are other and more accurate methods to tune these two parameters. In matching the track segments, which cross the wire plane it is possible to tune  $t_0^{offset}$  and the drift velocity can be determined too by matching the segments from tracks which cross the cathode cell boundaries. However, for CIZ the precision of these two methods is limited by the geometry of the tilted wire arrangement and the small number of wires (see Figure 5.2 the upper plot where the different situations are shown.) In addition inhomogeneities in the drift field near the cell boundaries and near the wires can be a source of wrong measurements. For the CIZ a third method is used with great accuracy to tune both calibration constants  $t_0^{offset}$  and  $v_D$  using cosmic tracks.

### Calibration with cosmic data

This section describes a procedure for calibrating the CIZ using cosmic events. The procedure requires clean cosmic events in which a single cosmic ray penetrates the H1 detector from above, passes through the COZ, CIZ, then near the beam axis, then through the CIZ and finally the COZ. The events must also be reconstructible. The reconstruction must yield two CJC tracks, each of which has a CIZ and a COZ link. Given these criteria, the procedure fits the two tracks as one long straight track in the  $z$ - $s$  plane, ( $z$  coordinate along the beam axis, and the arclength  $s$ ).

Given a helix in space, whose axis of symmetry is parallel to the  $z$  axis, the points on the helix satisfy the equations:

$$x_i(\beta_i) = r_0 \sin \psi_0 + \frac{1}{\kappa} [s \cdot \cos \beta_i + \sin \psi_0] \quad (5.14)$$

$$y_i(\beta_i) = -r_0 \cos \psi_0 + \frac{1}{\kappa} [s \cdot \sin \beta_i - \cos \psi_0] \quad (5.15)$$

$$z_i(\beta_i) = z_0 - \frac{\cot \vartheta}{\kappa} \cdot \left[ \beta_i - \psi_0 - s \cdot \frac{\pi}{2} \right]. \quad (5.16)$$

There  $\kappa^{-1}$  is the radius of curvature, and is signed.  $r_0$  is the distance of closest approach to the  $z$  axis, and is also signed.  $\psi_0$  is the angle between the tangent to the helix in the  $x$ - $y$  plane at  $r_0$ .  $z_0$  is the  $z$  coordinate of the track at  $r_0$ , while  $\vartheta$  is the polar angle of the helix. The parameter  $s$  is either  $+1$  or  $-1$ , and depends on the charge of the track, and the direction of the magnetic field. For  $\vec{B}$  along the  $+z$  axis,  $s$  is positive for a negative track. The sign of  $\kappa$  is chosen to be the sign of  $s$ , while the sign of  $r_0$  is taken from the direction of  $\vec{r}_0 \times \vec{p}_T$ ; positive if this is in the  $+z$  direction, and negative otherwise. Finally,  $\beta_i$  is the running parameter that describes the angle in the  $x$ - $y$  plane relative to the center of the helix, that describes the point  $(x, y)$ . In the  $x$ - $y$  projection, the helix appears as a circle of radius  $\frac{1}{|\kappa|}$ , while in the  $z$ - $S$  projection, it appears

as a straight line, ( $S$  is the length of the arc in the  $x$ - $y$  plane). The arc length can be computed at a point  $(x, y)$  as follows. If  $r = \sqrt{x^2 + y^2}$ , and  $\rho = \frac{1}{|\kappa|}$

$$S = \rho \cdot \arccos\left(\frac{\rho^2 + R^2 - r^2}{2 \cdot \rho \cdot R}\right) \quad (5.17)$$

where  $R = \rho - r_0 \cdot \text{sign}(\kappa)$ . For  $r = r_0$ ,  $S = 0$ . Thus for every point along the track, we can compute the arc length,  $S_i$ . It is also important to estimate the error in  $S$ ,  $\delta_S$ . To do so, we will write equation 5.17 as:

$$\cos(S/\rho) = 1 - \frac{r^2 - r_0^2}{2\rho(\rho - r_0)}.$$

Now, in the typical case of a cosmic track,  $S/\rho < 0.1$ , which means we can approximate the cos function by its Taylor series, or:

$$1 - \frac{S^2}{2 \cdot \rho^2} = 1 - \frac{r^2 - r_0^2}{2\rho(\rho - r_0)}.$$

This then can be reduced to yield:

$$S = \sqrt{\frac{\rho(r^2 - r_0^2)}{\rho - r_0}} \quad (5.18)$$

We can now estimate the error in  $S$  with respect to the various parameters.

$$\begin{aligned} dS/dr &= \sqrt{\frac{\rho \cdot r^2}{(\rho - r_0) \cdot (r^2 - r_0^2)}} \\ dS/dr_0 &= \frac{1}{2} \sqrt{\frac{r - r_0}{\rho \cdot (r^2 - r_0^2)}} \cdot \left[ 1 + \frac{r^2 - \rho^2}{(\rho - r_0)^2} \right] \\ dS/d\rho &= \frac{S}{2 \cdot \rho \cdot (1 - \rho/r_0)} \end{aligned}$$

These can be simplified for typical values to estimate the significance of each contribution.

$$\begin{aligned} dS/dr &\approx 1 \\ dS/dr_0 &\approx 0.1 \text{ to } 0.4 \\ dS/d\rho &\approx 0.001 \end{aligned}$$

The error with respect to  $r_0$  is roughly independent of  $\rho$ , and grows as  $|r_0|$  increases. The error with respect to  $\rho$  is very tiny, even for 100% errors in  $\rho$ .

In the problem at hand, the parameters  $\kappa$  and  $r_0$  are taken from the CJC tracks, and the points of interest are then the attached hits in the CIZ and COZ. Using the  $(z_i, r_i)$  pairs for the attached  $z$ -chamber hits, we use the CJC information to convert these to  $(z_i, S_i)$  pairs. These points should then fall on a line:

$$z = \alpha \cdot S + \beta$$

In order to take advantage of the fact that the two tracks are the same, we can make the  $S_i$  on one of the tracks negative. Thus all the points from both tracks will now satisfy the same linear equation. Given that we have  $n$  points, each of which is measured with an error  $\sigma_i = \delta z_i$ , we can solve for  $\alpha$  and  $\beta$ :

$$\begin{aligned}\Delta &= \sum_i^n \frac{1}{\sigma_i^2} \cdot \sum_i^n \frac{S_i^2}{\sigma_i^2} - \left( \sum_i^n \frac{S_i}{\sigma_i^2} \right)^2 \\ \alpha &= \frac{1}{\Delta} \cdot \left[ \sum_i^n \frac{1}{\sigma_i^2} \cdot \sum_i^n \frac{S_i \cdot z_i}{\sigma_i^2} - \sum_i^n \frac{S_i}{\sigma_i^2} \cdot \sum_i^n \frac{z_i}{\sigma_i^2} \right] \\ \beta &= \frac{1}{\Delta} \cdot \left[ \sum_i^n \frac{S_i^2}{\sigma_i^2} \cdot \sum_i^n \frac{z_i}{\sigma_i^2} - \sum_i^n \frac{S_i}{\sigma_i^2} \cdot \sum_i^n \frac{S_i \cdot z_i}{\sigma_i^2} \right]\end{aligned}$$

Given these equations, we can define several different fits, all of which are useful for the overall calibration. We define here two quantities, the *deviation* and the *resolution*. We use only the COZ points to make the fit, and then compute the *deviation* of each CIZ hit from the fitted line. Further we can compute the *resolution* of a single hit by making the line fit excluding only the desired hit, and then computing the distance from this hit from the line, the *resolution*. In order to facilitate looking at these things, we map all of the CIZ data onto one ring. We can then look at the *deviations* from the track fit as a function of the drift distance. This plot, shown in Figure 5.7 is the heart of the calibration procedure as it is used to tune both calibration constants. In Figure 5.7 (a) we see the *deviation* with correctly tuned calibration constants. A straight flat distribution with matched left and right part of the CIZ drift cell indicates a correct calibration of  $t_0^{offset}$  and drift velocity  $v_d$ . In the next plot we see a shift in  $t_0^{offset}$  of 100 ns with a correct  $v_D$ . This appears as a shift of the *deviations* in the right and the left drift cell but no slope in the distribution. In (c) we see a 10% misadjusted  $v_D$  with a correct  $t_0^{offset}$ . The left side matches the right one but there is a slope in the distribution. Finally both calibration constants  $v_D$  and  $t_0^{offset}$  are wrong in (d) which results in a shift together with a slope.

In principle we are now able to tune the parameters checking the plots and varying the input parameters until the distribution is flat and match the left and the right side of the drift time distribution.

To be able to run the calibration automatically a special program fits each side of the drift cell independently with a straight line ( $A + B \cdot D$  where  $D$  is the drift distance) and calculates from the shift of the two lines ( $A$ ) the offset in  $t_0^{offset}$  and the correct drift velocity from the slope of the two lines ( $B$ ). These numbers are converted into the units used in the database and can be used directly as new input parameters for the program. Thus, this procedure can work iteratively and converges after two or three iterations. The two most inner bins near the wires are excluded from the fit due to a non homogeneous drift field.

This procedure is able to measure 1 ns deviation in time and 1 permille shifts in  $v_D$ . The statistical error in the drift velocity measurement is 3 permille. The stability of the variables  $A$  and  $B$  from the straight line can be deduced from Figure 5.8. If 10000 hits are collected the fit begins to converge and the results remain stable.

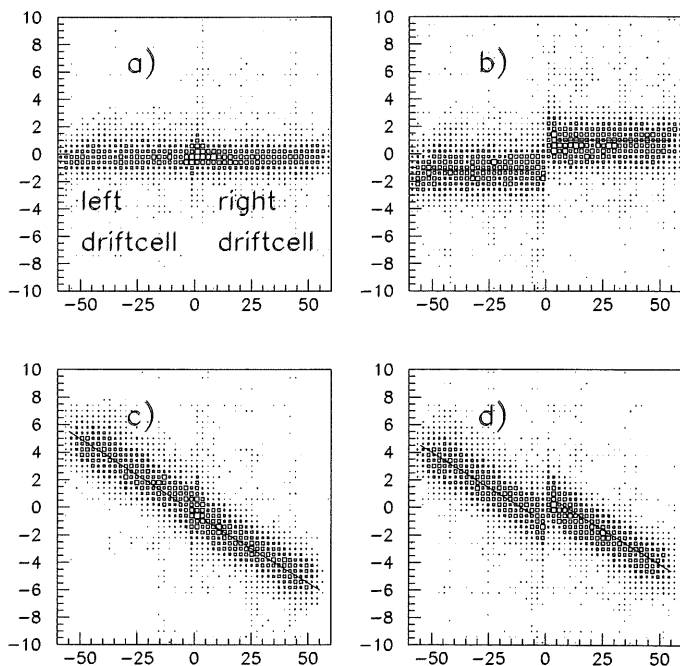


Figure 5.7: *Deviations of CIZ points from the track fit which uses only the COZ as a function of the drift distance. The left and the right drift cell range from -60 to 0 mm and from 0 to 60 mm respectively.*

- a) correctly tuned CIZ calibration constants.
- b)  $t_0^{offset}$  is shifted by 100 ns.
- c)  $v_D$  is shifted by 10%.
- d) both shifts included.

It is important to note that a miscalibration of the COZ either in the time or in the drift velocity does not affect our measurement as we measure the mean of the distribution and not the width. Not correctly tuned calibration constants of the COZ cause a broadening of the *deviation* plot of the CIZ but no shift. The CIZ calibration constants remain stable within the statistical errors. This is demonstrated in Figure 5.9 where the upper plots correspond to correctly tuned COZ parameters and the lower one do not. We see a projection from the left (left side) and the right driftcell (right side) of CIZ. A clear broadening of the distribution is the result. With this

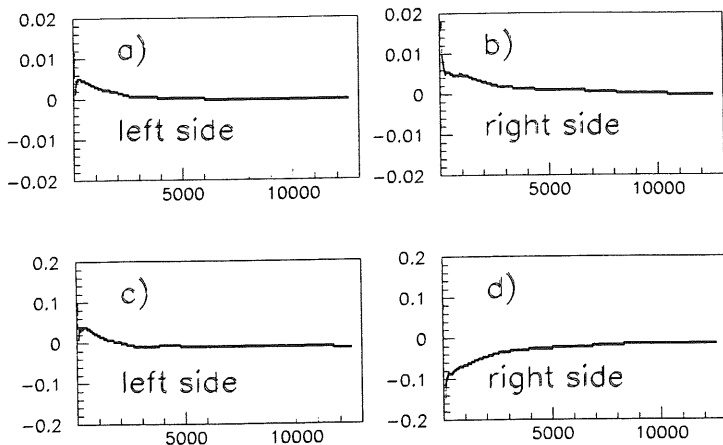


Figure 5.8: Fit-parameters  $A$  and  $B$  from the straight line fit through the *Deviation* of the left and right drift cell in dependence of the number of hits.

a) and b) fit-parameter  $A$ ,  
 c) and d) fit-parameter  $B$ .

method it is also possible to note absolute shifts between the two chambers. In Figure 5.10 COZ is shifted by 3.8 mm relative to the COZ in positive  $z$  direction. We observe that the *deviation* distribution of the CIZ is splitted in an upper and a lower band. The upper band consists of hits within rings tilted in forward direction and the lower one collects hits in rings 0–8. Hence a slight shift of the  $z$ -chambers relative to each other results in a vertical shift of the *deviation*. This method was used to fix both chambers in their relative position in the  $z$  direction. As a cross check the *deviation* of the COZ hits from the line fixed only with the CIZ can be used to test the procedure. For geometrical reasons this method is not so sufficiently to calibrate the COZ, but wrong CIZ parameters immediately broaden the COZ *deviation* according to Figure 5.11. In (a) a clear structure is visible which proves that the CIZ parameters are correct. A slope in the distribution indicates some problems in the drift velocity calibration of the COZ. In (b)  $t_0^{offset}$  of COZ is shifted by 100 ns. In (c)  $v_D$  is shifted by 10 % and (d) includes both shifts together. Using the whole drift region where the drift field is homogeneous is the main advantage of this calibration method compared to the other method mentioned above. The basic idea was to use the COZ to calibrate the CIZ and then to use the CIZ to calibrate the COZ as an iterative procedure. The COZ is calibrated independently, so we use the COZ to calibrate the CIZ.

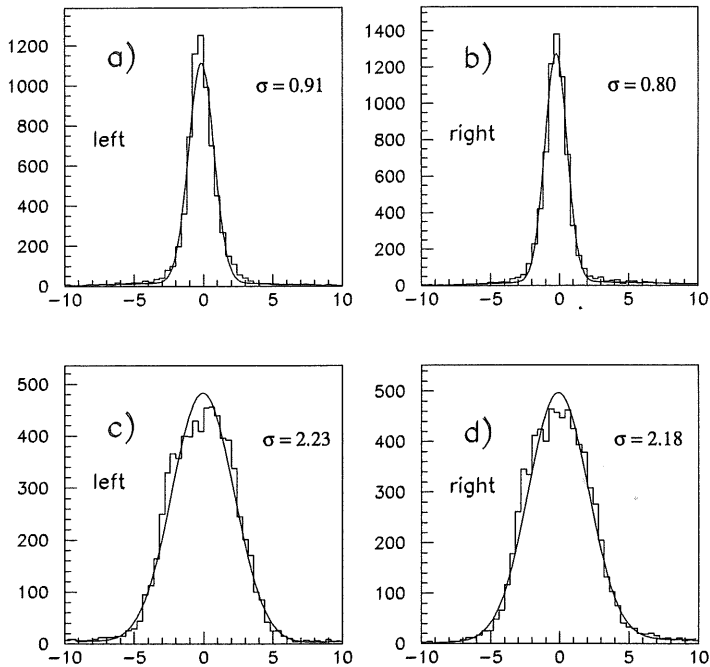


Figure 5.9: Projection of the *deviation* of CIZ as in Figure 5.7

a) and b): correct tuned COZ calibration constants. The left and right drift cell of CIZ is shown.  
 c) and d): the same as in a) and b) but with wrong calibration constants of COZ.

### Calibration with *ep* data

Not only cosmic muons are helpful to calibrate the  $t_0^{offset}$  and the drift velocity. In principle it is possible to use normal data from *ep* collisions and follow the same procedure as for cosmic data. This has been tested in a program which selected good CJC tracks with linked to both *z*-chambers and pointed to the primary vertex. These tracks are fixed by the COZ and the vertex. In Figure 5.12 the *deviation* of linked CIZ hits from such a track is shown. The distributions are the same as in Figure 5.7 but for *ep* data. The left column shows the scatter plot and the right side represents the corresponding mean values of the histogram with a different vertical scale. The deviation of the CIZ hits which are linked to that track yield the same *deviation* as just discussed for cosmic tracks. There is a crucial difference between these two methods. The

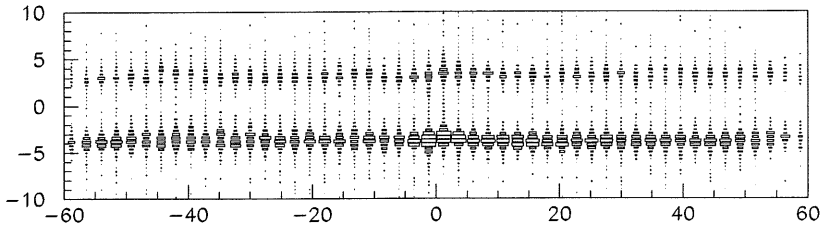


Figure 5.10: CIZ *deviation* with CIZ shifted by 3.8 mm in positive  $z$  direction.

cosmic track is very long and fixed with both ends in the outer  $z$ -chamber. The  $ep$  data track has half the length of the cosmic track and the accuracy of the vertex is not so good. Hence the precision of the measurement of the calibration constants using cosmic data is much better than for  $ep$  data.

This method is only usable if the tracks are constrained to a vertex and if the measurement of the CIZ has no influence on the assignment of tracks to the vertex.

## 5.4 Resolution, efficiency and performance

### Resolution

The H1 detectors have been designed to provide a good momentum resolution in combining the information from the different sub-detectors. The resolution of the inner  $z$ -chamber was measured with data and Monte Carlo data.

A combined resolution of the CIZ can be measured with cosmic tracks using the same procedure as for calibration i. e. the *deviations* of the CIZ hits from the track fit using only COZ. Another quantity is the *resolution* of CIZ by making the line fit excluding only the desired hit, and then computing the distance of this hit from the line. As mentioned earlier in this chapter the problem of the isochrone map affects the width of the *deviation* and *resolution*. This is an artifact of the isochrone table used and has nothing to do with cable length or delays in the readout system. The  $t_0^{offset}$  parameter seems to be different for the different wire types as can be seen in Figure 5.13 in the scatter plots (a) and b)) which illustrates the *deviation* as a function of the drift region shown for the outer and inner wire types separately. Below a projection through the left and the right drift cell is shown for both the outer wires (middle) and the inner ones (below).

Figure 5.14 summarizes the external resolution measurements. Only the inner wires are used. All fits are made as a Gaussian on top of a quadratic polynomial. The *deviation* is shown in the two upper plots 5.14 (a) and (b). Figures 5.14 (c) and (d) represent the *resolution* of the inner wires (i. e. line-fit excluding the desired hit and then computing the distance from this hit to

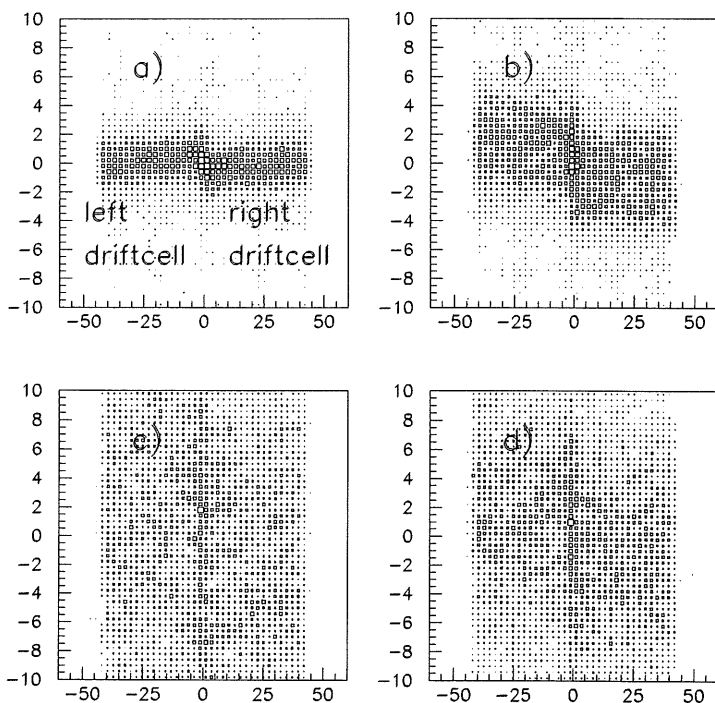


Figure 5.11: *Deviations* of COZ from the track fit which uses only the CIZ as a function of the drift distance. The left and the right driftcell ranging from -50 to 0 mm and from 0 to 50 mm respectively.

a) correctly tuned CIZ calibration constants. b)  $t_0^{offset}$  is shifted by 100 ns. c)  $v_D$  is shifted by 10%. d) both shifts included.

the line). The lower scatter plot in Figure 5.14 (e) illustrates the *resolution* as a function of the full drift region from -60 mm to +60 mm. The difference between the width of the *deviation* and the *resolution* is small indicating quite good calibration.

The overall resolution number of about  $700 \mu\text{m}$  also contains effects like multiple scattering between the different chambers and miscalibration of the latter.

An internal resolution can be obtained by looking at the deviation of the hits from a track segment which has been reconstructed only with hits collected in the inner  $z$ -chamber. Another possibility is the triple hit resolution which combines two hits to a line and measures the deviation of the hit lying in between. Both distributions are shown in Figure 5.15. These distributions



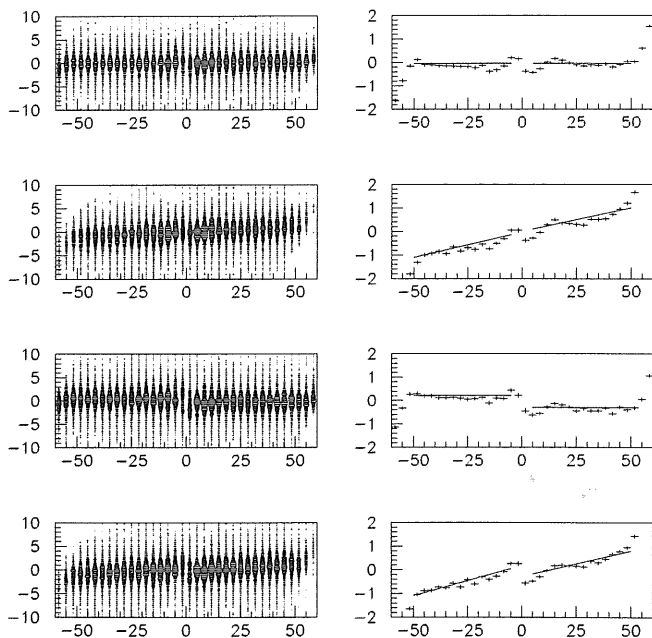


Figure 5.12: *Deviations* of CIZ hits from  $ep$  data tracks which are linked to both  $z$  - chambers and to the primary vertex. The distributions are the same as shown in Figure 5.7 for cosmic tracks. There is a change of the calibration constants of CIZ from the top to the bottom : correctly calibrated (top), drift velocity off by 10%,  $t_0^{offset}$  shifted by 100 ns, both calibration constants shifted (bottom).

Left side: scatter plot of *deviation* vs. drift cell

Right side: mean values of the histograms on the left.

are produced with tracks restricted to  $45^\circ \leq \psi_{135^\circ}$  as measured perpendicular to the  $z$ -axis. Table 5.2 summarizes the results.

The improvement in the momentum determination if the information of the  $z$ -chambers is used are studied with Monte Carlo data. A simulated track was matched together with its reconstructed one and the difference in the momentum is computed (Figure 5.16). Table 5.2 is a

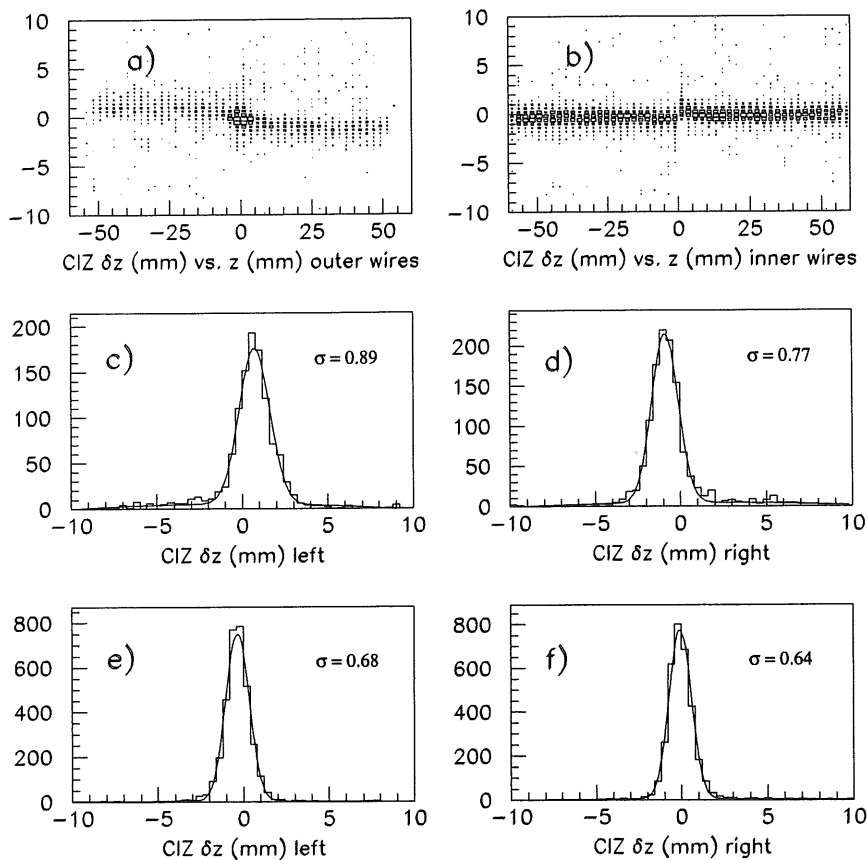


Figure 5.13: Deviation of CIZ hits as measured using the COZ for the inner and outer wire types. The upper column is the deviation as a function of the drift region shown for the outer and inner wire types separately. Below a projection through the left and the right drift cell is shown for both the outer wires (c and d) and the inner ones (e and f).

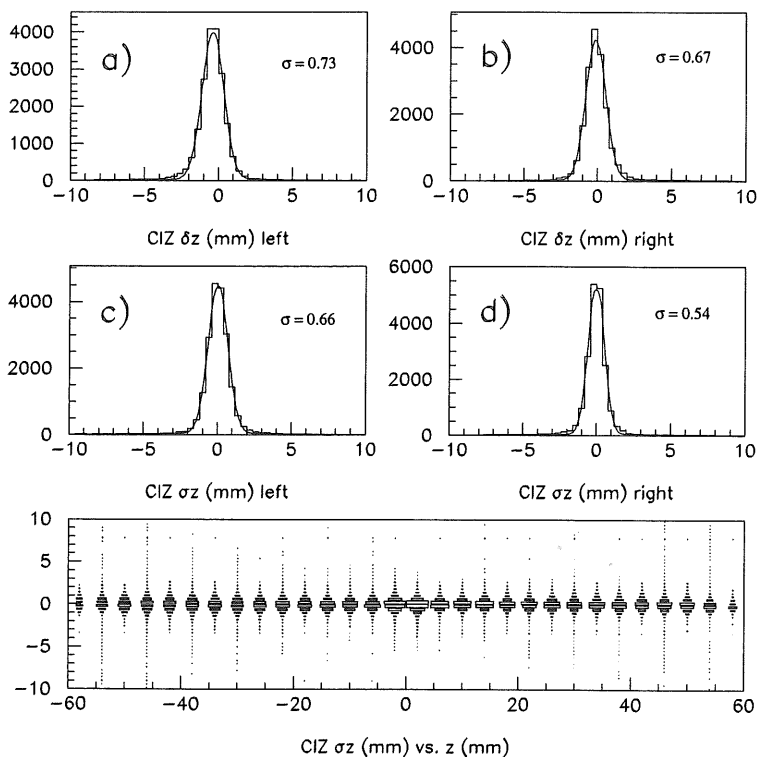


Figure 5.14: *Deviation and resolution of CIZ using cosmic tracks.*

a) and b): *deviation of the inner wires*

c) and d): *resolution of the inner wires by making the line fit excluding only the desired hit, and then computing the distance from this hit from the line.*

e): *the resolution of all wires as a function of the drift field.*

compilation of different values concerning the resolution in space and of different momentum components.

The theoretical calculation of the momentum resolution has been discussed in [55] in detail. The relative momentum  $\Delta p/p$  in GeV as a function of the angle  $\vartheta$  of the tracks is shown in Figure 5.17 using the difference between simulated and reconstructed track parameters for the total momentum difference  $\Delta p$ . The different values for tracks measured only with the jet chambers are compared to tracks which use both  $z$ -chambers CIZ and COZ to determine the

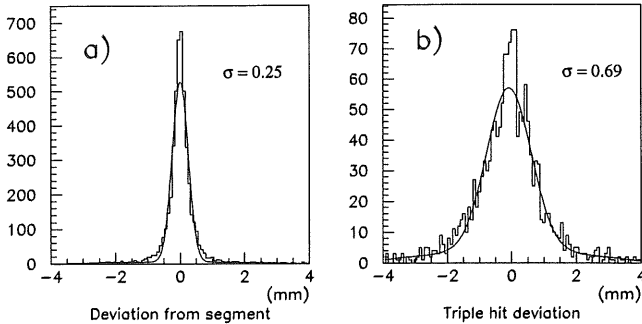


Figure 5.15: Internal resolutions of CIZ.

a) The deviation of hits in CIZ from a segment reconstructed using only hits of CIZ.

b) Triple hit resolution of CIZ.

The tracks are restricted to  $45^\circ \leq \vartheta \leq 135^\circ$  as measured perpendicular to the  $z$ -axis.

momentum. The more precise measurement of the  $z$ -coordinate using the  $z$ -chambers results in smaller tails of the relative momentum resolution for tracks crossing the detector with flat angles. This behavior is in agreement with expectation.

### Efficiency

Three different types of efficiencies were studied :

- Single wire efficiency
- Tracking efficiency
- Linking efficiency

Sigma of distribution	unit	value
<i>deviation</i> (external)	mm	0.70
<i>resolution</i> (external)	mm	0.60
deviation from segment (internal)	mm	0.25
triple hit resolution (internal)	mm	0.55
momentum resolution with $P_z$ only measured with the CJC	MeV	14.5
momentum resolution with $P_z$ measured with both $z$ -chambers	MeV	6.5
total momentum resolution only measured with the CJC	MeV	12.
total momentum resolution with $z$ -chambers included	MeV	9.8

Table 5.2: CIZ resolutions

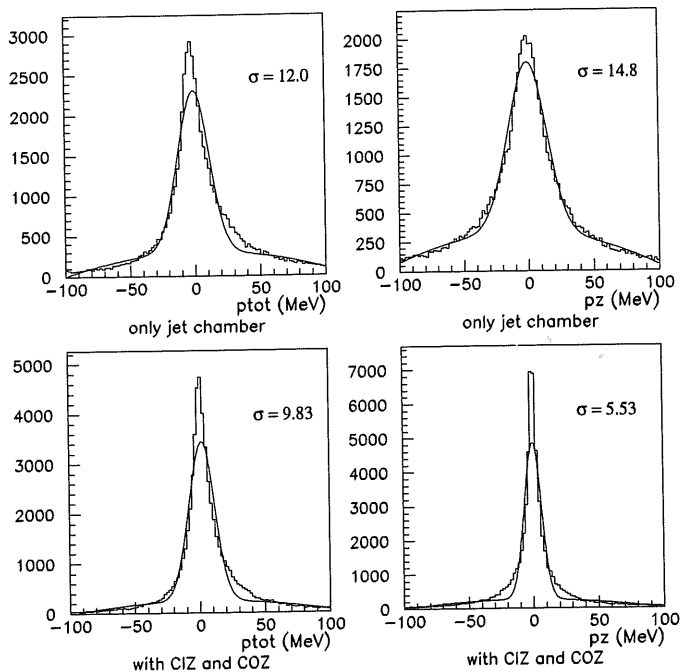


Figure 5.16: difference between a simulated track and the same reconstructed track for the total momentum and for the momentum in the  $z$ -direction.

Upper plots : momentum resolutions of tracks measured only with the jet chambers  
 Lower plots : momentum resolutions of tracks which use both  $z$ -chambers.

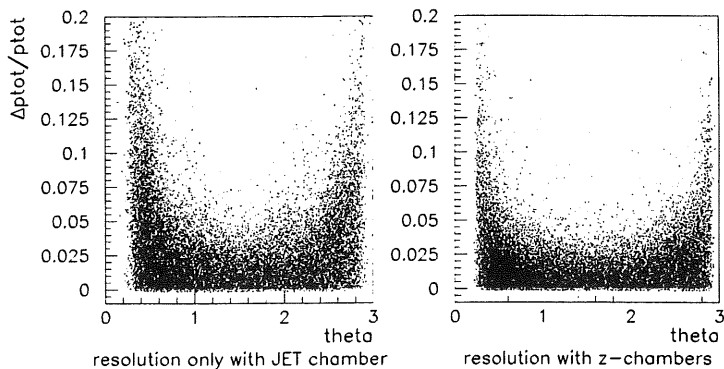


Figure 5.17: Relative momentum resolution  $\Delta p/p$  in GeV using simulated and reconstructed tracks.

The **single wire efficiency** is calculated using a method independent of other detector components. Two hits are required on different wires within the same drift cell: one on an outer wire and the other one an inner wire in such a way that there has to be a single wire between these two hits. Two combinations are possible for CIZ: the wire numbers # 1 and # 3 and the numbers # 2 and # 4 dependent of the side of the drift cell where the track is crossing the chamber. The occurrence respectively of the middle hit within the expected drift time window is the criterion used for determine the single wire efficiency of the inner wires # 2 and # 3.

The **track efficiency** is measured using tracks in the jet chambers pointing to CIZ. The impact point in CIZ has to be within a window in the  $z$ -coordinate in order to take into account the finite resolution of the measurement of the  $z$ -coordinate using only the CJC with the charge division method. No other track should point to the same ring of CIZ. The chamber is regarded as efficient when there are at least two hits on two different wires found. Four combinations of two or three hits are possible for one drift cell.

The **link efficiency** is defined as the number of CJC tracks which have at least two hits found in CIZ. These linked hits fulfilled all criteria of the linking program and are used to improve the measurement of the  $z$ -coordinate.

Figure 5.18 summarizes the dependence of all three efficiencies as a function of the high voltage. This has been done with cosmic data and the actual gas mixture of  $\text{Ar}/\text{C}_2\text{H}_6$  (70/30%).

If  $p$  denotes the single wire efficiency for all four wires the linking efficiency can be calculated

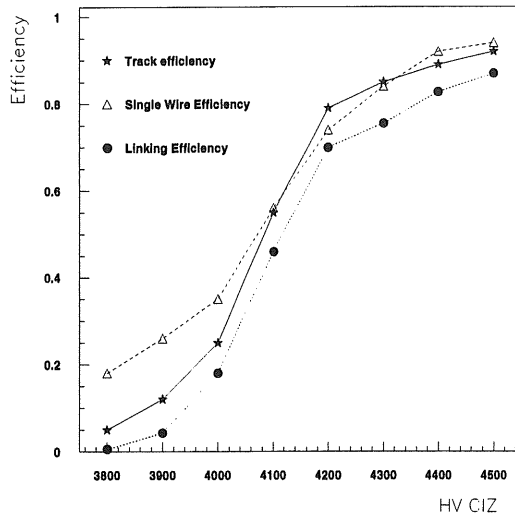


Figure 5.18: Three different efficiencies as a function of the high voltage measured with the gas mixture of Ar/C<sub>2</sub>H<sub>6</sub> (70/30%).

according the following equation:

$$effi = p^3 + 3p^2(1 - p) \quad (5.19)$$

This is valid if combinations of two and/or three hits within CIZ define a link to the jet chambers.

In 1995 the gas mixture and the high voltage remained stable and unchanged. The values of the single wire efficiency were written periodically to a database and are displayed in Figure 5.19. The efficiency of both combinations (efficiency of wire 1 (upper plot) and wire 2 (lower plot)) are shown. A slight decrease towards the end of the year in both distributions indicate ageing effects.

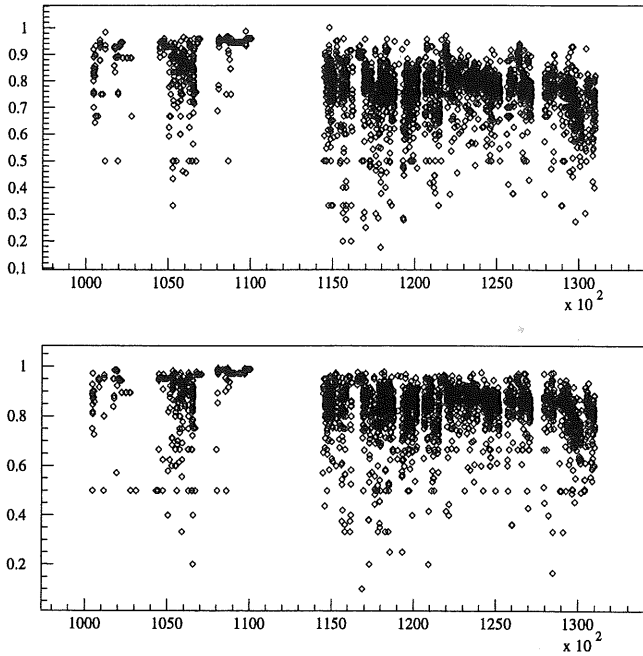


Figure 5.19: Single wire efficiency of CIZ during the run period of 1995. The upper Figure represents the efficiency of wire 1 and the lower one measures the same for wire 2.



## Chapter 6

# Bose Einstein correlation analysis

### 6.1 Event selection

The present study is based on a sample of positron proton collider events collected with the H1 detector in 1994. The data sample comprises an integrated luminosity of  $1.26 \text{ pb}^{-1}$ . Preliminary results of this analysis were presented previously in reference [16]. After full reconstruction of the raw data and after a first rejection of unphysical background the data is divided into event classes according to different physical quantities. These criteria are chosen so loose that nearly all events belonging to that specific class can be included but further cuts are needed to get a clean sample.

Three different types of data sets are used : Low  $Q^2$  and high  $Q^2$  deep inelastic scattering events (DIS events) and diffractive events (rapidity gap see section 3). The scattered positron has to be detected within the backward electromagnetic calorimeter for low  $Q^2$  events (corresponding to a range in  $Q^2$  from  $10 \text{ GeV}^2$  to  $80 \text{ GeV}^2$ ) and in the liquid argon calorimeter for high  $Q^2$  events with  $Q^2 \geq 20 \text{ GeV}^2$ . In the high  $Q^2$  data, the positron track is identified with a track-cluster linking algorithm. The main analysis is based on variables from tracks, so calorimeter information is used only for event selection and determination of kinematic variables.

#### 6.1.1 Deep inelastic scattering events

We use the standard event selection of the H1 deep inelastic analysis group. Low  $Q^2$  events are selected via the detection of the scattered positron with  $E_e \geq 12 \text{ GeV}$  and  $157^\circ \leq \vartheta_e \leq 173^\circ$ , where the polar angle  $\vartheta$  is measured with respect to the proton beam direction. This energy requirement ensures the remaining photoproduction background to be less than 1%. To exclude events with with large QED radiative effects and to ensure substantial hadronic energy flow in the detector the invariant mass squared  $W^2$  of the hadronic system, determined from energy clusters in the calorimeter, is required to be larger than  $4400 \text{ GeV}^2$ . Diffractive events ("rapidity gap events") are removed in the final event sample. To that end events for which the energy deposited within the polar angular range  $4.4^\circ \leq \vartheta \leq 15^\circ$  is less than  $0.5 \text{ GeV}$ , are excluded. The same selections are applied to the various Monte Carlo generated event samples used in the analysis. An event vertex, reconstructed from tracks in the central tracker, and located within

$\pm 30$  cm of the mean vertex  $z$ -position, is required to reject beam-induced background and to permit a reliable determination of the kinematic variables.

In Figure 6.1 a typical example of a low  $Q^2$  event with the positron in the BEMC is shown and Figure 6.2 illustrates a high  $Q^2$  collision where the positron produces a shower in the electromagnetic calorimeter. At least two selected tracks are finally required in an event in order to get at least one charged track pair in each event. 48'000 events passed these cuts from the low  $Q^2$  sample and 16'100 in the high  $Q^2$  sample.

## 6.2 Track selection

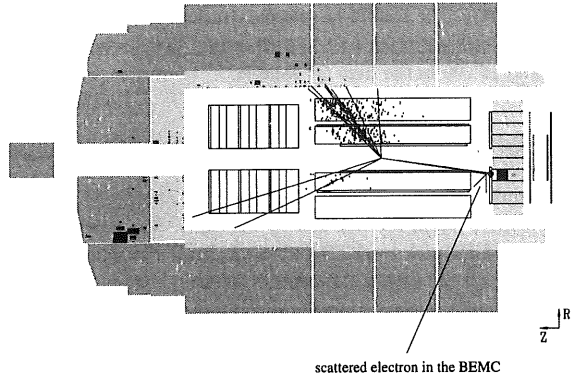
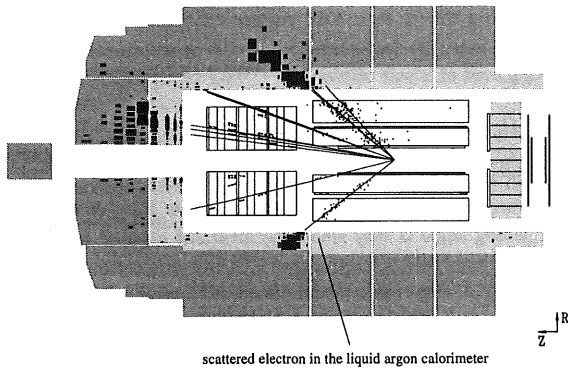
Charged tracks are required to arise from the primary vertex in order to minimize decay products from long lived resonances which are not able to interfere. A minimum of 10 hits within the jet chambers are required for each track. Requiring a transverse momentum  $p_T > 0.15$  GeV/c rejects strongly curving tracks within the central tracking chambers. Positive and negative tracks do not have the same reconstruction efficiency in the low momentum range as a result of the construction of the jet chamber [39]. The ratio of positive to negative track pairs illustrated in Figure 6.3 proves an acceptable relation after the track selection. In addition a non perfect reconstruction efficiency of like charged track pairs very close together in space compared to pairs with the opposite charge can bias the strength of the BEC measurement. Again Figure 6.3 does not show any depletion towards small total momentum nor in the  $p_t$  distribution. In addition, in a visual scan of selected tracks passing all criteria with the event display no spurious tracks ("ghost tracks") due to noise hits or reconstructed mirror hits of real tracks have been found. A polar angle  $\vartheta$  satisfying  $22^\circ < \vartheta < 150^\circ$  restricts the analysis to particles which can be measured at least in the inner jet drift chamber in order to improve the quality of the tracks. The invariant mass squared of a pair of pions is

$$M^2 = (E_1 + E_2)^2 - (\vec{p}_1 + \vec{p}_2)^2 = 2m_\pi^2 + 2E_1 E_2 - 2|\vec{p}_1||\vec{p}_2| \cos \alpha \quad (6.1)$$

where  $\alpha$  is the opening angle between the momentum vectors  $\vec{p}_1$  and  $\vec{p}_2$ .

BEC studies are very sensitive to double counting effects i. e. the splitting of a single track into two pieces. If the opening angle is very small the invariant mass of such a pair contributes to the interesting region where BEC are significant. The invariant mass of like and unlike pairs are shown in Figure 6.4. A huge peak in the distribution of like pairs indicates such splitted tracks, mostly caused between the inner and outer jet chamber. For splitted tracks one finds  $E_1 \cong E_2$ ,  $\vec{p}_1 \cong \vec{p}_2$  and  $M^2 = 4m_\pi^2$ . Taking only those tracks which start within the inner CJC the problem is reduced drastically (see Figure 6.4 (c) ). High voltage problems with a cathode plane in CJC1 required special rejection of double tracks in a particular region. Figure 6.4 (d) illustrates the resulting invariant mass distribution after all cuts on track parameters.

A typical event used to measure BEC is shown in Figure 6.5. Some pairs of charged tracks have such a small invariant mass that they enter into the first ten bins of the mass distribution (this is the case for the pairs with the numbers : (6,8), (6,3), (1,2), (3,10)). In Figure 6.6 a special pair with a mass of 298 MeV is inspected in detail. A good reconstruction quality and pattern

Figure 6.1: A typical low  $Q^{*2}$  event.Figure 6.2: A typical high  $Q^{*2}$  event.

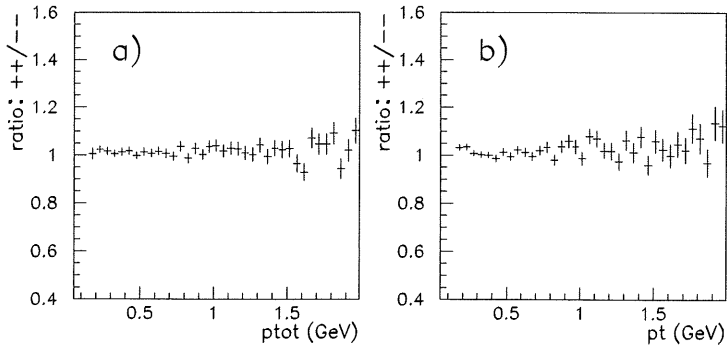


Figure 6.3: Plot (a) shows the ratio of the total momentum of positive and negative tracks and in (b) that for the transverse momentum.

recognition is visible even for tracks very close together. The cut of  $p_t \geq 150$  MeV rejects 20% of all pairs while the cut on the beginning of the tracks within CJC1 affects 9.4% and the final double rejection procedure only 1.7% of all pairs. In Figure 6.7 we demonstrate the effect of the track selection on the angles  $\vartheta$  and  $\phi$  of the tracks. Both distributions remain unchanged, i. e. no bias is visible. Another method to reduce the reconstruction certainly for nearby like charged track pairs is to cut on the opening angle between the two like sign tracks, as done by other experiments [42]. In our analysis we did not apply that cut. The energy loss information available from the CJC is not used in this analysis. All charged particles are assumed to be pions (see Chapter 6.7.2).

### 6.3 Technical aspects of the analysis

In order to measure the correlation Function 2.4 we have to normalize the two-particle like-sign inclusive density denoted with  $\rho_2(M) = \rho_2(M)^{like} = \rho_2(M)^l$  to a reference sample (background)  $\rho^{\text{ref}}(M)$  which contains no Bose-Einstein correlations and form the ratio :

$$R(M) = \frac{\rho_2(M)}{\rho^{\text{ref}}(M)} \quad (6.2)$$

The choice of such a reference sample is not trivial and a source of bias and systematic errors in all BEC measurements. Ideally it should satisfy the following conditions:

- (1) absence of BEC
- (2) presence of correlations due to energy-momentum and charge conservation
- (3) presence of correlations due to the topology and the global properties of the events
- (4) absence of additional dynamical correlations due to resonances or long-lived particle decays.

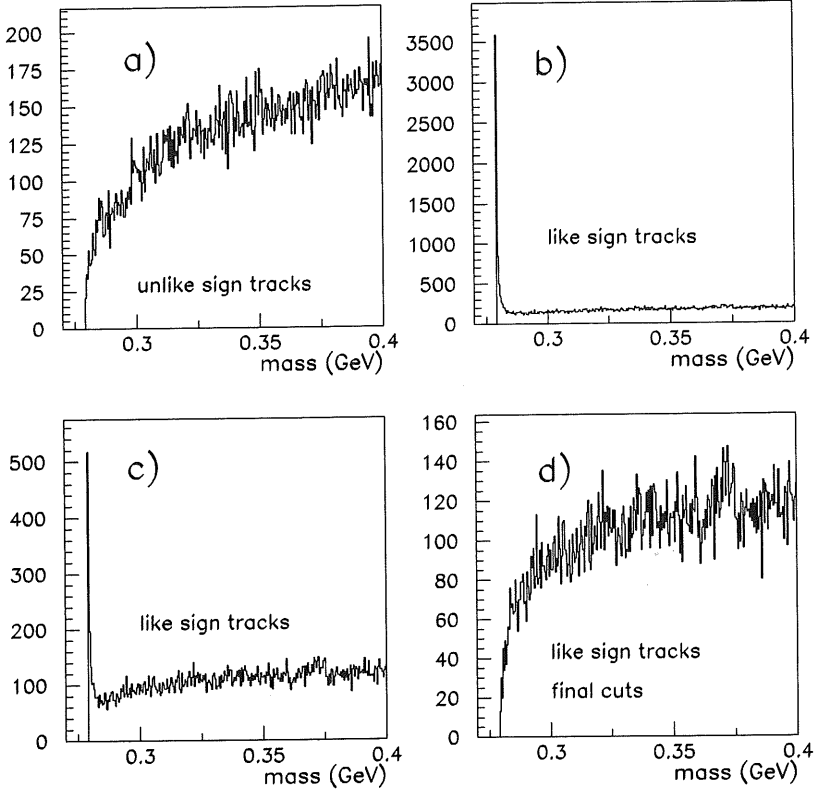


Figure 6.4: Invariant mass distribution of pairs of charged tracks : Unlike sign pairs are shown in (a) and like sign ones in (b) where only the acceptance cut in theta and the  $p_t \geq 150 MeV$  requirement is imposed on the track selection. In (c) the same is shown for like sign pairs for tracks starting in the inner jet chamber. In (d) the final selection of like sign pairs after double track rejection is shown.

In this analysis we use either the two particle unlike-sign inclusive distribution  $\rho^{\text{ref}}(M) = \rho_2^U(M)$  or we create uncorrelated pairs by mixing tracks from different events, denoted by  $\rho^{\text{ref}}(M) = \rho_1 \otimes \rho_1(M)$  to simulate the background data sample. These two techniques are commonly used in different experiments [45, 42, 46, 47].

The whole analysis was done in two steps in order to study systematic effects and to be able to compare the results with other experiments which used the same analysis method.

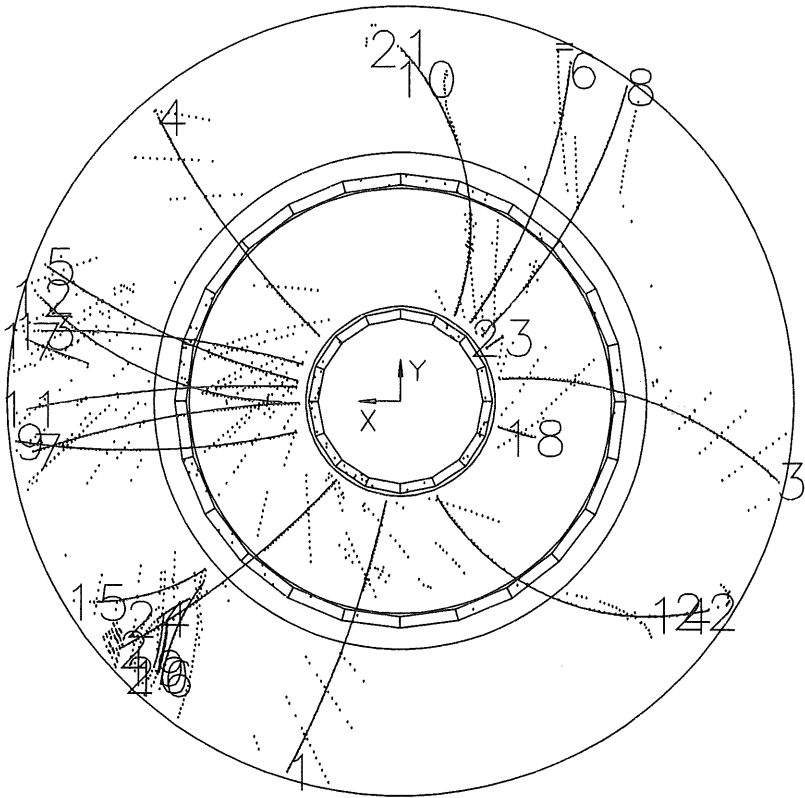


Figure 6.5: Radial view of a typical low  $Q^2$  event. The invariant mass of some pairs is very small and enters in the first ten bins of the mass distribution.

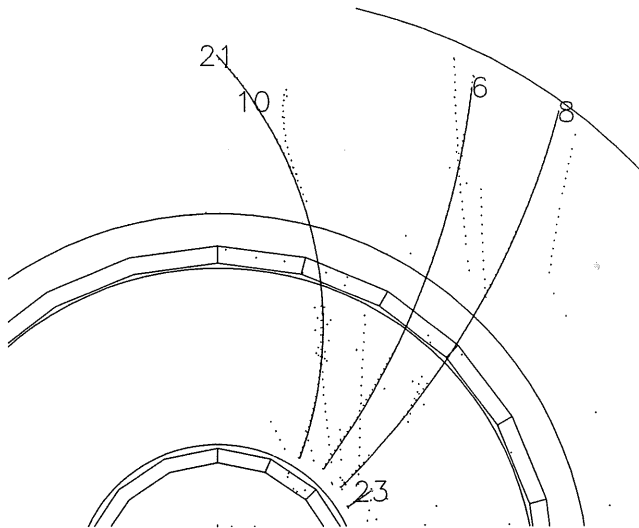


Figure 6.6: Two tracks (No. 6 and 8) with a very small invariant mass of 298  $MeV$  used for BEC analysis.

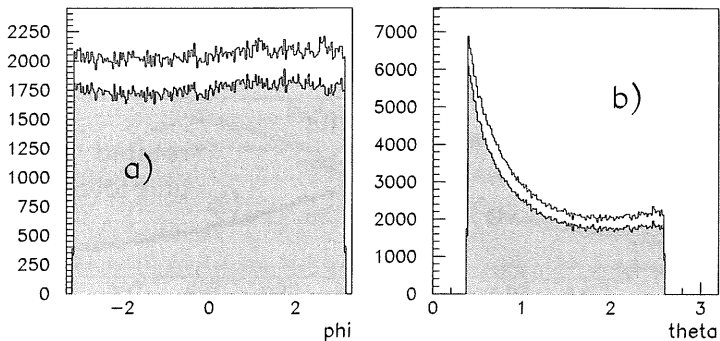


Figure 6.7: The final track selection (grey) is compared to those tracks where only the cut on theta is imposed (white). (a) represents the distribution of the angle  $\phi$  while (b) shows the angle  $\vartheta$  of the tracks.

In a first step all events were divided into four classes according to the invariant mass of the final hadronic system  $W$  and for each event a partner event was found within the same class. Track pairs were formed with one track from the event under study and the other from the partner event (first analysis).

In a second step the event-mixing technique was improved. Up to 20 partner events were found for that event under study (second analysis). Classes according to the invariant mass of the final hadronic system  $W$ , the four momentum transfer of the scattered electron and the multiplicity of selected charged tracks are formed and only candidates in the same class are mixed. This second method increased the number of available combinations drastically and reduced potential bias by mixing events which are not equivalent in their kinematics. The results of both methods will be presented.

The invariant mass of a track pair is calculated in formula 6.1 containing the opening angle between the pair. If we mix events which typical jet structure and if the corresponding jet axes are not collinear in space the invariant masses of the mixed pairs became larger on average than the corresponding inclusive density  $\rho_2(M)$  of pairs from the same event. The result manifests itself as a slight shift of the phase space shape which can be seen in any distribution of  $\rho_1 \otimes \rho_1(M)$  (see Figure 6.11).

Rotation of the partner event in the  $r$ - $\phi$  plane such that positron tracks have the same direction in the  $r$ - $\phi$  projection reduces this bias slightly as depicted in Figure 6.8 (a). The open circles show the original invariant mass distribution of the mixed pair sample  $\rho_1 \otimes \rho_1(M)$  and the full dots represent the same distribution but with rotated partner event which is used to mix the tracks.

Further studies were done with a selection of different event topologies. A cone jet-algorithm



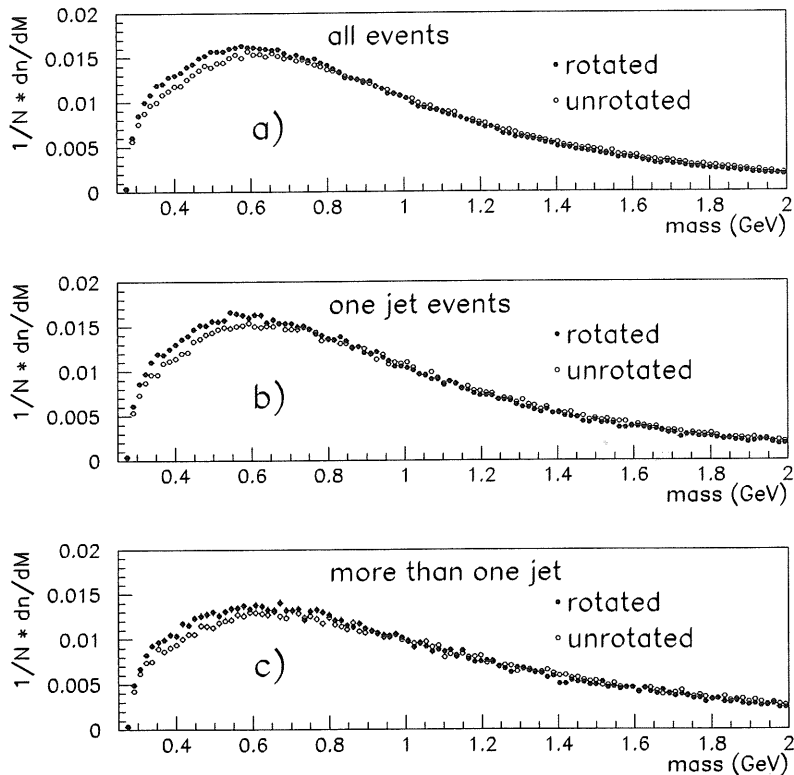


Figure 6.8: Invariant mass distributions of pairs of like sign tracks from different events  $\rho_1 \otimes \rho_1(M)$ . Full dots illustrates the mass spectrum of the mixed event sample where the second event is rotated in the  $r-\phi$  plane such that the projection on the  $r-\phi$  plane of the scattered positron track has the same direction with the event studied. Open circles belongs to the mass spectrum of mixed pairs where the partner event is not rotated and is hence shifted towards higher masses. In (b) and (c) the same is shown for two selected event classes where only one single jet could be found (b) and where more than one jet is found by a cone jet algorithm (c).

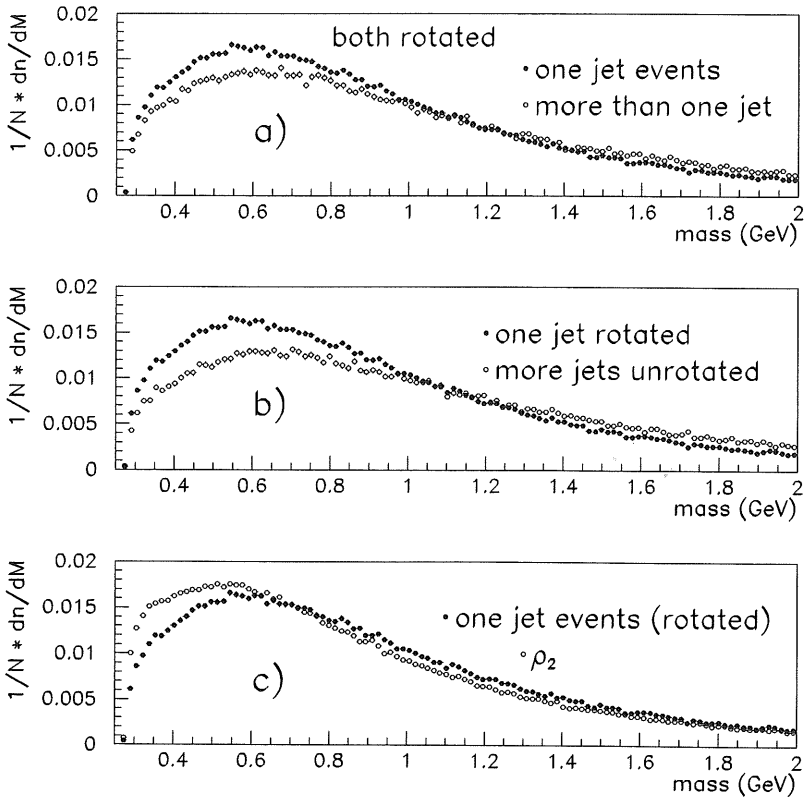


Figure 6.9: Invariant mass distributions of pairs of like sign tracks from different events  $\rho_1 \otimes \rho_1(M)$ . In (a) the difference in the mass spectrum of the two event samples with selected jet topologies according to Figure 6.8 is shown. Both distributions are formed with events where the partner event is rotated in the  $r$ - $\phi$  plane to match projections in the  $r$ - $\phi$  plane of the positron tracks.

In (b) the partner event of the event sample with more than one jet is remained unrotated, so the maximal shift is visible relative to the one jet sample which is rotated.

(c) Comparison of the original inclusive density  $\rho_2$  of like sign tracks with the rotated one jet sample.

was used to separate two classes of events : those where only one jet was found and those with more than one jet. Figures 6.8 (b) and (c) show the same as Figure (a) but use only pairs from the corresponding classes of events just mentioned. The magnitude of the effect due to rotation is quite the same independent of the topology if only events from the same class are compared but the whole shape of the phase space is more flat in (c). This difference is also illustrated in Figure 6.9 (a) where the two event samples are compared under the same conditions (both with rotated partner event). From Figure 6.9 (b) we can deduce the combined effect of rotation and influence of the multi jet topology on the shape of the invariant mass. We can conclude that a rotation of the second partner event used to mix tracks to get a reference distribution  $\rho_1 \otimes \rho_1(M)$  solves the phase space shift only partly, as apparent from Figure 6.9 (c) where the rotated one jet event sample is compared to the inclusive density  $\rho_2(M)$  of like pairs of pions. On the other hand BEC are incorporated in  $\rho_2^{\text{like}}(M)$  and produce the discrepancy between both curves in the range below 0.7 GeV. The influence of multi-jet events is hence the strongest cause of the rise at small masses in the ratios

$$R(M) = \frac{\rho_2(M)}{\rho_1 \otimes \rho_1(M)} \quad (6.3)$$

(see Figure 6.13 (b) open circles (MC without BEC is used) or in Figure 6.13 (a) where unlike pairs show a slight rise even in the absence of BEC). Full dots in Figure 6.13 (b) include these artificial "correlations" (which have nothing to do with BEC) and BEC together. We expect a flat distribution of the Ratio  $R(M) = \frac{\rho_1 \otimes \rho_1^{\text{like}}(M)}{\rho_1 \otimes \rho_1^{\text{unlike}}(M)}$  as there is no difference in the selection of a like or unlike track pair if we combine the pair from different events. Figure 6.10 (a) proves this supposition. For this reason we simply write  $\rho_1 \otimes \rho_1(M)$  for the mixed reference distribution. In the analysis  $\rho_1 \otimes \rho_1^{\text{like}}(M)$  and  $\rho_1 \otimes \rho_1^{\text{unlike}}(M)$  are added in order to increase the statistics.

To obtain the final result and to extract the BEC from these artificial correlations, we take a double ratio by dividing the correlation Function 6.3 from the data by the one obtained from reconstructed MC events which do not contain BEC:

$$R'(T) = \frac{R^{\text{data}}(T)}{R^{\text{MC}}(T)} \quad (6.4)$$

The extracted BEC effect in the double ratio (Formula 6.4) is shown in Figure 6.14 and there is no enhancement visible in the double ratio for unlike sign pairs (Figure 6.10 (b)) which proves the correctness of the method.

This procedure (double ratio) also corrects for the geometrical acceptance, kinematical cuts, and resonance decays if the unlike-sign reference sample is used to build  $\rho^{\text{ref}}(T)$ . In the end a suitable parameterization of the correlation Function 2.4 is found with equation 2.16 and the double ratio 6.4 is fitted to that function.

The formula (2.16) is the so called "Goldhaber Parameterization" which assumes a Gaussian shape of the pion emitting source (see Chapter 2.3.2. It is worthwhile to note that the two reference samples  $\rho_1 \otimes \rho_1(M)$  and  $\rho_2^{\text{like}}(M)$  are not equivalent as was demonstrated by DELPHI in [42] and also discussed in the next Chapter 6.4.

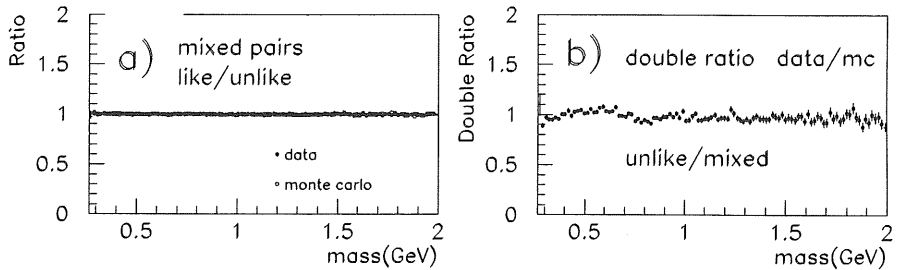


Figure 6.10: Control plots for the event mixing scheme. Full dots represent the detector data and open circles the Monte Carlo generated data.

$$a) \text{ Ratio } R(M) = \frac{\rho_1 \otimes \rho_1^{\text{like}}(M)}{\rho_1 \otimes \rho_1^{\text{unlike}}(M)}.$$

$$b) \text{ Double ratio } R'(T) = \frac{R^{\text{data}}(T)}{R^{\text{MC}}(T)} \text{ where } R(T) = \frac{\rho_2(T) \mathbb{1}(T)}{\rho_1 \otimes \rho_1(T)}.$$

## 6.4 Correlations in invariant mass

All data in this chapter belong to the low  $Q^2$  data-sample and the Monte Carlo based on a parton shower model.

Figure 6.11 shows  $\rho_2(M)$ , the inclusive two-particle density and  $\rho_1 \otimes \rho_1(M)$ , the uncorrelated reference distribution obtained from event mixing. The upper one (a) is for like-sign pairs and the lower one (b) for unlike-sign pairs. The distributions are weighted according to the number of accepted events. The mixing technique is performed according to the second method which yields much more statistics (see Chapter 6.3). Each reference distribution containing mixed track pairs  $\rho_1 \otimes \rho_1(M)$  is weighted with the number of pairs of the corresponding inclusive density  $\rho_2(M)$ , i. e. divided by the ratio  $\frac{\text{number of } \rho_1 \otimes \rho_1(M) \text{ pairs}}{\text{number of } \rho_2(M) \text{ pairs}}$ . A quite sharp peak at  $M \simeq 0.5$  GeV in Figure 6.11 (b) identifies  $K_S^0$  and a rather large flat hump at  $M \simeq 0.77$  GeV stems from the  $\rho^0$  decay. Figure 6.12 shows the same distributions as Figure 6.11 for Monte Carlo events (CDM), after full reconstruction. For further analysis, the first bin in Figures 6.11 and 6.12 was excluded because their content is strongly affected by reconstruction bias, especially in the like-sign sample. This bin is therefore not shown in the Figures 6.13 and 6.14. The effect of BEC can be seen in the Figures 6.11(a) and 6.12(a) in a different shape of the inclusive density  $\rho_2(M)$ . The discrepancy between  $\rho_2(M)$  and  $\rho_1 \otimes \rho_1(M)$  is discussed in Chapter 6.3 in detail. Figure 6.13 (a) shows the ratio  $R(M) = \frac{\rho_2^{\text{unlike}}(M)}{\rho_1 \otimes \rho_1(M)}$  for both data and the CDM-model. This unlike-sign inclusive density, normalized to the reference sample from event-mixing displayed in Figure 6.13 (a) is used as a check of the Monte Carlo predictions. The fragmentation models overestimate the amount of  $\rho$  production, as previously observed in the references [44, 45, 42, 46] and discussed in Chapter 6.5.1, but otherwise good agreement between data and MC is observed. In Figure 6.13

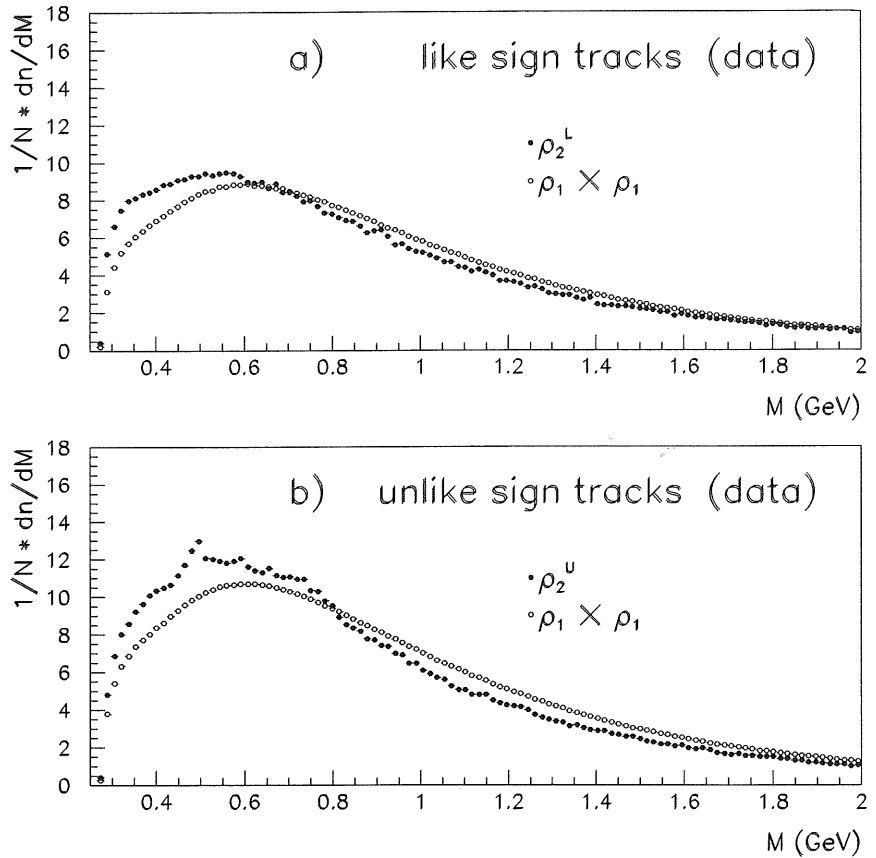


Figure 6.11: The invariant mass distribution of pairs of tracks, normalized to the number of accepted events  $N$ .

a) Full dots denote the two particle inclusive spectrum for like-sign pairs ( $\rho_2(M)$ ). The open circles represent the distribution obtained from event mixing  $\rho_1 \otimes \rho_1(M)$ .

In b) the same is shown for unlike-sign pairs: full dots  $\rho_2^U(M)$  and open circles  $\rho_1 \otimes \rho_1(M)$ .

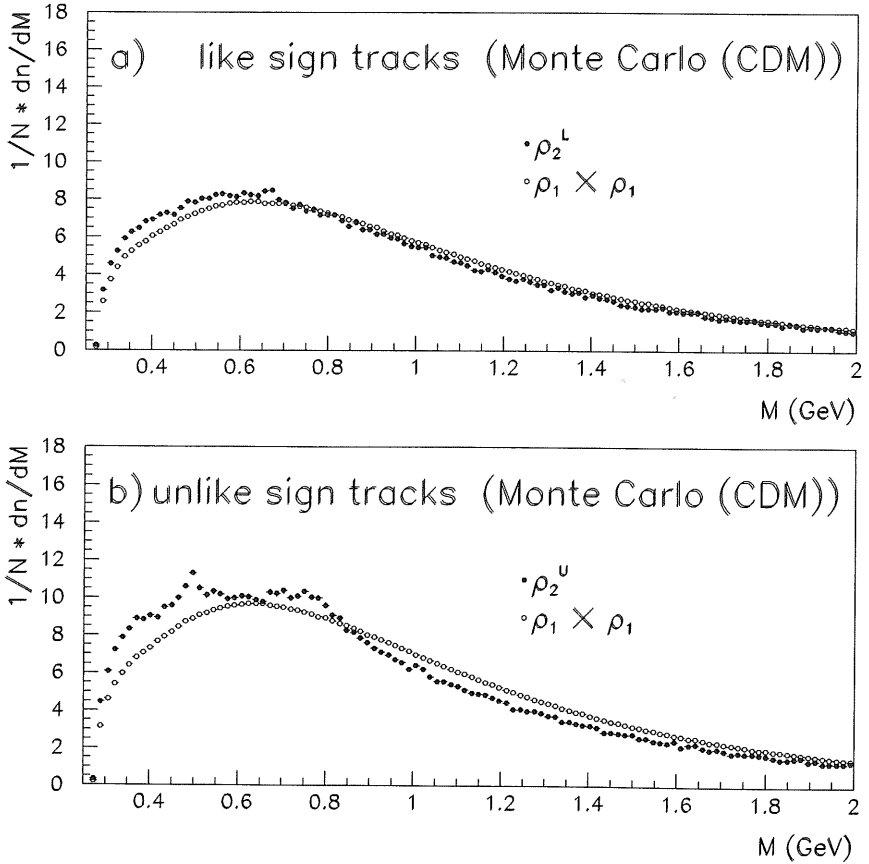


Figure 6.12: The same as Figure 6.11 for Monte Carlo events.

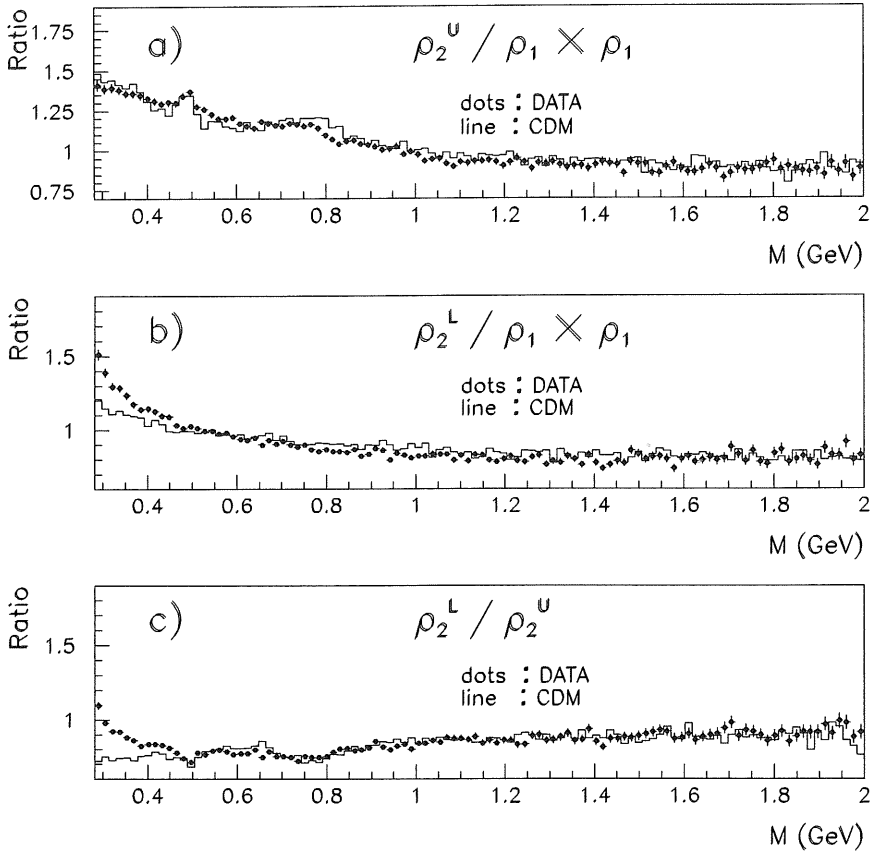


Figure 6.13: The ratio  $R(M) = \rho_2(M)/\rho_2^{\text{ref}}(M)$  for three combinations:

a) Ratio  $R(M) = \rho_2^U(M)/\rho_1 \otimes \rho_1(M)$ .

b) Ratio  $R(M) = \rho_2(M)/\rho_1 \otimes \rho_1(M)$  (with MC model without simulated BEC).

c) Ratio  $R(M) = \rho_2(M)/\rho_2^U(M)$ .

The full dots represent the data, the histograms represent the CDM Monte Carlo. The difference between Monte Carlo and data in (b) and (c) is attributed to the Bose-Einstein correlations.

(b) we see the ratio  $R(M) = \rho_2^1(M)/\rho_1 \otimes \rho_1^1(M)$  for like-sign pairs where the reference sample is obtained from event mixing. The experimental values of  $R(M)$  are considerably higher than those of the MC for  $M$  smaller than  $0.6 \text{ GeV}/c^2$ . This is usually attributed to the Bose-Einstein interference. The Monte Carlo also predicts a rise of  $R(M)$  towards threshold. These correlations are mainly caused by mixing tracks of events with a different jet topology which generates a shift towards larger masses and a depletion of the  $\rho_1 \otimes \rho_1(M)$  distribution at small masses as discussed in Chapter 6.3. These residual (non-BE) correlations should be nearly absent for events with no typical jet structure, as discussed in [42, 46]. From this discussion and the agreement of data and Monte Carlo demonstrated in Figure 6.13 (a), it becomes apparent that the double ratio of equation 6.4 should be used to fit the BE enhancement of equation 2.16. Figure 6.13 (c) shows the ratio of like-sign  $\rho_2^1(M)$  over unlike-sign  $\rho_2^1(M)$  two-particle densities. Clear  $K_s^0$  and  $\rho^0$  signals at  $0.5$  and  $0.77 \text{ GeV}$ , respectively, are visible in both Figures 6.13 (a) and (c).

The double ratios of data and Monte Carlo for signal and reference sample (Figure 6.13 (b) and Figure 6.13 (c)), i. e. the quantity  $R'(T) = R^{\text{data}}(T)/R^{\text{MC}}(T)$  are shown in Figure 6.14 (a) and Figure 6.14 (b) respectively. The fit of the ‘‘Goldhaber parameterization’’ (2.16) is superimposed. In Figure 6.14 (a) the region around the  $\rho^0$  and the  $K_s^0$  is excluded from the fit. This corresponds to a range of  $0.65 - 0.85 \text{ GeV}$  and  $0.38 - 0.43 \text{ GeV}$  in the variable  $T$ . Note that these plots show the variable  $T$  instead of the mass.

## 6.5 Comparison with Monte Carlo

The use of Monte Carlo generators is an integral part of this BEC analysis in order to correct systematic effects, to study resolution and errors and to build the double ratio  $R'(T)$  (equation 6.4).

The hadronic final state of neutral current DIS events was modeled using two different Monte Carlo generators in this analysis (see Chapter 6.5.2 for details).

The Monte Carlo simulation program H1SIM which is based on the GEANT CERN package [57] was used to simulate the detector response in detail and correct the data for geometrical acceptance, kinematical cuts, resolution and particle interactions with the detector material.

The simulated events were finally processed through the same reconstruction chain as real data.

### 6.5.1 Track finding efficiency and correction factors

Correction factors were calculated per bin of invariant mass as the ratio of the generated to the accepted number of pairs. This is done by selecting charged particles at the generator level which do not decay at the generator level. The same kinematical and geometrical cuts as on the reconstructed quantities are imposed for the generated particles. Figure 6.15 shows the correction factors for  $\rho_2(M)$  and  $\rho_1 \otimes \rho_1(M)$  and for the ratio of the two. Slightly more track at the generator level (denoted as ‘‘GEN’’) are visible compared to the simulated and reconstructed Monte Carlo data (denoted as ‘‘MSR’’). These numbers differ due to technical cuts on the impact parameters such as the reconstructed tracks have to begin within the inner jet chamber or the requirement of at least 10 hits on each track. The correction factors for the



## MEAR

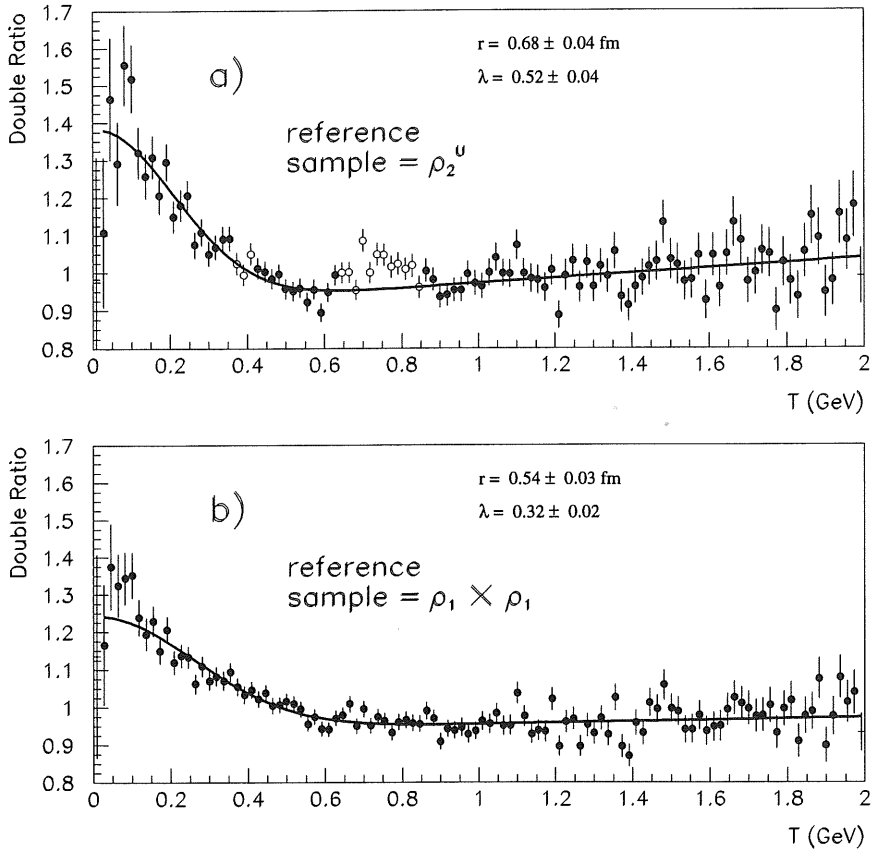


Figure 6.14: Double ratio  $R'(T) = R^{\text{data}}(T)/R^{\text{MC}}(T)$  for  $R(T) = \rho_2(T)/\rho_2^u(T)$  in (a) and for  $R(T) = \rho_2(T)/\rho_1 \otimes \rho_1(T)$  in (b), here displayed as function of the variable  $T = \sqrt{M^2 - 4m_\pi^2}$ . The fitted values for  $r$  and  $\lambda$  corresponds to the "Goldhaber Parameterization" 2.16.

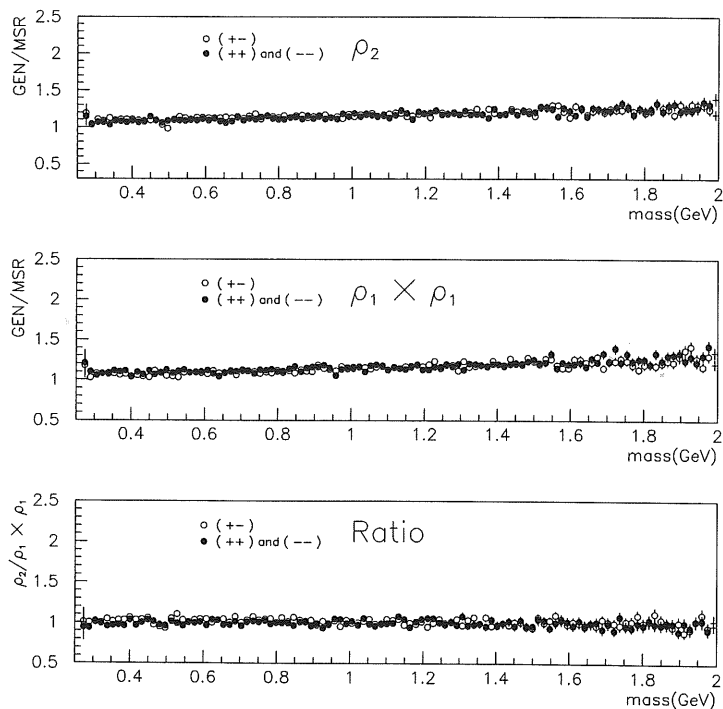


Figure 6.15: Correction factors as the ratio of generated ("GEN") particles to that of simulated and reconstructed ones ("MSR") used for a) the two particle densities  $\rho_2(M)$ , b) the uncorrelated background  $\rho_1 \otimes \rho_1(M)$  and c) the ratio  $R(M) = \frac{\rho_2(M)}{\rho_1 \otimes \rho_1(M)}$ .

ratio  $R(M) = \rho_2^1(M)/\rho_1 \otimes \rho_1(M)$  shown in Figure 6.15 (c) are equal to unity and are smooth as a function of mass, except for the unlike sign combination (open circles) at  $M \simeq 0.5$  GeV, where a small influence of  $K_s^0$  decay is seen which is not completely suppressed by the fit to the primary vertex in the "MSR" sample but which is excluded in the generator sample as it is considered a stable particle at the generator level. These correction factors are applied to the data in order to compare data directly with the raw generated ("GEN") quantities. If we form the double ratio with reconstructed Monte Carlo data ("MSR") then these correction factors drop out. The correction factors are multiplied bin-by-bin to the data sample and can be compared to the generated distributions ("GEN") illustrated in 6.16. The main physical quantities remain unchanged after applying the correction factors. The peak from the  $K_s^0$ -decays visible in the simulated data in Figure 6.13 (a) was disappeared, but it is still present in the data. Figure 6.16 (a) shows quite good agreement of the Monte Carlo prediction with the data if we neglect the region below 1 GeV where some resonances are dominant which are not well reproduced by the Monte Carlo. Especially the production rate of the  $\rho^0$  meson and in the very low mass region the  $\eta'$  resonance are overestimated. This is a known effect in the JETSET model, also stressed in other experiments [46, 42]. It is also evident in the double ratio of Figure 6.10 (b) which should be completely flat if resonance production is properly simulated in the Monte Carlo or in an enhancement in the double ratio 2.16 visible in 6.14 (open circles).

Contrary to the relative agreement of the data with the simulation, the ratio with the like-sign distribution (Figure 6.13 (b))  $R(M) = \rho_2^{\text{like}}(M)/\rho_1 \otimes \rho_1(M)$  is not reproduced by the Monte Carlo except for masses below 1.2 GeV. This disagreement is usually attributed to the Bose Einstein effect. These Figures are however in good agreement with other experiments like [42]. As already stressed by the DELPHI collaboration [42] there is a much better agreement of data with Monte Carlo in the case of  $x_{\pi\pi} \geq 0.01$ , where  $x_{\pi\pi} = 2 |p|/W_{\text{cm}}$  and  $p$  is the momentum of the  $\pi\pi$  system and  $W_{\text{cm}}$  is the total hadronic energy of the event. Pairs of tracks are selected which have a value of  $x_{\pi\pi}$  in this two regions. Figure 6.17 shows the mass distribution of the two data-samples and confirm the observation of the DELPHI collaboration.

To rely on the simulation program a comparison between some track parameters of data and reconstructed Monte Carlo tracks was made. Pairs with low invariant masses, i. e. in the first bin used in the analysis are selected both in data and in MC. As explained in section 6.3 this low mass region is the most interesting and most important kinematical regime for BEC. Since a variety of effects can enhance or reduce the ratio between like and unlike sign tracks the following quantities were compared :

- track starting point
- track end point
- track length in the  $r - \phi$  plane
- number of hits in the inner jet-chamber
- number of hits in the outer jet-chamber
- number of hits in the  $z$ -chambers (CIZ and COZ separately)
- $\vartheta$
- $\phi$
- total momentum

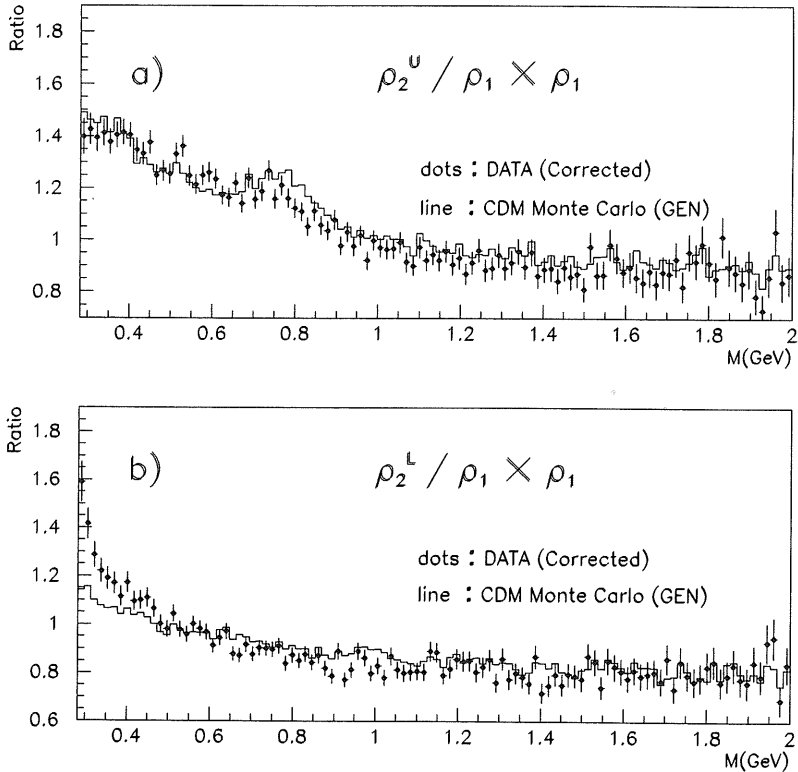


Figure 6.16: a) Ratio  $R(M) = \frac{\rho_2^{\text{unlike}}(M)}{\rho_1 \otimes \rho_1(M)}$  for corrected data (full dots) and generated Monte Carlo ("GEN") data (line). b) Ratio  $R(M) = \frac{\rho_2^L(M)}{\rho_1 \otimes \rho_1(M)}$ .

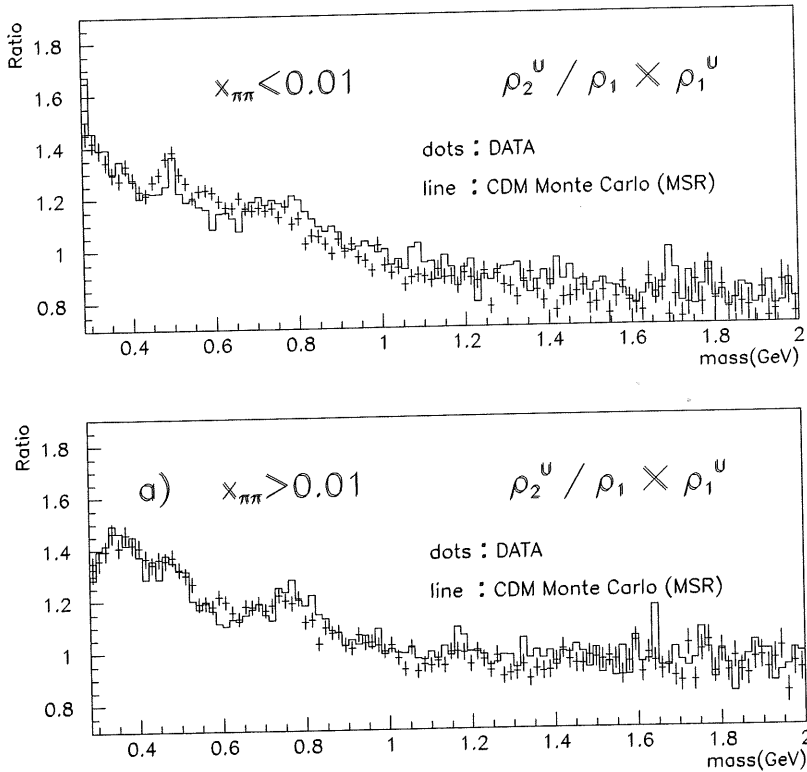


Figure 6.17:  $R(M) = \frac{\rho_2^{\text{unlike}(M)}}{\rho_1 \otimes \rho_1(M)}$  for a)  $x_{\pi\pi} \leq 0.01$  and b)  $x_{\pi\pi} \geq 0.01$ . Both plots use uncorrected data and the CDM Monte Carlo generator with reconstructed data.

– transverse momentum

The plots are not shown. However, good agreement is found between data and MC for that critical region in the invariant mass distribution.

### 6.5.2 Comparison of different Monte Carlo generators

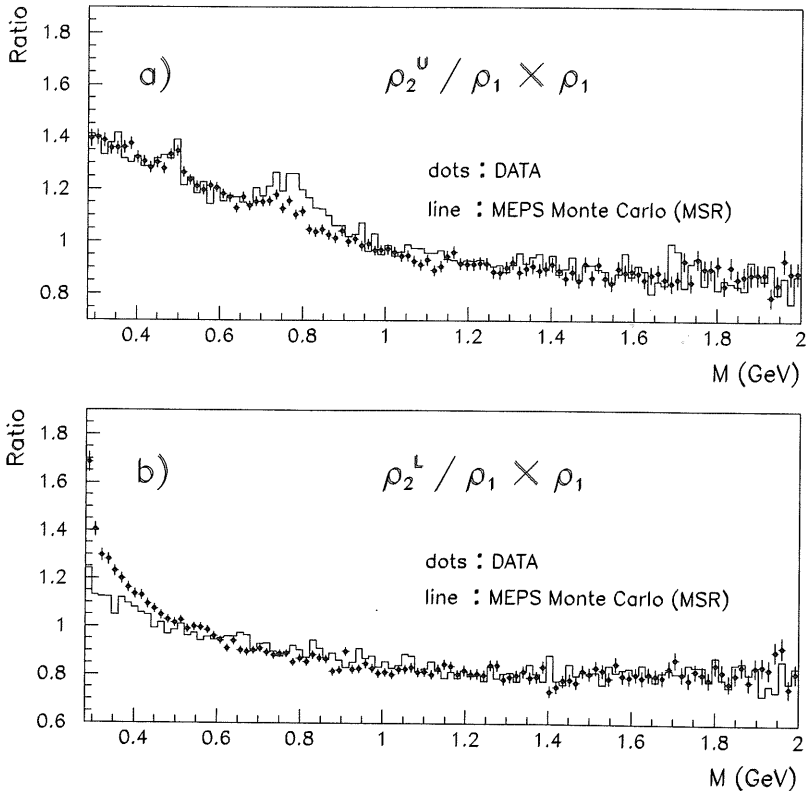


Figure 6.18: The same distributions as in figure 6.13 but for the parton shower model instead of the color dipole model.

As already mentioned two different Monte Carlo models are compared with data : the Color Dipole Model (CDM) and the parton shower model (MEPS). Figure 6.18 shows the same as 6.13

(a) and (b) but for the Parton Shower model. With the data the agreement is are slightly better than for the CDM model. In the figures we sometimes use the abbreviations "GEN" and "MSR" which stand for generated Monte Carlo (GEN) data and detector simulated and reconstructed Monte Carlo data (MSR). "MEAR" and "CDM" means the same data from a MOnTe Carlo generator which uses an algorithm based on the color dipole model. "MEPS" uses the parton shower model to generate deep inelastic scattering events.

### 6.5.3 Monte Carlo with BEC included

A crude option for the simulation of Bose Einstein correlations is included in the JETSET Monte Carlo (subroutine LUBOEI) and written by Torbjörn Sjöstrand [8]. What is offered is merely a algorithm but not a model based on a physical concept. In this scheme, the fragmentation is allowed to proceed as usual, and so is the decay of short-lived particles like  $\rho$ . Then pairs of identical particles,  $\pi^+$  say, are considered one by one. The  $T_{ij}$  value of a pair  $i$  and  $j$  is evaluated,

$$T_{ij} = \sqrt{(p_i + p_j)^2 - 4m^2} \quad (6.5)$$

where  $m$  is the common particle mass. A shifted (smaller)  $T'_{ij}$  is then to be found such that the ratio  $C_2(T)$  of shifted to unshifted  $T$  distributions is given by the requested parameterization. The shape may be chosen either exponential or Gaussian,

$$C_2(T) = 1 + \lambda \exp(-(T/d)^r), \quad r = 1 \text{ or } 2 \quad (6.6)$$

The change in  $T_{ij}$  can be translated into an effective shift of the three- momenta of the two particles. The Bose Einstein effect is here interpreted almost as a classical force acting on the "final state", rather than a quantum mechanical phenomenon on the production amplitude.

The inclusive density  $\rho_2(M)(\text{GEN}(\text{BE}))$  for like pairs formed by the generated quantities of the Monte Carlo program which contains BEC is shown in Figure 6.19 (a) (full dots) and the same distribution for the Monte Carlo without BEC (open circles). The phase space shift is apparent and may be compared with the invariant mass spectra obtained with the mixed reference method  $\rho_1 \otimes \rho_1(T)$  from Figure 6.11 (a). In the ratio  $\rho_2(M)(\text{GEN}(\text{BE}))/\rho_2(M)(\text{GEN})$  (Figure 6.19 (b)) the input value for the generator (given in appendix A) of 0.53 fm is nearly extracted.

Figure 6.20 show the much better agreement of the Monte Carlo with the data mainly in (b) where the like sign inclusive density is shown. The correction factors are applied to the data and generated data (GEN) with the BEC included are plotted. These distributions have to be compared with Figure 6.16 where the same quantities are shown without the simulation of BEC in the Monte Carlo program. The uncorrected data are compared in Figure 6.21 to reconstructed Monte Carlo events. We find an almost perfect agreement between Monte Carlo and data, if the BEC is included in the generators. The gap of the distributions below 0.6 GeV in Figure 6.13(b) is nearly disappeared and even in the higher mass region above 0.6 GeV the Monte Carlo is in better agreement with the data than in Figure 6.13 (b). The strength of the BEC effect is still less pronounced in the Monte Carlo than in the data resulting in a slight rise for very low masses in the double ratio in Figure 6.22 (b) where  $R'(T) = R^{\text{data}}(T)/R^{\text{MSR}(\text{BE})}(T)$  is outlined. The BEC signal has really disappeared, only a very slight enhancement is visible below 0.05

GeV in the variable  $T$ . The extracted values of the correlation Function 2.16 are compared in Figure 6.22 (a), (c) and (d). Figure (a) shows the same distribution as Figure 6.14. In 6.22 (b) the Monte Carlo background  $R^{\text{MC}}(T)$  is replaced by the file which incorporates simulated BEC. A perfect simulation would produce a flat distribution. Figures (c) and (d) deal with the double ratio  $R'(T) = R^{\text{MSR(BE)}}(T)/R^{\text{MSR}}(T)$  and  $R'(T) = R^{\text{GEN(BE)}}(T)/R^{\text{GEN}}(T)$  respectively and illustrate the difference between generated and reconstructed Monte Carlo data. The BEC survive the whole simulation and reconstruction nearly unbiased and the values of the parameters extracted agree within  $\simeq 1.5$  standard deviations with those used in the generator step. All numbers are summarized in section 6.10.

The differences between Figures 6.22 (a), (c) and (d) are used to estimate the systematic effects of the reconstruction procedure. The precise parameters which are used for the JETSET Monte Carlo to simulate BEC are given in Appendix A.

## 6.6 Final state interactions and corrections

The final state of two or more charged bosons is affected by strong and electromagnetic interactions. Strong interactions are very difficult to calculate. An estimation of the effect has been made by Suzuki [32]. A correction factor for this effect does not exist and no correction has been performed. The electromagnetic interactions in the final state appear in two ways. First the particle interacts with the system as a whole and secondly it interacts with the partner in the pair. The interaction of the particle with the remaining system is not considered to influence the two particle correlations and its effect is neglected [12]. The electromagnetic interaction between pairs of particles is considered below and corrections were applied to the data.

### 6.6.1 Coulomb correction

Coulomb forces between charged pairs of particles accounts for electromagnetic attraction and repulsion and are expected to modify the two particle correlation. Since two unlike (like) charged bosons experience electromagnetic attraction (repulsion), the number of pairs in the region of small relative momenta is enhanced (suppressed). The correction factors for this effect are known as Gamov factors [9]. For like ( $l$ ) and unlike ( $u$ ) charged pairs the inclusive corrected distribution is given by :

$$\rho_2^{\text{like corr}}(M) = G_l(\eta)\rho_2^{\text{like}}(M) \quad (6.7)$$

$$\rho_2^{\text{unlike corr}}(M) = G_u(\eta)\rho_2^{\text{unlike}}(M) \quad (6.8)$$

where  $\rho_2^{(\text{un})\text{like}}(M)$  is the uncorrected and  $\rho_2^{(\text{un})\text{like corr}}(M)$  the corrected inclusive distribution and

$$G_l(\eta) = \frac{2\pi\eta}{\exp(2\pi\eta) - 1} \quad (6.9)$$

$$G_u(\eta) = \frac{2\pi\eta}{1 - \exp(-2\pi\eta)} \quad (6.10)$$

$$\eta = \frac{\alpha m_\pi}{\sqrt{T^2}} \quad (6.11)$$



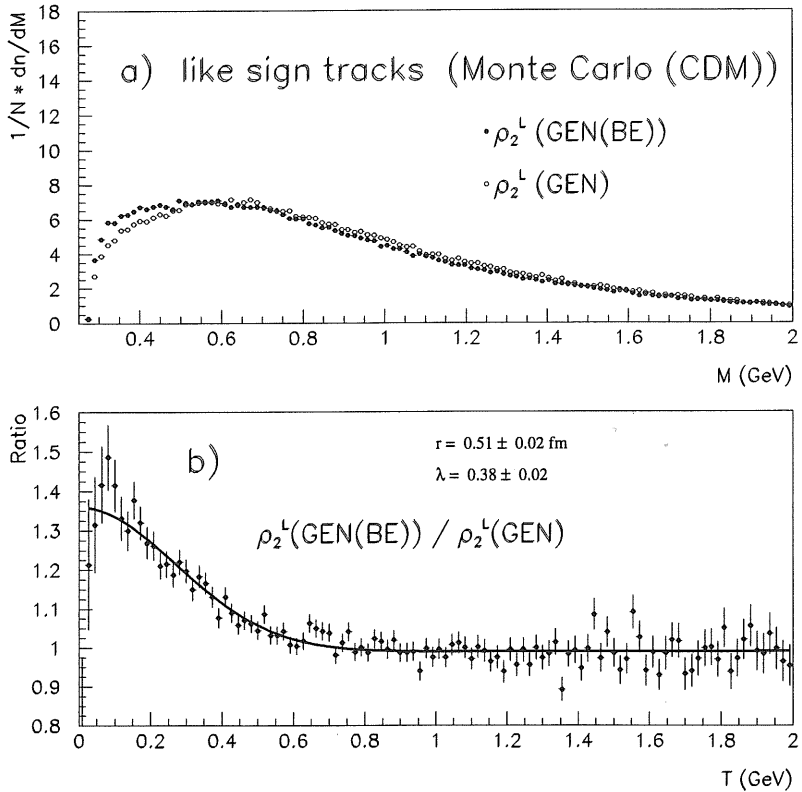


Figure 6.19: Comparison of the Monte Carlo with and without simulated BEC.

a) The two particle inclusive spectrum of like-sign pairs ( $\rho_2(M)(\text{GEN}(\text{BE}))$ ) of generated Monte Carlo data which includes BEC (full dots) and ( $\rho_2(M)(\text{GEN})$ ) from the Monte Carlo without simulated BEC (open circles).

b) Ratio  $\rho_2(M)(\text{GEN}(\text{BE})) / \rho_2(M)(\text{GEN})$ .

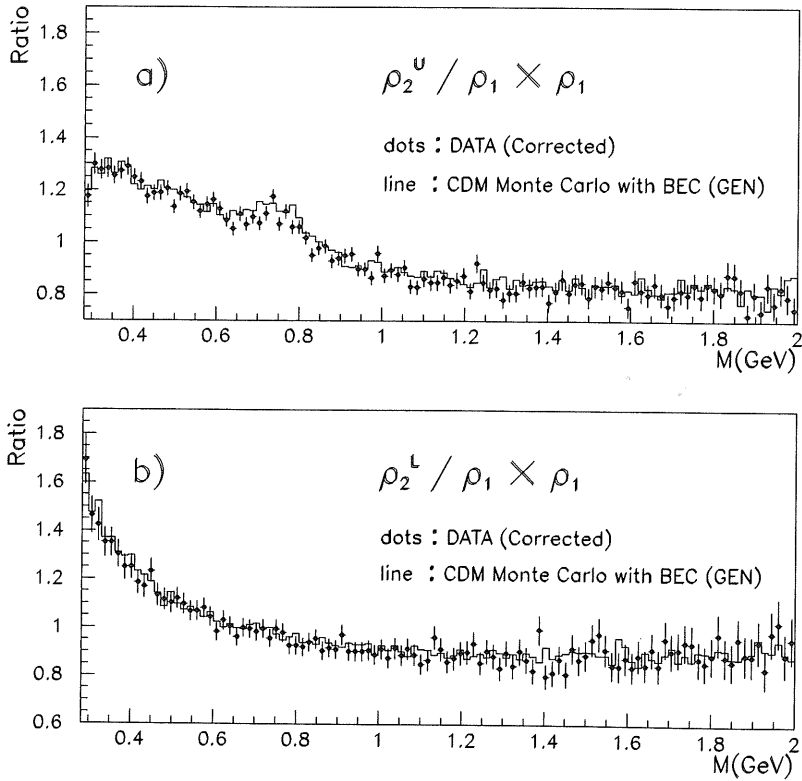


Figure 6.20: The same distributions as in Figure 6.16 but with the Bose Einstein correlation included in the CDM Monte Carlo.

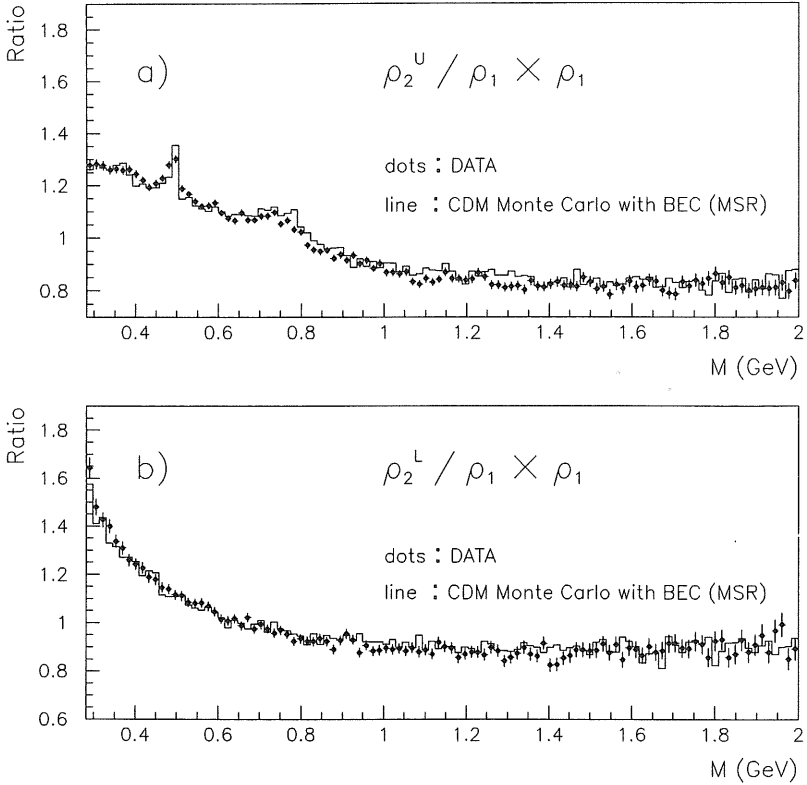


Figure 6.21: The same distributions as in Figure 6.20 but with reconstructed Monte Carlo data and uncorrected data.

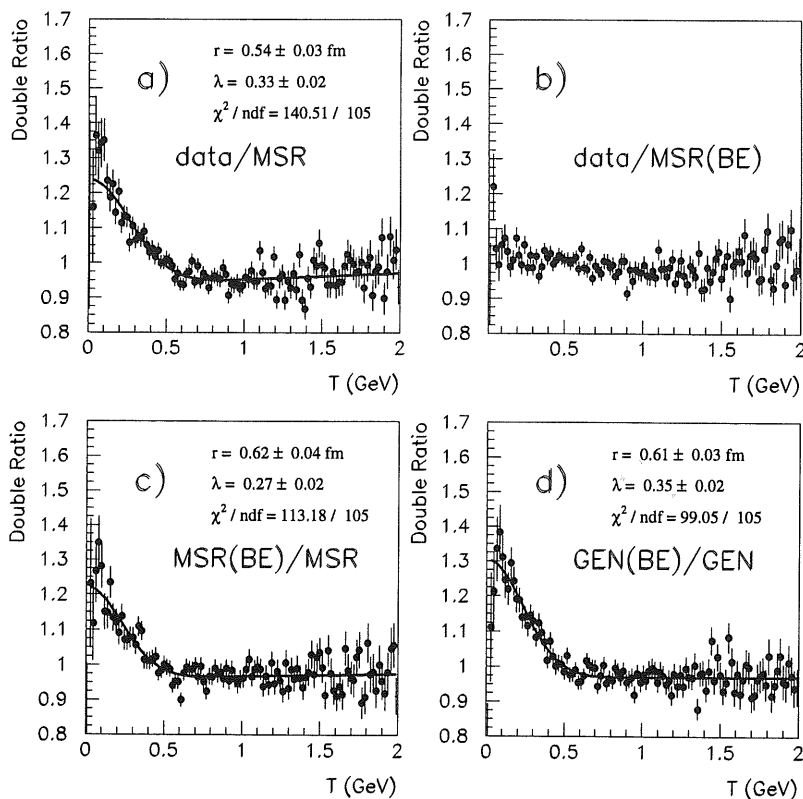


Figure 6.22: Comparison of the data with the Monte Carlo with BEC included. Double ratio

$$R'(M) \text{ for } R(M) = \frac{\rho_2(M)}{\rho_1 \otimes \rho_1(M)}$$

The fitted values for  $R$  and  $\lambda$  corresponds to the "Goldhaber Parameterization" formula 2.16.

- a) Double ratio  $R'(M) = R^{\text{data}}(M) / R^{\text{MSR}}(M)$
- b) Double ratio  $R'(M) = R^{\text{data}}(M) / R^{\text{MSR(BE)}}(M)$
- c) Double ratio  $R'(M) = R^{\text{MSR(BE)}}(M) / R^{\text{MSR}}(M)$
- d) Double ratio  $R'(M) = R^{\text{GEN(BE)}}(M) / R^{\text{GEN}}(M)$

where  $\alpha = 1/137$ , and  $T^2$  is the four momentum difference between the two particles. As can be seen in Figure 6.23, the correction is significant only at very small values of  $T^2$ . The correction is performed bin by bin weighting the distribution by the corresponding Gamov factor. The Coulomb repulsion is not simulated in the Monte Carlo generated events and does not appear in the sample of mixed events. In [12] M.G.Bowler stressed that the Coulomb corrections to BEC are greatly exaggerated by applying the Gamov factors. The overestimation can reach a value up to 20%. In this analysis the Gamov factors were applied only for completeness to be able to compare the data with other experiments treated similarly. The results are again summarized in Chapter 6.10.

## 6.7 Purity and its correction

Resonance production plays an important role in the study of Bose Einstein correlations. If the reference sample  $\rho^{\text{ref}}(M)$  is formed with unlike sign pairs, dips due to decay products of resonances in the ratio  $R(M) = \frac{\rho_2(M)}{\rho_2(M)^{\text{unlike}}}$  can influence the result of the analysis and bias the extracted parameters. The suppression of the ‘‘coherence’’ factor  $\lambda$  from its maximum value is caused mainly by resonance decays. It is known [46, 43] that pions are effectively uncorrelated within the experimental resolution if they are produced from the decays of long-lived resonances. Special studies were done to test this [43].

### 6.7.1 Resonances and decay channels

In the region of the invariant mass we are predominantly encountering  $\eta$ ,  $\eta'(958)$ ,  $\omega(782)$ ,  $K_s^0$  and  $\rho^0(770)$  decays. A special study with the JETSET Monte Carlo data where the particles could be identified is performed. The Figures 6.24 and 6.25 show these channels in the decay chain with two charged pions. In Figure 6.24 (a) we see the phase space of all unlike sign pion pairs. A sharp signal from the  $K_s^0$  is visible superimposed on a broad  $\rho^0$  signal and the continua from the other resonances. Monte Carlo data are shown directly without detector effects. In Figure 6.24 (b) the mainly two body decay of the  $\rho^0(770)$  resonance is present. As the lifetime is very short the width is about 150 MeV. In Figure 6.24 (c) we see the contribution of the  $\omega(782)$  into a pair of unlike sign pions. The sharp peak at 782 MeV belongs to the direct decay into a  $\pi^+\pi^-$  pair with a rate of 2.2% while the other pairs are smeared around low invariant masses as they represent three particle decays. Figure 6.24 (d) illustrates the contribution of the  $\eta$  to the mass of a charged  $\pi^+\pi^-$  pair. The available phase space is limited as the charged channels are 3 body decays and contribute with 30% to all  $\eta$  decays. The mass of charged pion pairs originating from the  $\eta'(958)$  is shown in Figure 6.25 (a). It is the same plot as Figure 6.25 (d) for the  $\eta'$ . As the decay  $\eta' \rightarrow \pi^+\pi^-\eta$  is followed by  $\eta \rightarrow \pi^+\pi^-\pi^0$  or  $\eta \rightarrow \pi^+\pi^-\gamma$ , there are two like sign pion pairs in the total decay chain. We see these pairs in Figure 6.25 (b).

### 6.7.2 Purity correction

In order to correct the data-sample for pions which are not able to interfere the ratio of such particles have to be determined with Monte Carlo data. A special sample of such tracks is

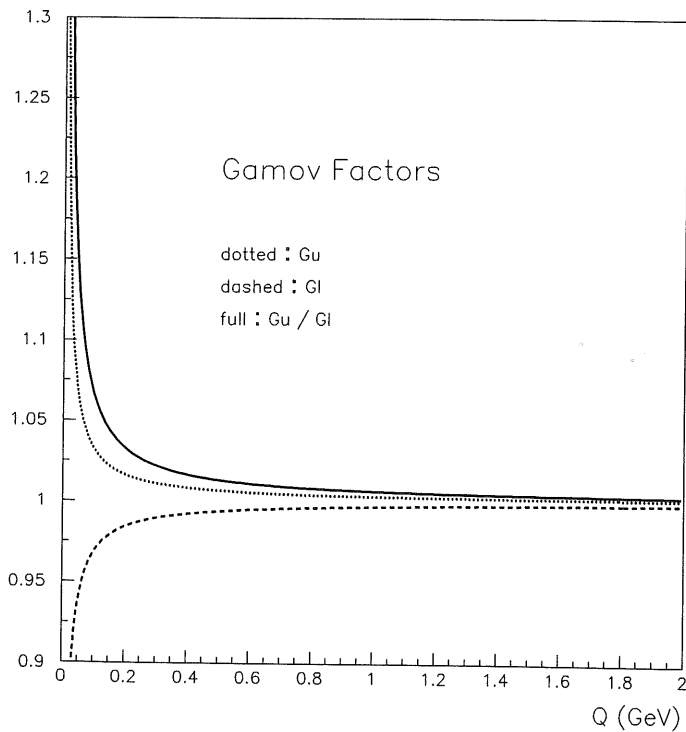


Figure 6.23: Gamov correction factors  $G_l(\eta)$  (dotted line) and  $G_u(\eta)$  (dashed line). The solid line represents the ratio  $\frac{G_u(\eta)}{G_l(\eta)}$ .  $T$  is the four momentum difference between two pions.

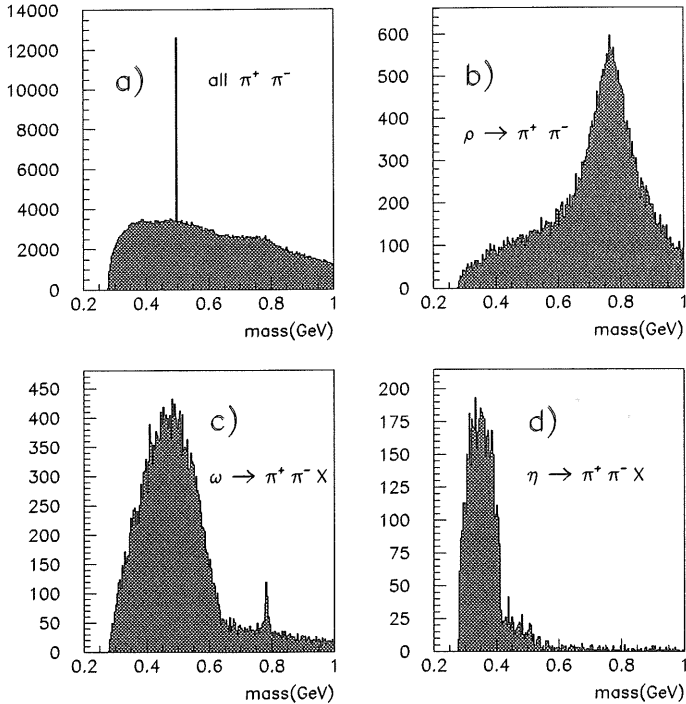


Figure 6.24: The invariant mass distributions of some resonance channels.

(a) All decays in a  $\pi^+ \pi^-$  pair. A sharp signal from the  $K_s^0$  decay is visible together with a broad peak from  $\rho^0$  decay.

(b)  $\rho^0$  decay channel. Only unlike sign  $\pi$  pairs which are decay products of the  $\rho^0$  are plotted.

(c)  $\omega$  decay. A small peak from the rare two pion channel is superimposed on the continuum from three pion decay.

(d)  $\eta$  decays.

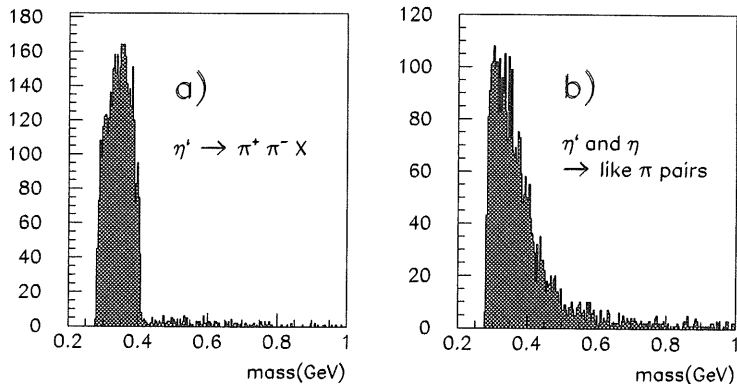


Figure 6.25: The invariant mass distribution of the decay of the  $\eta'$ . in (a) the mass of the two unlike sign pions are plotted and in (b) the mass of all like sign pions from the combined decay of  $\eta$  and  $\eta'$  is shown i. e.  $\eta' \rightarrow \pi^+ \pi^- X$  followed by  $\eta \rightarrow \pi^+ \pi^- \pi^0$  and  $\eta \rightarrow \pi^+ \pi^- \gamma$

created which contains only pions which are directly produced on the string or which are decay products from the same weakly decaying particle. Here and in the following, “direct” pions are taken to be pions which are either produced promptly, or with a mother which has a lifetime shorter than the  $K^*(890)$  (motivated by [42]). In the JETSET model, the fraction of such direct like-sign pion pairs in the sample of all like-sign charge particle combinations, can be well parameterized in the low mass region ( $T = 0. \div 1.2$  GeV/c<sup>2</sup>) by the function:

$$f(T) = 0.183 + 0.26T - 0.095T^2. \quad (6.12)$$

which was experimentally found by fitting the polynomial  $f(T) = P(1) + P(2)T - P(3)T^2$  to the fraction in Figure 6.29 (c). One can correct for the presence of non-direct pion-pion pairs by fitting the double ratio  $R'$  for like-sign pions (Figure 6.14) with a slightly modified form of equation 2.16:

$$R' = N(1 + \delta T)[1 + \lambda f(T) \exp(-T^2 r^2)]. \quad (6.13)$$

The fitted parameter values from the Function 6.13 applied to the uncorrected data and shown in Figure 6.29 (b) are :

$$\lambda = 1.46 \pm 0.10, \quad r = 0.61 \pm 0.03 \text{ fm} \quad (6.14)$$

Using these fitted values of  $\lambda$  and  $r$ , the individual entries of the  $R'(M)$  distribution can be corrected for the finite purity of direct pion pairs by weighting each entry by the factor:

$$\frac{1 + \lambda \exp(-T^2 r^2)}{1 + \lambda f(T) \exp(-T^2 r^2)}. \quad (6.15)$$



The result is shown in Figure 6.29 (c). The fraction of all like-sign pions pairs to all detected particle pairs within the jet chamber has been calculated using the JETSET hadronization procedure and its value varies around 70% as depicted in Figure 6.26 (a). In Figure 6.26 (b) the fraction of all "direct" like-sign pion pairs to all like-sign pion pairs is shown and Figure 6.26 (c) illustrates the fraction of all "direct" like-sign pion pairs to all charged pairs which is parameterized in Function 6.12 and used in 6.13. Both ratios decrease towards smaller masses indicating the influence of long living resonances which decay at least into two pions. Figure 6.26 (d) includes the fraction of like-sign pion pairs directly produced from the string to all like-sign pion pairs which is very tiny and increases towards higher masses since the energy of these pions is normally quite large. The purity correction Function 6.15 to be used to weight the double ratio (Figure 6.14) is illustrated in 6.26 (e).

## 6.8 Dependence of BEC on kinematic variables

Events are selected from the low  $Q^2$  event sample and are divided into classes according to global kinematical variables of the event like the DIS-variable  $x_{\text{Björken}}$  or the multiplicity of tracks in order to study BEC under different conditions. The limited statistics allows only a separation of the full low  $Q^2$  event-sample into two sets. A limit at which the sample is divided was chosen such, that the number of events in each sample is more or less equal.

There are 5 variables investigated:

- $x_{\text{Björken}}$  (see equation 3.5) (limit:  $10^{-3}$ )
- multiplicity of selected tracks in the event (limit: 10)
- invariant mass of the hadronic final state  $W$  (see equation 3.3) (limit: 140 GeV)
- The four momentum transfer  $Q^2$  of the scattered positron (see equation 3.3) (limit: 20 GeV<sup>2</sup>)
- Sum of the momenta of the pion pair:  $|\vec{p}_1 + \vec{p}_2|$  (limit: 1.5 GeV)

The double ratios are formed with each sample and a fit to the correlation Function 2.16 yields the parameters  $r$  and  $\lambda$ . The results are summarized in Table 6.8. Comparing the data-samples with contain events with an  $x_{\text{Björken}}$  of less than 0.001 and the corresponding distribution with  $x_{\text{Björken}} \geq 0.001$  then a slightly other behavior is visible (Figure 6.27). Although the quality of the fit is not so good, a difference towards smaller values of  $r$  is evident for increasing  $x_{\text{Björken}}$ . Comparing the difference between two data-samples where the multiplicity of selected charged tracks is smaller than 10 and bigger than 10 respectively, the magnitude of the  $r$  parameter tends to be higher as the multiplicity increases. This behavior has been observed also in [50]. There is no significant tendency visible in the other three variables as given in Table 6.8.

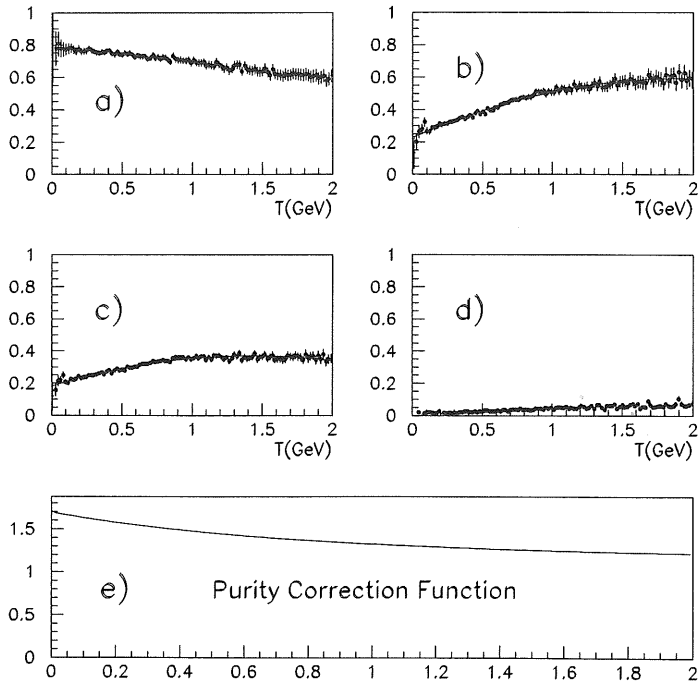


Figure 6.26: (a) Fraction of all like-sign pion pairs to all like sign charged particles.  
 (b) Fraction of all "direct" like-sign pion pairs to all like-sign pion pairs.  
 (c) same ratio as (b) but with all charged particles in the denominator.  
 d) Fraction of like-sign pion pairs directly produced on the string to all like-sign pion pairs.  
 Histogram (c) is used to determine Function 6.12 which is used to form the correction function  $\frac{1+\lambda \exp(-T^2\tau^2)}{1+\lambda f(T) \exp(-T^2\tau^2)}$  shown in (e).

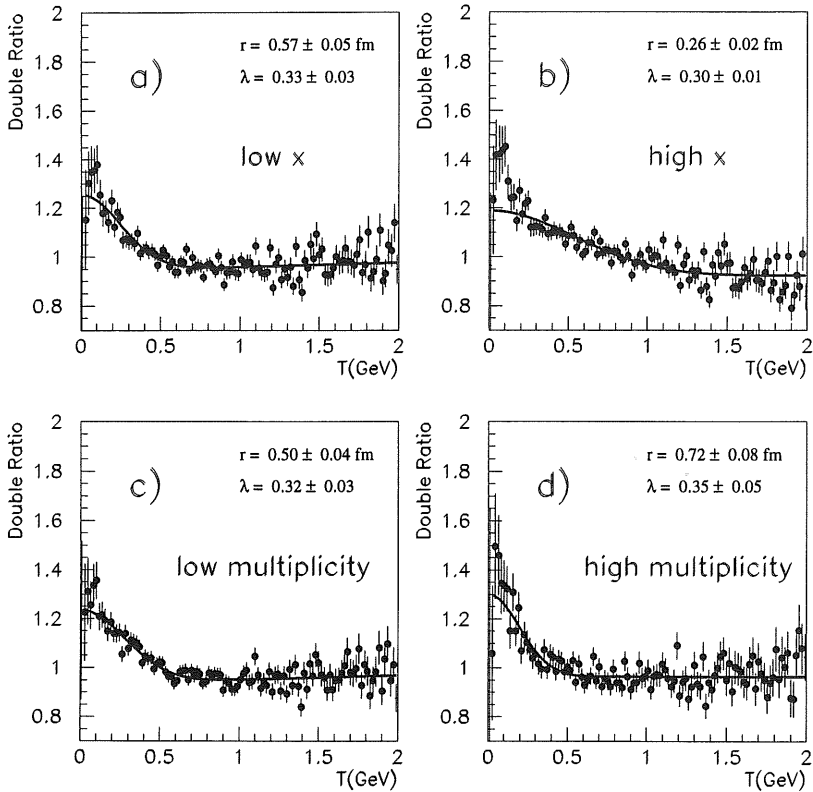


Figure 6.27: Double ratios of four of the data-samples with different event kinematics (event mixing).

a)  $R'(T) = R^{\text{data}}(T)/R^{\text{MSR}}(T)$  for the data-sample with  $x_{\text{Björken}} \leq 0.001$

b)  $R'(T) = R^{\text{data}}(T)/R^{\text{MSR}}(T)$  for the data-sample with  $x_{\text{Björken}} \geq 0.001$

c)  $R'(T) = R^{\text{data}}(T)/R^{\text{MSR}}(T)$  for the data-sample with a multiplicity of less than 10 selected tracks per event.

d)  $R'(T) = R^{\text{data}}(T)/R^{\text{MSR}}(T)$  for the data-sample with a multiplicity of more than 10 selected tracks per event.

## 6.9 Systematic errors

An estimation of the systematic errors was performed using Monte Carlo generated events and a full detector simulation. Two correlation functions were calculated, one at the generator level (GEN) and the other after detector simulation and reconstruction of the Monte Carlo events (MSR). The CDM Monte Carlo with simulated BEC (see Chapter 6.5.3) is used too. The variable  $r$  which correspond to the radius of the source and the "chaoticity" parameter  $\lambda$  from equation 2.16 are the most interesting ones and usually compared with other experiments. In order to assess the influence of an assumption or a particular analysis step on the values of these two parameters a reference distribution (6.17) is chosen and the deviations of the parameter values relative to that reference are determined.

A summary of all values and checks performed is given in the Tables 6.1, 6.2, 6.3 and 6.5 in section 6.10.

For the final error quoted all contributions are added in quadrature. There are five main contributions to the overall systematic uncertainties:

- Finite detector resolution and acceptance effects as well as an imperfect pattern recognition in the reconstruction step can be tested by comparing the generated data-sample ("GEN") with the simulated and reconstructed one ("MSR").
- The choice of parametrization for correlation Function 2.4 is tested by comparison to alternatives used in the literature.
- The influence of the reference sample can be obtained using Monte Carlo generated events with ad hoc inclusion of BEC, i. e. by considering the double ratio

$$R'(T) = \frac{R^{GEN(BE)}(T)}{R^{GEN}(T)}$$

i. e. comparing this double ratio with the outputvalues of the routine LUBOEI in the ratio

$$R(T) = \frac{\rho_2^{GEN(BE)}(T)}{\rho_2^{GEN}(T)}$$

- To check the influence of the event generator we compared the MEPS and CDM Monte Carlo packages.
- Technical differences like bin width, range in  $T$  in which the fit is performed and the influence of the resonances can be checked by varying the corresponding quantities.

In order to understand these results, a few further points need to be mentioned. The three different parametrizations of the correlation Function 2.4 are:

$$f(T) = N(1 + \lambda \exp(-r^2 T^2)) . \quad (6.16)$$

$$f(T) = N(1 + \delta T)(1 + \lambda \exp(-r^2 T^2)) . \quad (6.17)$$

$$f(T) = N(1 + \delta T + \epsilon T^2)(1 + \lambda \exp(-r^2 T^2)) . \quad (6.18)$$

Systematic differences are evident between the fit with all bins and that where the regions of the  $\rho^0$  (0.65–0.85 GeV) and the  $K^0$  (0.38–0.43 GeV in  $T$ ) resonances are excluded. Some experiments only fit a range of 0 – 1.2 GeV in  $T$  instead of 0 – 2 GeV. We investigate both ranges, because it is known that long range correlations may shift the extracted values from different parametrizations.

The errors are furthermore calculated separately for both reference samples  $\rho_2(T)^u$  and  $\rho_1 \otimes \rho_1(T)$ .

Different bin sizes do not influence the result of the fit within the statistical errors. This has been tested using a sample with half the bin-width and an enlarged bin size. The exclusion of the  $\rho^0$  resonance region lowers  $r$  by 10% and enhances  $\lambda$  by 6% if the unlike-sign reference sample is taken. When the “mixed” reference sample is used, the effect is less drastic : a 6% enhancement for  $\lambda$  and a 1.5% decrease for the radius. The  $K^0$  peak has practically no influence on the variation of these values. The larger effect of the  $\rho^0$  can be understood, because the  $\rho^0$  peak appears in a critical region of the invariant mass where the enhancement of the correlation function starts and hence the influence on the radius parameter is noticeable. This is in particular true for the Functions 6.17 and 6.18 which take into account long range correlations. Function 6.16 is more stable in this respect, but the radius depends much more on the  $T$ -region for the fit. For a larger range  $r$  increases using Function 6.16 but also  $\chi^2$  increases, because the fit does not match the data well. For this reason we excluded the results using Function 6.16 from further considerations, but quote the results here for completeness.

In general, the systematic errors of the double ratio taken with the “mixed” reference sample seem to be smaller than for the unlike-sign sample. The highest contribution to the systematic error in the “unlike” case comes from the difference between the MEPS and the MEAR Monte Carlo, as the extracted  $\lambda$  parameter is significantly higher as for the latter model.

For the reference distribution the first bin and the regions of the  $\rho^0$  resonance (0.65–0.85 GeV in  $T$ ) and  $K_s^0$  resonance (0.37–0.43 GeV in  $T$ ) are excluded from the fit which is taken over the full range in  $T$  from 0–2 GeV.

The final results are collected in Table 6.6. The entry in this table include only the results from the second analysis (Table 6.2, (A), (C), 6.3 (C), 6.4 (B))

## 6.10 Results and discussion

Tables 6.1 – 6.9 summarize all results, which were obtained in this analysis using the high and low  $Q^2$  data sets, for both the unlike-pair and event-mixed reference samples, in the latter case for the two ways, which were used to mix events, and lastly also for those cases, where final state corrections were applied. Since the low  $Q^2$  data sample is the statistically most significant one, it was used to study the systematic uncertainties mentioned in the last section and the corrections, hence Tables 6.1 – 6.8, where these studies are summarized, pertain only to this sample. Though the first and second analysis in principle only differ by a new way to mix

events, and hence should not effect the results for the unlike-pair reference sample, we have quoted them in Tables 6.1 – 6.5, 6.8 and 6.9 too, because small differences existed also in the event and track selection for both these analyses. The second analysis set a cut on the hadronic energy sum determined via the Jacquet-Blondel method [ $W_{JB}^2 > 4400 \text{ GeV}^2$ ], and required more than 10 hits in the central jet chambers. Both these cuts were absent in the first analysis and lead to a loss of 20 % of the events. The values found for the two analyses are in good agreement with each other in general. For the two cases, where differences occur, they are well within the range of systematic uncertainties. The results are grouped as follows: Tables 6.1 – 6.2 present results for the double ratios, data compared to reference sample divided by Monte Carlo compared to reference sample, for the CDM and the MEPS event generator and up to three different functions used for the parametrization. Tables 6.4 and 6.5 list the results from the intercomparison of two different data samples generated with the same event generator (CDM) with BEC included in the generation step or not. The radius used in the generation step was  $r = 0.53 \text{ fm}$  (see Appendix A), approximately matched to the experimental result. Here also a comparison between double and single ratios could be made and also a comparison directly at the generator level, i. e. before the events had passed the detector simulation and reconstruction step. Table 6.7 exhibits the influence of purity and Coulomb correction. For these the analysis was not repeated. Table 6.8 collects the data from the different data subsets, and lastly Table 6.9 can be considered the essence of our analysis, the parameters from the fit to the high and the low  $Q^2$  sample using the double ratio and the standard parametrization (Equation 2.16). For completeness we have included results obtained within our collaboration [65] for the diffractive subset of the deep inelastic scattering data set.

### 6.10.1 Low $Q^2$ data

The results (Table 6.9) for the two different reference samples are slightly different, as already observed in other experiments [41, 42, 46, 47, 49, 50]. These differences are ascribed [51, 27] to correlations imposed by the decays of other long lived resonances as e. g.  $\omega, \eta, \eta'$ , non-resonant  $\pi\pi$ -interaction and Coulomb effects. This observation is independent of the choice of the Monte Carlo generator used to describe the scattering process — the detector description of course being the same. The difference appears already at the generator level, in the double and single ratios as apparent from Table 6.4 and 6.5. The event mixing method however leads to values for the radius quite close to what has been used in the generator, which why these values in general are preferred and used for communication with other recent analysis.

Since  $R = 0.53 \text{ fm}$  was used in the generator and  $0.51 \leq r \leq 0.61 \text{ fm}$  is found in the analysis, we must assign a systematic error of  $\pm 0.05 \text{ fm}$  to our results. The detector influence is small on the other hand. At the generator level and after the reconstruction nearly identical results are obtained. The unlike-pair reference sample was included mainly to allow also to look for trends in comparison to older low energy experiments.

In our first analysis we found a 1.6 standard deviation difference between the two Monte Carlo generators for  $r$ . This observation lead us to redo the analysis with a more refined mixing technique, which removed this difference completely. Since we could not isolate any cause for

the difference in the first analysis we consider it a statistical fluctuation. Taking the average of all differences, were both Monte Carlos have been compared for the event mixing sample, we arrive at a variation of  $\Delta r = \pm 0.04$ .  $\lambda$  has been treated similar.

Including the other smaller error source mentioned above, our final result of the low  $Q^2$  data-sample is :

$$r = 0.54 \pm 0.03 \pm 0.10 \quad \lambda = 0.32 \pm 0.02 \pm 0.10 \quad (6.19)$$

where the first quoted error is statistical and the second systematic.

The corresponding result for the unlike-sign reference sample is :

$$r = 0.68 \pm 0.04 \pm 0.21 \quad \lambda = 0.52 \pm 0.03 \pm 0.29 \quad (6.20)$$

The inclusion of the final state corrections does not alter these results, as Table 6.7 shows. In Figure 6.28 we demonstrate, how the double ratio is modified, when the Gamov factors are applied in order to correct for the Coulomb repulsion and attraction, i. e. when the correction function shown in Figure 6.23 is multiplied bin by bin. An enhancement of the very first bins is obvious, while the rest remains unchanged. The effect on the fit variables is an enhancement of the radius of 3% and in lambda of 4.5% in the sample which uses the event mixing reference sample and in the ratio using the unlike sign reference sample the change is 2.5% for  $r$  and 14% for  $\lambda$ .

When the purity correction is applied to the double ratio in order to study the effect of long lived resonances and particles in the data-sample, which do not obey Bose Einstein statistics according to Section 6.7.2, one has two choices: either one can fit the data with Function 6.13 or multiply each bin of data with 6.15. Both methods are summarized in Figure 6.29. The values from the purity corrected data fitted with the Function 2.16 are :

$$\lambda = 1.09 \pm 0.04, \quad r = 0.56 \pm 0.01 \text{ fm} \quad (6.21)$$

and hence in good agreement with a value of one for the "chaoticity" parameter  $\lambda$ .

### Other functions to fit the double ratio

As already discussed in the theory part the string fragmentation model predicts an exponential shape of the correlation function which is based on the treatment of BEC in that model. In the course of our analysis we noticed that both reference samples the double ratio matches slightly better to an exponential function than to a Gaussian one. Furthermore effects like purity or Coulomb correction enhance the correlation mainly in the first bins. The measured correlation function appears reduced and hence "real" correlations should look even more like an exponential function and less Gaussian.

It is worthwhile to note that in the article of Andersson and Hofmann [35] on BEC and strings, a model is introduced in which the length scale measured by BEC is not interpreted as the diameter of the total pion emitting source, but instead as the distance in production points for which the momentum distributions still overlap. In this picture it is not surprising that nearly all measured radii in so many different experiments (except heavy ion ones) are the same (see Chapter 6.11).

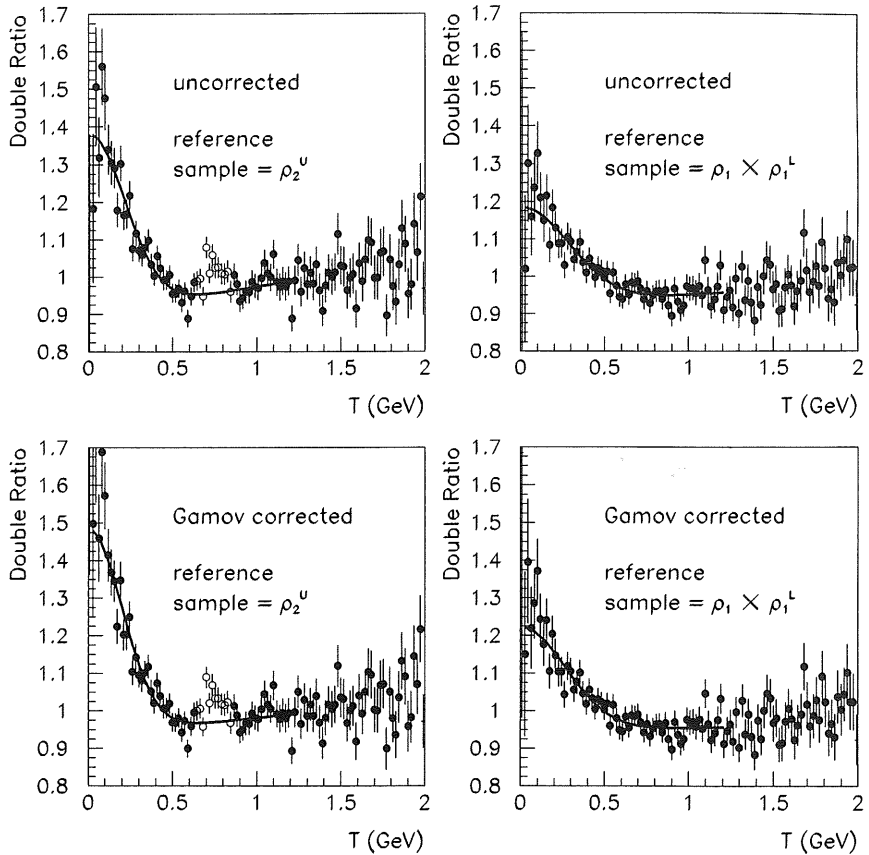


Figure 6.28: Double ratio with different reference samples for the uncorrected data (a) and (b) and for corrected data (c) and (d) with the Gamov correction function showed in Figure 6.23

### 6.10.2 High $Q^2$ and diffractive data

The selection of the high  $Q^2$  data-sample was described in section 5.1. The data is processed through the same analysis software as the low  $Q^2$  data and its double ratio



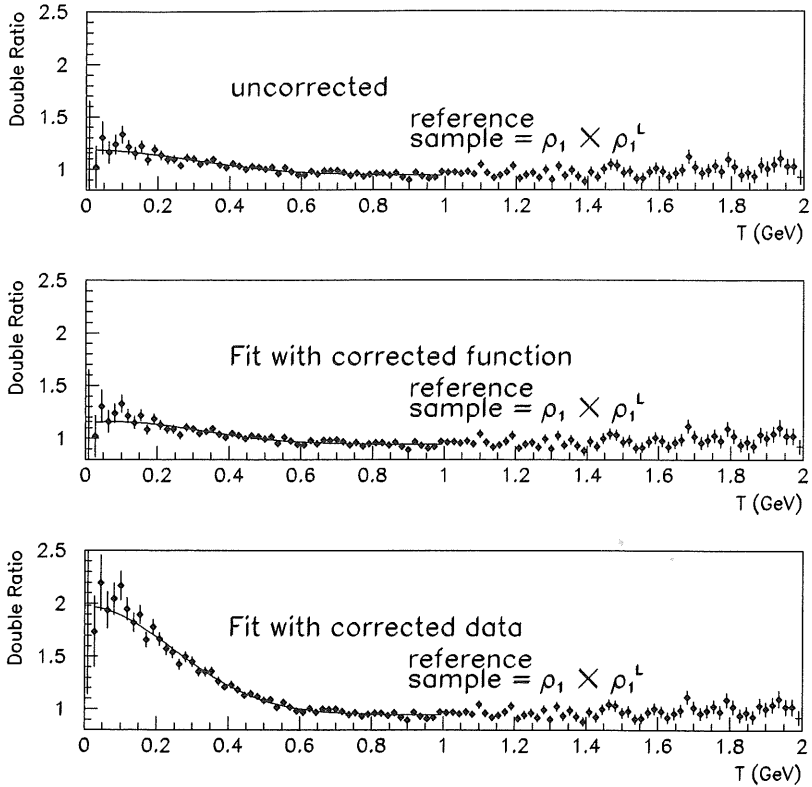


Figure 6.29: Double ratio with purity correction applied. a) unchanged data fitted with Function 2.16. b) unchanged data fitted with Function 6.13. c) purity corrected data with 6.15 fitted with Function 2.16.

$R'(T) = R^{\text{data}}(T)/R^{\text{MC}}(T)$  is fitted with the the same Function 6.4.

No differences appeared between our two data-samples . The data are shown in Figures 6.30 and 6.31. First, the Tables 6.1, 6.2 and 6.3 collect the fit-parameters from the double ratios corrected with the CDM and the MEPS Monte Carlo.

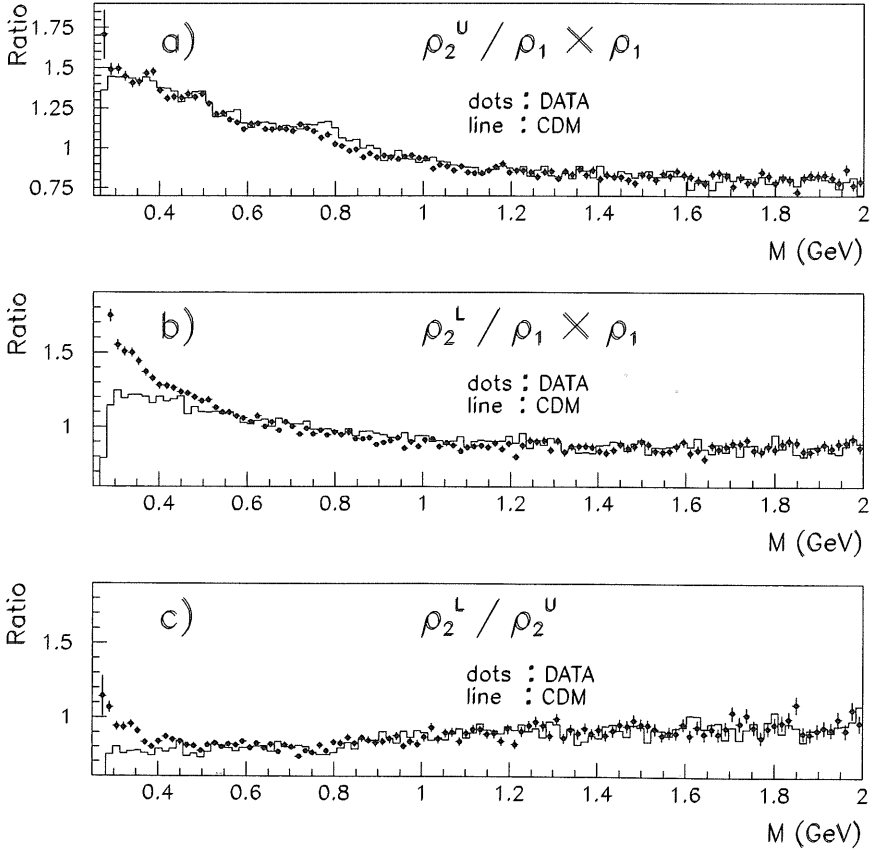


Figure 6.30: The same distributions as in Figure 6.13 for high  $Q^2$  data.

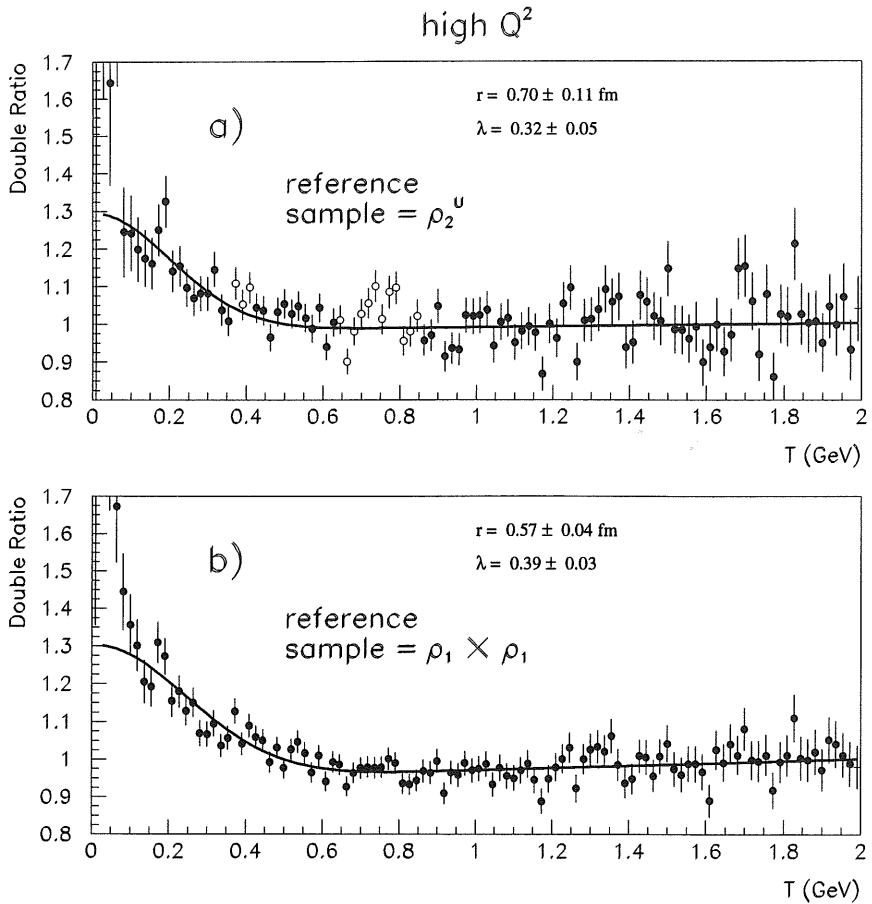


Figure 6.31: Double ratios of the high  $Q^2$  data sample. The plots are the same as in Figure 6.14.

excluded areas in the fit	Reference sample			
	unlike-sign $\rho_2^0(T)$		event-mixed $\rho_1 \otimes \rho_1(T)$	
	$r(\text{fm})$	$\lambda$	$r(\text{fm})$	$\lambda$
first analysis MEAR				
<b>A</b>	function of the fit $N(1 + \delta T)[1 + \lambda \exp(-r^2 T^2)]$			
fit-range 0 - 1.2 GeV				
all bins	0.76±0.04	0.48±0.03	0.49±0.06	0.28±0.05
all bins except first	0.76±0.04	0.48±0.03	0.49±0.06	0.28±0.05
$\rho^0$ excluded	0.66±0.05	0.52±0.05		
$K^0$ excluded	0.77±0.05	0.49±0.04		
$\rho^0$ and $K^0$ excluded	0.68±0.05	0.53±0.05		
fit-range 0 - 2 GeV				
all bins	0.75±0.04	0.49±0.04	0.47±0.04	0.30±0.03
$\rho^0$ excluded	0.67±0.04	0.52±0.03		
$K^0$ excluded	0.76±0.04	0.50±0.04		
$\rho^0$ and $K^0$ excluded	0.68±0.04	0.52±0.04		
<b>B</b>	function of the fit $N[1 + \lambda \exp(-r^2 T^2)]$			
fit-range 0 - 1.2 GeV				
all bins	0.79±0.04	0.46±0.04	0.52±0.04	0.26±0.02
$\rho^0$ and $K^0$ excluded	0.76±0.04	0.47±0.04		
fit-range 0 - 2 GeV				
all bins	0.81±0.04	0.46±0.04	0.55±0.04	0.26±0.02
$\rho^0$ and $K^0$ excluded	0.80±0.04	0.47±0.04		
<b>C</b>	function of the fit $N(1 + \delta T + \epsilon T^2)[1 + \lambda \exp(-r^2 T^2)]$			
fit-range 0 - 1.2 GeV				
all bins	0.76±0.05	0.48±0.04	0.48±0.07	0.27±0.04
$\rho^0$ and $K^0$ excluded	0.68±0.05	0.53±0.05		
fit-range 0 - 2 GeV				
all bins	0.76±0.04	0.48±0.05	0.47±0.04	0.27±0.02
$\rho^0$ and $K^0$ excluded	0.68±0.04	0.52±0.04		

Table 6.1: Summary from fit-parameters with different functions and different ranges. The CDM Monte Carlo is used as the reference sample to form the double ratio

excluded areas in the fit	Reference sample			
	unlike-sign $\rho_2^U(T)$		event-mixed $\rho_1 \otimes \rho_1(T)$	
	$r(\text{fm})$	$\lambda$	$r(\text{fm})$	$\lambda$
second analysis MEAR				
<b>A</b>	function of the fit $N(1 + \delta T)[1 + \lambda \exp(-r^2 T^2)]$			
	fit-range 0 - 1.2 GeV			
all bins	0.77±0.05	0.48±0.04	0.56±0.03	0.32±0.02
all bins except first	0.77±0.05	0.48±0.04	0.56±0.03	0.32±0.02
$\rho^0$ excluded	0.67±0.05	0.53±0.05		
$K^0$ excluded	0.78±0.05	0.49±0.04		
$\rho^0$ and $K^0$ excluded	0.67±0.05	0.53±0.05		
	fit-range 0 - 2 GeV			
all bins	0.76±0.04	0.49±0.04	0.54±0.03	0.32±0.02
$\rho^0$ excluded	0.68±0.04	0.52±0.04		
$K^0$ excluded	0.77±0.04	0.49±0.04		
$\rho^0$ and $K^0$ excluded	0.68±0.04	0.52±0.03		
<b>B</b>	function of the fit $N[1 + \lambda \exp(-r^2 T^2)]$			
	fit-range 0 - 1.2 GeV			
all bins	0.80±0.04	0.46±0.04	0.56±0.03	0.31±0.02
$\rho^0$ and $K^0$ excluded	0.76±0.04	0.47±0.04		
	fit-range 0 - 2 GeV			
all bins	0.82±0.04	0.46±0.04	0.57±0.03	0.31±0.02
$\rho^0$ and $K^0$ excluded	0.80±0.04	0.46±0.04		
<b>C</b>	function of the fit $N(1 + \delta T + \epsilon T^2)[1 + \lambda \exp(-r^2 T^2)]$			
	fit-range 0 - 1.2 GeV			
all bins	0.77±0.05	0.48±0.04	0.56±0.03	0.31±0.02
$\rho^0$ and $K^0$ excluded	0.67±0.05	0.53±0.04		
	fit-range 0 - 2 GeV			
all bins	0.77±0.05	0.48±0.05	0.54±0.03	0.32±0.03
$\rho^0$ and $K^0$ excluded	0.68±0.04	0.52±0.04		

Table 6.2: The same table as Table 6.1 but for the second analysis

excluded areas in the fit	Reference sample			
	unlike-sign $\rho_2^U(T)$		event-mixed $\rho_1 \otimes \rho_1(T)$	
	$r$ (fm)	$\lambda$	$r$ (fm)	$\lambda$
first analysis MEPS				
<b>A</b>	function of the fit		$N(1 + \delta T)[1 + \lambda \exp(-r^2 T^2)]$	
	fit-range 0 - 1.2 GeV			
all bins	0.71±0.05	0.31±0.03	0.65±0.06	0.30±0.04
$\rho^0$ excluded	0.63±0.07	0.33±0.05		
$\rho^0$ and $K^0$ excluded	0.66±0.07	0.33±0.04		
	fit-range 0 - 2 GeV			
all bins	0.71±0.05	0.31±0.03	0.60±0.06	0.31±0.03
$\rho^0$ excluded	0.65±0.05	0.32±0.03		
$\rho^0$ and $K^0$ excluded	0.67±0.06	0.33±0.03		
<b>B</b>	function of the fit		$N[1 + \lambda \exp(-r^2 T^2)]$	
	fit-range 0 - 1.2 GeV			
all bins	0.71±0.05	0.31±0.03	0.66±0.06	0.30±0.03
$\rho^0$ excluded	0.65±0.04	0.32±0.03		
$\rho^0$ and $K^0$ excluded	0.68±0.05	0.33±0.03		
	fit-range 0 - 2 GeV			
all bins	0.71±0.05	0.31±0.03	0.69±0.06	0.30±0.04
$\rho^0$ excluded	0.67±0.04	0.32±0.03		
$\rho^0$ and $K^0$ excluded	0.69±0.05	0.32±0.03		
second analysis MEPS				
<b>C</b>	function of the fit		$N(1 + \delta T)[1 + \lambda \exp(-r^2 T^2)]$	
	fit-range 0 - 1.2 GeV			
all bins	0.71±0.05	0.31±0.03	0.55±0.05	0.37±0.05
$\rho^0$ excluded	0.62±0.07	0.34±0.05		
$\rho^0$ and $K^0$ excluded	0.64±0.08	0.34±0.05		
	fit-range 0 - 2 GeV			
all bins	0.70±0.05	0.31±0.03	0.54±0.03	0.38±0.02
$\rho^0$ excluded	0.65±0.05	0.32±0.03		
$\rho^0$ and $K^0$ excluded	0.66±0.06	0.33±0.03		
<b>D</b>	function of the fit		$N[1 + \lambda \exp(-r^2 T^2)]$	
	fit-range 0 - 1.2 GeV			
all bins	0.71±0.05	0.31±0.03	0.61±0.03	0.33±0.02
$\rho^0$ and $K^0$ excluded	0.67±0.05	0.32±0.03		
	fit-range 0 - 2 GeV			
all bins	0.71±0.05	0.31±0.03	0.65±0.03	0.33±0.02
$\rho^0$ and $K^0$ excluded	0.69±0.05	0.32±0.03		

Table 6.3: Summary from fit-parameters with different functions and different ranges for the first and the second analysis. The MEPS Monte Carlo is used as the reference sample to form the double ratio.

	unlike-sign $\rho_2^U(T)$		event-mixed $\rho_1 \otimes \rho_1(T)$	
	$r(\text{fm})$	$\lambda$	$r(\text{fm})$	$\lambda$
<b>A</b> first analysis				
DATA and MSR	$0.68 \pm 0.04$	$0.52 \pm 0.04$	$0.47 \pm 0.04$	$0.30 \pm 0.03$
MSR(BE) and MSR	$0.68 \pm 0.04$	$0.47 \pm 0.04$	$0.53 \pm 0.05$	$0.25 \pm 0.04$
GEN(BE) and GEN	$0.74 \pm 0.04$	$0.58 \pm 0.04$	$0.51 \pm 0.04$	$0.29 \pm 0.03$
<b>B</b> second analysis				
DATA and MSR	$0.68 \pm 0.04$	$0.52 \pm 0.03$	$0.54 \pm 0.03$	$0.33 \pm 0.02$
MSR(BE) and MSR	$0.67 \pm 0.04$	$0.48 \pm 0.04$	$0.62 \pm 0.04$	$0.27 \pm 0.02$
GEN(BE) and GEN	$0.71 \pm 0.04$	$0.57 \pm 0.04$	$0.61 \pm 0.03$	$0.35 \pm 0.02$

Table 6.4: Double ratios with CDM Monte Carlo with BEC included

	unlike-sign $\rho_2^U(T)$	
	$r(\text{fm})$	$\lambda$
first analysis		
DATA	$0.81 \pm 0.03$	$0.54 \pm 0.02$
MSR(BE)	$0.74 \pm 0.03$	$0.47 \pm 0.03$
GEN(BE)	$0.68 \pm 0.02$	$0.55 \pm 0.03$
second analysis		
DATA	$0.78 \pm 0.03$	$0.50 \pm 0.02$
MSR(BE)	$0.73 \pm 0.03$	$0.44 \pm 0.03$
GEN(BE)	$0.68 \pm 0.02$	$0.56 \pm 0.03$

Table 6.5: Single ratios  $R(T) = R(T) = \rho_2(T)/\rho_2^U(T)$  from data and CDM Monte Carlo with BEC included.

overall systematic errors for both reference samples			
unlike-sign $\rho_2^U(T)$		event-mixed $\rho_1 \otimes \rho_1(T)$	
$r(\text{fm})$	$\lambda$	$r(\text{fm})$	$\lambda$
$\pm 0.21$	$\pm 0.29$	$\pm 0.10$	$\pm 0.10$

Table 6.6: Summary of systematic errors

CORRECTIONS and FITS	unlike-sign $\rho_2^U(T)$		event-mixed $\rho_1 \otimes \rho_1(T)$	
	$r(\text{fm})$	$\lambda$	$r(\text{fm})$	$\lambda$
first analysis				
Gamov corr.	$0.71 \pm 0.05$	$0.58 \pm 0.04$	$0.49 \pm 0.05$	$0.33 \pm 0.07$
Purity corr.	$0.80 \pm 0.05$	$2.30 \pm 0.22$	$0.56 \pm 0.01$	$1.09 \pm 0.04$
Purity and Gamov corr.	$0.77 \pm 0.05$	$2.71 \pm 0.20$	$0.58 \pm 0.04$	$1.30 \pm 0.11$

Table 6.7: Double ratios with final state interactions applied

kinemat. variable	limit	LOW ,mixed reference $\rho_1 \otimes \rho_1(T)$		HIGH ,mixed reference $\rho_1 \otimes \rho_1(T)$	
		$r(\text{fm})$	$\lambda$	$r(\text{fm})$	$\lambda$
first analysis					
$x_{\text{Bj\o{r}ken}}$	$10^{-3}$	$0.53 \pm 0.05$	$0.37 \pm 0.04$	$0.50 \pm 0.05$	$0.40 \pm 0.05$
multiplicity	10	$0.45 \pm 0.03$	$0.44 \pm 0.04$	$0.83 \pm 0.11$	$0.45 \pm 0.08$
W	140 GeV	$0.49 \pm 0.04$	$0.43 \pm 0.05$	$0.52 \pm 0.05$	$0.36 \pm 0.04$
$Q^2$	20 GeV	$0.51 \pm 0.04$	$0.93 \pm 0.04$	$0.51 \pm 0.06$	$0.38 \pm 0.05$
$p_1 + p_2$	1.5 GeV	$0.52 \pm 0.04$	$0.38 \pm 0.04$	$0.51 \pm 0.06$	$0.35 \pm 0.05$
second analysis					
$x_{\text{Bj\o{r}ken}}$	$10^{-3}$	$0.57 \pm 0.05$	$0.33 \pm 0.03$	$0.26 \pm 0.02$	$0.30 \pm 0.01$
multiplicity	10	$0.50 \pm 0.04$	$0.32 \pm 0.03$	$0.71 \pm 0.08$	$0.35 \pm 0.05$
W	140 GeV	$0.59 \pm 0.07$	$0.27 \pm 0.04$	$0.53 \pm 0.04$	$0.34 \pm 0.03$
$Q^2$	20 GeV	$0.57 \pm 0.05$	$0.29 \pm 0.03$	$0.49 \pm 0.04$	$0.40 \pm 0.04$
$p_1 + p_2$	1.5 GeV	$0.51 \pm 0.03$	$0.29 \pm 0.02$	$0.59 \pm 0.05$	$0.40 \pm 0.04$

Table 6.8: Double ratios with different kinematical event-classes

DATA-SAMPLE	unlike-sign $\rho_2^U(T)$		event-mixed $\rho_1 \otimes \rho_1(T)$	
	$r(\text{fm})$	$\lambda$	$r(\text{fm})$	$\lambda$
first analysis				
Low $Q^2$ MEAR	$0.68 \pm 0.05$	$0.52 \pm 0.05$	$0.49 \pm 0.06$	$0.28 \pm 0.05$
Low $Q^2$ MEPS	$0.63 \pm 0.07$	$0.33 \pm 0.05$	$0.65 \pm 0.06$	$0.30 \pm 0.04$
second analysis				
Low $Q^2$ MEAR	$0.68 \pm 0.04$	$0.52 \pm 0.04$	$0.54 \pm 0.03$	$0.32 \pm 0.02$
Low $Q^2$ MEPS	$0.63 \pm 0.06$	$0.33 \pm 0.03$	$0.54 \pm 0.03$	$0.38 \pm 0.02$
High $Q^2$	$0.70 \pm 0.11$	$0.32 \pm 0.05$	$0.57 \pm 0.04$	$0.39 \pm 0.03$
diffractive (ARIADNE) (see [65])	$0.62 \pm 0.12$	$0.46 \pm 0.11$	$0.51 \pm 0.06$	$0.40 \pm 0.14$
diffractive (Parton shower) (see [65])	$0.57 \pm 0.14$	$0.52 \pm 0.13$	$0.46 \pm 0.05$	$0.49 \pm 0.06$

Table 6.9: Summary of the tree data-samples.



### 6.10.3 $x_{\text{Björken}}$ , $W$ and multiplicity dependence

Subdividing the sample indicated, that the results obtained are rather independent of the kinematical region. Only for the high- $x_{\text{Björken}}$  subset (smaller radius) and the high-multiplicity subset (larger radius) differences outside the statistical and systematical errors are observed. If substantiated by higher statistics data sets in subsequent analyses, where really in function of  $x_{\text{Björken}}$  and multiplicity trends could be observed, such deviations would be clearly the most exciting result of our analysis.

## 6.11 Comparison with other Experiments

Table 6.10 is a summary of the results from the fit to the double ratio from other experiments. The errors are only the statistical ones. Different experiments used different data-samples i. e. sometimes purity correction and/or corrections to final state interactions as Coulomb corrections (Gamov factors) were applied. This is the main source for the big systematic differences of both values and of the difficulty to compare results from other events. The values of  $r$  extracted with a mixed reference sample are systematically lower than those obtained with an unlike-sign background which is also visible in our data. The fluctuations in the parameter  $\lambda$  are much higher and more sensible on different analysis techniques used in this field. Our results are broadly consistent with results from  $\ell N$ -scattering at lower energies and from  $e^+e^-$ -annihilation.

EXPERIMENT		unlike-sign $\rho_2^{\pm}(T)$		event-mixed $\rho_1 \otimes \rho_1(T)$		$\sqrt{s}$
		$r(\text{fm})$	$\lambda$	$r(\text{fm})$	$\lambda$	[GeV]
$\ell N$	EMC ( $\mu p$ )	$0.84 \pm 0.03$	$1.08 \pm 0.10$	$0.46 \pm 0.03$	$0.73 \pm 0.06$	23
	E665 ( $\mu p$ )			$0.39 \pm 0.02$	$0.35 \pm 0.02$	30
	BBCNC ( $\nu N$ )	$0.80 \pm 0.04$	$0.61 \pm 0.04$	$0.64 \pm 0.04$	$0.46 \pm 0.03$	10-28
	HERA	$0.68 \pm 0.04$	$0.52 \pm 0.03$	$0.54 \pm 0.03$	$0.32 \pm 0.02$	300
$e^+e^-$	DELPHI	$0.83 \pm 0.03$	$0.31 \pm 0.02$	$0.47 \pm 0.03$	$0.24 \pm 0.02$	91
	ALEPH	$0.80 \pm 0.04$	$0.62 \pm 0.04$	$0.50 \pm 0.02$	$0.40 \pm 0.02$	91
	OPAL	$0.93 \pm 0.02$	$0.86 \pm 0.03$			91
	MARK 2	$0.84 \pm 0.06$	$0.50 \pm 0.07$			29 (3)
	TASSO	$0.80 \pm 0.06$	$0.35 \pm 0.07$			34
	AMY	$0.73 \pm 0.05$	$0.47 \pm 0.05$	$0.58 \pm 0.06$	$0.39 \pm 0.02$	58
	VEPP	$0.73 \pm 0.11$	$0.71 \pm 0.16$			9.5 (7-10)
	CLEO	$0.54 \pm 0.10$	$0.99 \pm 0.14$			9.5 (7-10)

Table 6.10: Results from other experiments

## Appendix A

The parameters of the generator (JETSET 7.4) which were changed from their default values (see [8]) are :

$$MSTJ(51) = 2 \tag{6.22}$$

which includes a Gaussian parametrization according to :  $C_2(T) = 1 + PARJ(92) \cdot e^{-\left(\frac{T}{PARJ(93)}\right)^2}$

$$MSTJ(52) = 7 \tag{6.23}$$

which specifies the number of particle species for which Bose-Einstein correlations are to be included.  $MSTJ(52) = 7$  incorporates the inclusion of:  $\pi^0, \pi^+, \pi^-, K^+, K^-, K_s^0$  and  $K_l^0$ .

$$PARJ(92) = 1. \tag{6.24}$$

steers the nominal strength of Bose-Einstein effects for  $T$ . This parameter corresponds to the "chaoticity parameter"  $\lambda$ .

$$PARJ(93) = 0.38 \tag{6.25}$$

is the size of the Bose-Einstein effect region in terms of the  $T$  variable, see  $MSTJ(51)$ . The more conventional measure, in terms of the "radius"  $r$  of the production volume, is given by:  $r = h \cdot c / PARJ(93) = 0.2 fm GeV / PARJ(93)$ . Our value of  $PARJ(93) = 0.38$  corresponds to a radius  $r = \frac{0.2}{0.38} = 0.53$  fm

# List of Figures

2.1	Two different paths of a two-pion system . . . . .	4
2.2	Schematic illustration of a two pion correlation experiment . . . . .	7
2.3	Space-time development of hadronization in the string model . . . . .	11
2.4	Two string configurations which lead to the same final state . . . . .	13
3.1	Feynman diagram for basic DIS process . . . . .	15
3.2	Feynman diagram of a diffractive DIS event . . . . .	18
4.1	The storage ring HERA with its preaccelerators. . . . .	20
4.2	The H1 detector with its main components. . . . .	22
4.3	Side view of the H1 tracking system. . . . .	24
4.4	Radial view of the H1 tracking system. . . . .	25
5.1	The inner $z$ -drift chamber . . . . .	27
5.2	Schematic view of drift-cells in the middle of CIZ. . . . .	29
5.3	One single driftcell of CIZ. . . . .	30
5.4	Mean charge of CIZ with different gas mixtures. . . . .	31
5.5	Mean charge of CIZ with the gas mixture Argon/Ethane. . . . .	32
5.6	Deviation of CIZ hits from a CJC track as a function of $\vartheta$ . . . . .	35
5.7	<i>Deviations</i> of CIZ from the track fit which uses only the COZ . . . . .	41
5.8	Fit-parameters $A$ and $B$ of the line-fit in the drift-cells. . . . .	42
5.9	Projection of the <i>deviation</i> of CIZ hits. . . . .	43
5.10	CIZ <i>deviation</i> with CIZ shifted by 3.8 mm. . . . .	44
5.11	<i>Deviations</i> of COZ from the track fit which uses only the CIZ. . . . .	45
5.12	<i>Deviations</i> of CIZ hits from $ep$ data. . . . .	46
5.13	<i>Deviation</i> of CIZ hits for the inner and outer wire types. . . . .	47
5.14	<i>Deviation</i> and <i>resolution</i> of CIZ. . . . .	48
5.15	Internal resolutions of CIZ. . . . .	49
5.16	Difference between a simulated track and the same reconstructed track. . . . .	50
5.17	Relative momentum resolution. . . . .	51
5.18	Three different efficiencies as a function of the high voltage. . . . .	52
5.19	Single wire efficiency of CIZ. . . . .	53
6.1	A typical low $Q^2$ event . . . . .	56

6.2	A typical high $Q^{*2}$ event . . . . .	56
6.3	Ratio of positive and negative tracks . . . . .	57
6.4	Invariant mass distribution of pairs of charged tracks . . . . .	58
6.5	Radial view of a typical low $Q^2$ event used for BEC . . . . .	59
6.6	Track pair used for BEC . . . . .	60
6.7	Final track selection . . . . .	61
6.8	Invariant mass spectrum of mixed pairs from different events. . . . .	62
6.9	Invariant mass of mixed pairs from different events. . . . .	63
6.10	Uncorrelated background for data and Monte Carlo. . . . .	65
6.11	Invariant mass distribution of the low $Q^2$ data-sample. . . . .	66
6.12	Invariant mass distribution of the low $Q^2$ Monte Carlo sample (CDM). . . . .	67
6.13	Ratio $R(M)$ for data and CDM Monte Carlo. . . . .	68
6.14	Double ratio of the low $Q^2$ data . . . . .	70
6.15	Correction factors . . . . .	71
6.16	Ratio $R(M)$ for corrected data and GEN (CDM). . . . .	73
6.17	Ratio $R(M)$ for data and MSR divided in $x_{\pi\pi}$ . . . . .	74
6.18	Ratio $R(M)$ for data and MSR (MEPS). . . . .	75
6.19	Comparison of the Monte Carlo with and without simulated BEC . . . . .	78
6.20	Ratio $R(M)$ for corrected data and GEN with included BEC. . . . .	79
6.21	Ratio $R(M)$ for data and MSR with included BEC. . . . .	80
6.22	Double ratios $R'(M)$ for data and Monte Carlo with included BEC. . . . .	81
6.23	Gamov correction factors . . . . .	83
6.24	The invariant mass distributions of some resonance channels. . . . .	84
6.25	Inv. mass distributions of the $\eta'$ resonance. . . . .	85
6.26	Different fractions of special like-sign pions to all like-sign pions. . . . .	87
6.27	Double ratios of four data samples with different event kinematic. . . . .	88
6.28	Double ratio corrected with Gamov factors . . . . .	93
6.29	Double ratio with purity correction applied. . . . .	94
6.30	Ratio $R(T)$ for the high $Q^2$ data-sample. . . . .	95
6.31	Double ratio for the high $Q^2$ data-sample. . . . .	96

# List of Tables

4.1	Summary of HERA parameters. . . . .	21
4.2	Central jet chamber parameters. . . . .	26
5.1	CIZ parameters . . . . .	28
5.2	CIZ resolutions . . . . .	49
6.1	Summary of different fits with CDM Monte Carlo as reference sample(first analysis)	97
6.2	Summary of different fits with CDM Monte Carlo as reference sample (second analysis). . . . .	98
6.3	Summary of different fits with MEPS Monte Carlo as reference sample. . . . .	99
6.4	Double ratios with CDM Monte Carlo with BEC included . . . . .	100
6.5	Single Ratios with CDM Monte Carlo with BEC included. . . . .	100
6.6	Summary of systematic errors . . . . .	100
6.7	Gamov corrections . . . . .	101
6.8	Double ratios with different kinematical event-classes . . . . .	101
6.9	Summary of the three data-samples. . . . .	101
6.10	Results from other experiments . . . . .	102

# Bibliography

- [1] H1 Collaboration, DESY internal report, DESY 93-103 (1993)
- [2] T. Lohse, DESY Internal Report, DESY-PRC 94-02 (1994).
- [3] DESY Internal Report, DESY-PRC 93-06 (1993).
- [4] Status Report 1993, DESY, Hamburg (Feb. 1993).
- [5] J. Bürger Nucl. Instr. Meth. A279 (1989) 217.
- [6] K. Müller Nucl. Instr. Meth. A312 (1992) 457.
- [7] K. Müller, Ph.D. Thesis, University of Zürich, unpublished, 1994.
- [8] T. Sjöstrand, CERN-TH.7112/93
- [9] A.S. Davydov, *Quantum Mechanics* Pergamon Press, London (1965)
- [10] M. G. Bowler, Z. Phys. C29 (1985), 617
- [11] M. G. Bowler, Particle World, Vol.2, No.1, 1
- [12] M.G. Bowler, Phys. Lett. B270 (1991), 69.
- [13] R. D. Field, R. P. Feynman, Nucl. Phys. B136 (1978), 1
- [14] For recent reviews, see e.g. Proc. of the Ringberg Workshop "*Fluctuations and Fractal Structure*", Eds. R. Hwa, W. Ochs, N. Schmitz, World Scientific, Singapore, 1992; E.A. De Wolf, I.M. Dremin, W.K. Kittel, "*Scaling laws for density correlations and fluctuations in Multiparticle Dynamics*", Nijmegen preprint HEN-362 (1993), Brussels preprint IIHE-ULB-VUB-93-01
- [15] A. Białas, R. Peschanski: Nucl. Phys. B273 (1986) 703; B308 (1988) 857
- [16] Contr. EPS-0481 to Int. Europhysics Conf. on High-Energy Physics, Brussels (1995); Contr. paper to Lepton-Photon Conf., Beijing, China (1995).
- [17] R. Hanbury Brown, R.Q. Twiss, Phil. Mag. 45, 663 (1954);
- [18] R. Hanbury Brown, R.Q. Twiss, Nature 177, 27 (1956)

- [19] R. Hanbury Brown, R.Q. Twiss, *Nature* 178, 1046 (1956)
- [20] R. Hanbury Brown, R.Q. Twiss, *Proc. Royal Soc.* Vol. 243, 291 (1958);
- [21] G.Goldhaber, W.B. Fowler, S. Goldhaber, T.F. Hoang, T.F. Kalegoropoulos and W.F. Powell, *Phys. Rev. Lett.* 3, 181 (1959)
- [22] G.Goldhaber, S. Goldhaber, W. Lee and A. Pais, *Phys. Rev.* 120, 300 (1960)
- [23] A.H.Mueller, *Phys. Rev. D*4 (1971) 150
- [24] E.A. De Wolf, L.M. Dremin, W. Kittel, *Phys. Rep.* C.
- [25] J.B. Bjorken, *Proc. XXIV. Symposium on Multiparticle Dynamics, Vietri sul Mare, Italy (1994)*, eds. A. Giovannini et al. (World Scientific, Singapore 1995), p.611.
- [26] W. A. Zajc, in *Hadronic Multiparticle Production*, Advanced Series on Directions in High-Energy Physics, P. Caruthers ed. (World Scientific, Singapore, 1988), vol. 2, p. 235; *Proc. Int. Workshop on Correlations and Multiparticle Production (LESIP 4)*, Marburg, Germany (1990), M. Plümer et al. eds. (World Scientific, Singapore, 1991), p. 439.
- [27] B. Lörstad, *Int. J. mod. Phys. A*, Vol. 4 Nr. 12 (1989), 2861.
- [28] G. Goldhaber, *Proc. Workshop on Local Equilibrium in Strong Interaction Physics (LESIP 1)*, Bad Honnef, Germany (1984), eds. D. K. Scott and R. M. Weiner (World Scientific 1985), p. 115.
- [29] D. Boal et al., *Rev. Mod. Phys.* 62 (1990), 553.
- [30] S. Haywood, Rutherford Appleton Laboratory RAL REP. 94-074 1994.
- [31] E.A. De Wolf, *Proc. XXVIIth International Conf. on High Energy Physics, Glasgow, (1994)*, 1281.
- [32] M. Suzuki. *Phys. Rev. D*35 (1987), 3359
- [33] B. Andersson, G. Gustafson, G. Ingelman and T. Sjöstrand, *Phys. Rep.* 97 (1983) 33
- [34] X. Artru and G. Menessier, *Nucl. phys.* B70 (1974) 93
- [35] B. Andersson and W. Hofmann, *Phys. Lett.* B169 (1986), 364.
- [36] X. Artru and M. G. Bowler, *Z. Phys.* C37 (1988), 293.
- [37] G. Ingelman, *Proc. Workshop on Physics at HERA, Hamburg (1991)*, eds. W. Buchmüller and G. Ingelman (DESY, Hamburg 1992), vol. 3, p. 1366.
- [38] L. Lönnblad, *Comput. Phys. Commun.* 71 (1992), 15.
- [39] T. Eckel, Diploma Thesis, University of Hamburg, DESY report H1-08/94-371 (1994), unpublished.

- [40] G. Gustafson and U. Petterson, Nucl. Phys. B306 (1988), 746; G. Gustafson, Phys. Lett. B175 (1986), 453; A. Andersson et al., Z. Phys. C43 (1989), 625.
- [41] DELPHI Collaboration, Phys. Lett. B286 (1992), 201.
- [42] DELPHI Collaboration, Z. Phys. C63 (1994) 17
- [43] DELPHI Collaboration, DELPHI 93-119 PHYS-337.
- [44] NA22 Collaboration, Z. Phys. C46 (1990), 387.
- [45] NA22 Collaboration, Z. Phys. C61 (1994), 567.
- [46] ALEPH Collaboration, Z. Phys. C54 (1992), 75.
- [47] EMC Collaboration, Z. Phys. C32 (1986), 1.
- [48] E665 Collaboration, Phys. Lett. B308 (1993), 418.
- [49] OPAL Collaboration, Phys. Lett. B267 (1991), 143.
- [50] Big Bubble Chamber Neutrino Collaboration, Z. Phys. C60 (1993), 37.
- [51] M. G. Bowler, Z. Phys C39 (1988), 81.
- [52] M. G. Bowler, Z. Phys C46 (1990), 305.
- [53] Mark II Collaboration, Phys. Rev. D39 (1989), 39.
- [54] Tasso Collaboration, Z. Phys. C30 (1986), 355.
- [55] P. Robmann, Ph. D. thesis, University of Zürich (1993).
- [56] K.Esslinger, and P. Robmann, Nucl. Instr. and Meth. A334 (1993) 649.
- [57] R. Brun *et al.*, GEANT3, CERN DD/EE/84-1 (1987)
- [58] D.Urner, Diploma Thesis, University of Zurich (1989), unpublished.
- [59] C.A. Meyer, The central inner z-chamber online and offline reconstruction software, 19 March 1993.
- [60] B.Fominykh and F.Linsel, H1 software note no. 42, Sept. 1993.
- [61] T.Walter, Diploma Thesis, University of Zurich (1995), unpublished.
- [62] A. Blondel and F. Jacquet, Proc. of "Study of an ep Facility for Europe", Ed. U. Amaldi, DESY-79-48 (1979) 391.
- [63] T. Ahmed et al. (H1 Collaboration), Nucl. Phys. **B429** (1994) 477.
- [64] T. Ahmed et al. (H1 Collaboration), Phys. Lett. **B348** (1995) 681.
- [65] E. Rizvi, Queen Mary and Westfield College, London, priv. comm.



## Acknowledgments

In the first place, I want to thank Prof. Dr. P. Truöl for the trust he had put in me and the chance he gave me to work in the H1 collaboration and to be introduced in the field of particle physics, though coming from mathematics. His intuition and experience was essential for the successful outcome of this work.

Additionally, I am very grateful to all my colleagues of the Physik-Institut in Zurich, especially Dr. Peter Robmann for very useful discussions and ideas and for the excellent technical support .

In relation with the experiment in Hamburg I want to thank all members of the H1 collaboration who helped me with technical and moral support, especially the members of the DIS physics working group (Flow and Spectra) for many interesting discussions.

This work was supported by the Swiss National Foundation.

## Curriculum Vitae

### Personalien

Name: Dollfus  
Vornamen: Christian Emanuel  
Geboren: am 9. 3. 1963 in Zürich  
Heimatort: Basel und Zürich

### Bildungsgang

1970-1979 Rudolf Steiner Schule Zürich  
1979-1980 Schule am Römerhof  
1980-1984 Kant. Unterseminar Küsnacht (ZH), kant. Matura  
1984-1991 Studium der Mathematik (Exp. Physik und Theor. Physik)  
an der Universität Zürich, Diplom in Mathematik  
1989-1990 Diplomarbeit in nichtlinearer Analysis unter der Leitung von Prof. Dr. P. Hess  
Titel: "Ein periodisches Volterra-Lotka Wettbewerbsmodell"  
1991-1996 Wissenschaftliche Mitarbeit beim H1 Experiment am  
Elektron-Proton Speicherring HERA in Hamburg (DESY)  
und Dissertation bei Prof. Dr. P. Truöl

### Dozentenverzeichnis

H. Amann	C. Amsler	F. Arndt
U. Asper	A. Barbour	D. Baumann
H. Bitto	E. Bolthausen	B. Derighetti
R. Engfer	P. Gabriel	H. Gross
P.Hess	W. Jaus	G. Karrer
E. Lichtenhahn	H.H. Keller	W. Kündig
R. Marty	G. Mazzola	P.F. Meier
H.H. Müller	B.D. Patterson	G. Rasche
A. Salzer	B. Schmid	H.R. Schwarz
H.H. Storrer	N. Straumann	K. Strebel
A. Thellung	P. Truöl	D. Wyler